NTNU – Trondheim
Norwegian University of
Science and Technology

Optimisation of Positron-Positronium Conversion and Positronium Laser Excitation

Ine Larsen Jernelv

Nanotechnology
Submission date: July 2015
Supervisor: Bo-Sture Skagerstam, IFY
Co-supervisor: Michael Doser, European Organisation for Nuclear Research (CERN)

Norwegian University of Science and Technology
Department of Physics

Cover Image:

The cover art is an image showing parts of the positron system and the experimental zone of the AEGIS experiment at CERN. The positron source is in the far right of the image, located in the blue support framework. The positron trap and accumulator regions are situated downstream of the source, with the accumulator in the far left of the image. The vacuum pumps used in each region are visible on top of the framework.

Abstract

The AEGIS collaboration (Antimatter Experiment: Gravity, Interferometry, Spectroscopy) at CERN has as its goal to directly measure the Earth's gravitational force on antimatter for the first time. Neutral antihydrogen atoms are an integral part of performing this measurement, and will be produced by the highly efficient charge-exchange reaction between a cloud of cold antiprotons and Rydberg-state positronium. This thesis work is done at CERN as a part of the AEGIS experiment, specifically in the positron system which is an essential part of the overall experiment. The focus of the work is on improvements of the positron system, testing different positron-positronium converter materials and the initial laser excitation of positronium. The improvements of the positron system were done in two parts: by the implementation of an acceleration system in order to compress the positron beam, and by investigating photon detectors for the detection of positron annihilation radiation. The result of accelerating the positron beam was a 3-fold temporal compression of the beam, and additionally a detector with good characteristics was found for the positron spectroscopy. Four different converter targets, each consisting of monocrystalline silicon with etched nanochannels, were then investigated for the production of positronium. The targets were one sample of p-type Si with crystal orientation (100), one sample of p-type Si with crystal orientation (111), and two n-type Si samples with crystal orientation (100) made with two different production processes. These were examined using lifetime spectroscopy, and only the two p-type samples displayed evidence for positronium emission. The p-type (111) was found to be slightly more efficient than the p-type (100) and had a positronium lifetime of 142.8±1 ns, while the p-type (100) gave a positronium lifetime of 111.0±1 ns. Finally, laser excitation of positronium to the $n = 3$ state with a UV laser pulse was demonstrated here for the first time, using lifetime spectroscopy.

Sammendrag

AEGIS-eksperimentet (Antimatter Experiment: Gravity, Interferometry, Spectroscopy) ved CERN har som sin oppgave å måle Jordas gravitasjonskraft på antimaterie for første gang. Nøytrale antihydrogen-atomer er en vesentlig del av utførelsen av dette eksperimentet, og vil bli produsert ved en effektiv ladningsutvekslingsreaksjon mellom en sky av kalde antiprotoner og positronium eksitert til Rydberg-nivå. Arbeidet til denne masteroppgaven er gjort ved CERN som en del av AEGIS-eksperimentet, spesifikt i positronsystemet som er en essensiell del av det eksperimentelle apparatet. Fokuset ved dette arbeidet er på forbedringer ved positronsystemet, undersøkelser av forskjellige materialer som positron-positronium-omformere, og den første laser-eksiteringen av positronium. Forbedringene av positronsystemet ble utført i to deler: ved implementering av et akselerasjonssystem for å komprimere positronstrålen og ved testing av fotondetektorer for å måle stråling i fra positroner som tillintetgjøres. Resultatene av disse forbedringene var at akselerasjonen av positronstrålen førte til at tidsspredningen minket med en faktor på 3, og i tillegg ble det funnet en detektor med gode karakteristikker for positronspektroskopi. Fire forskjellige prøver ble så testet som omformere for å produsere positronium, hvor prøvene besto av monokrystallint silisium med etsede nanokanaler. Herunder var det én prøve med p-type Si med (100)-krystallorientering, én prøve med p-type Si med (111)-krystallorientering, og to prøver med n-type Si med (100)-krystallorientering som ble blitt utsatt for forskjellige produksjonsmetoder. Disse prøvene ble undersøkt med levetids-spektroskopi, og kun prøvene som var p-type Si demonstrerte produksjon av positronium. Prøven som var p-type (111) var litt mer effektiv enn p-type (100) og ga en positronium-levetid på 142.8±1 ns, mens positronium i p-type (100) hadde en levetid på 111.0±1 ns. Til slutt ble laser-eksitering av positronium til $n = 3$ med en UV-laser demonstrert her for første gang, ved bruk av levetids-spektroskopi.

Preface

This thesis is written for the Siv.Ing degree in Nanotechnology at the Norwegian University of Science and Technology (NTNU), and is documentation for the author's work performed for the course TFY4905 - Nanotechnology, Master Thesis in the spring of 2015. The thesis has been made under the Department of Physics (IFY) at NTNU. The experimental work was done as a part of the AEGIS experiment at the European Organisation of Nuclear Research (CERN). This work was performed in the positron group at AEGIS, under Dr. Sebastiano Mariazzi.

Some of the work presented in this thesis is also included in drafts for two separate scientific publications. The preliminary titles for these articles are "Positron bunching and electrostatic transport system for the production of dense positronium clouds into vacuum" and "Efficient laser excitation to the $n = 3$ levels of positronium".

I would like to thank my supervisor Prof. Bo-Sture Skagerstam for his support of this work and helpful feedback during the writing process. I would also like to thank my co-supervisor Dr. Michael Doser for giving me the opportunity to work at AEGIS. Lastly, my thanks go to Dr. Sebastiano Mariazzi for giving me challenging and interesting work, and for providing guidance during the writing process.

Contents

List of Abbreviations

AD	Antiproton Decelerator
AEGIS	Antimatter Experiment: Gravity, Interferometry, Spectroscopy
$\bar{H}$	Antihydrogen
FWHM	Full width at half maximum
HF	Hydrofluoric acid
LINAC	Linear accelerator
MCP	Micro-channel plate
OPA	Optical parametric amplifier
OPG	Optical parametric generator
o-Ps	Orthopositronium
$\bar{p}$	Antiproton
PALS	Positron annihilation lifetime spectroscopy
PM	Penning-Malmberg
PMT	Photomultiplier tube
Ps	Positronium
p-Ps	Parapositronium
RGS	Rare gas solid
RW	Rotating wall
SEM	Scanning electron microscope
SSPALS	Single-shot positron annihilation lifetime spectroscopy

List of Figures

List of Tables

Chapter 1

Introduction and Motivation

Antimatter physics is an exciting field of research within particle physics that may contribute to an increased understanding of fundamental physical laws. The Standard Model is a theory which gives us a good understanding of particle physics. This model classifies all known subatomic particles, and concerns three basic physics interactions: the strong force, the weak force and the electromagnetic interaction. A consequence of the Standard Model is that most particles have an associated corresponding antiparticle. For example, electrons have positrons (antielectrons) as their counterpart, and protons have antiprotons. In the same way that electrons and protons can be combined to form atoms, positrons and antiprotons can be combined in order to form atoms of antimatter.

One of the largest research centres in the world focused on antimatter is the Antiproton Decelerator (AD) facility at CERN, where several experiments are currently active. These experiments mostly focus on producing cold antimatter atoms, and further using atomic spectroscopy for systematic studies of the properties of antimatter. The production of significant amounts of neutral antimatter is a complex task, as antiparticles annihilate upon contact with matter. The main difficulties in this type of work is therefore related to the storing and handling of antimatter. For instance, the electromagnetic traps used for storing antimatter require an ultra-high vacuum environment, a strong magnetic field for particle confinement and, in the case of antimatter atoms, an internal temperature close to 0 K.

The aim of the AEGIS collaboration (Antimatter Experiment: Gravity, Interferometry, Spectroscopy) is to measure the Earth's gravitational acceleration $\bar{g}$ on antimatter atoms [1]. The inertial masses of antiparticles are identical to their corresponding particles, from what can be determined by experiments such as measuring charged particles in a magnetic field. However, the movement of antiparticles in gravity, and therefore their gravitational mass, has never been measured directly. It is not practical to do this mea-

surement on charged particles due to the disturbances from surrounding magnetic and electric fields [2], and AEGIS will therefore employ neutral antimatter atoms.

Antihydrogen is the type of stable, neutral atomic antimatter that is the easiest to produce, and consists of one antiproton and one positron. It is also the best alternative for experiments whose goal it is to produce cold antimatter. The first method for producing cold antihydrogen was developed and used by the ATHENA collaboration [3] and then improved by the ALPHA collaboration [4], both situated at CERN. This method consists of setting up a specific configuration of magnetic and electric field inside a particle trap, in order to create an overlap between a cloud of cold antiprotons and a cloud of positrons. This creates cold antihydrogen, albeit at a low efficiency.

Different methods for increasing the antihydrogen productivity have been proposed in the last decade by experiments in the AD facility. One of the most interesting methods, in terms of the interaction cross section and the amount of antihydrogen formed, is the positron capture by an antiproton that interacts with an excited positronium atom. Positronium is a bound state between an electron and a positron, and is therefore a neutral bound state. The main advantage of this method is that the efficiency of the antihydrogen production is expected to be much higher for the excited positronium, both compared to using ground state positronium and earlier production techniques. This approach has been chosen by the AEGIS collaboration for producing cold antihydrogen for measurements of the gravitational acceleration upon antimatter atoms.

The task of efficiently creating and exciting positronium is in itself very complex, and the AEGIS collaboration therefore has a separate dedicated system to study this. The purpose of this system is to investigate the formation and subsequent excitation of positronium to highly excited (Rydberg) levels outside of the ultra-high vacuum and cryogenic environment of the main antihydrogen experiment, in order to gain control and understanding of the excitation process. Positronium formation is accomplished by implanting positrons into specialised positron-positronium converter materials, whereupon the formed positronium is ideally emitted back into vacuum. The excitation is achieved by illuminating the emitted positronium with intense UV and IR laser pulses.

This thesis reports work done at the AEGIS collaboration at CERN and describes the efficient formation of positronium and subsequent positronium laser excitation, which is needed for a high antihydrogen yield. Improvements of the positron transport and positronium signal detection will be described as a preparation for these measurements. The theory of positron beams and positronium formation is reviewed in detail, and an overview is given of the positronium laser excitation. Additionally, a thorough description of the experimental apparatus and positron-positronium converters is given.

The experimental work was carried out as a part of a larger collaboration, which has understandably affected the underlying conditions and the way that the work was carried out. The work and results presented here have been expanded from the initial plan and topic of the thesis. The original plan included improvements of the positron transport and testing of several positron-positronium converter targets in order to efficiently produce positronium. These experiments progressed faster than expected, and it therefore became possible to make the first attempts at positronium laser excitation in this system. Furthermore, several detectors were available for positronium detection, and some interesting results from comparing these detectors are included.

This work has involved operation and maintenance of the positron system, and various tasks related to the different experiments performed. The author was involved in all of the experiments that are presented in Chapter 4, which encompassed both carrying out the measurements and planning the progression of the work. Notable responsibilities include the production of new positron-positronium converters, and subsequent investigation and comparison of these. Additionally, maintenance work was carried out on the entire cryogenic and vacuum systems of the main experiment. This work included handling of cryogenic liquids, operation of the vacuum system, and the regular use of an 10 ton overhead crane to transport experimental equipment.

Chapter 2

Theory

This thesis is a continuation of work presented earlier by the author [5], and much of the same theory is therefore still relevant. Parts of the following material are for that reason derived from the text presented in the earlier work. This chapter contains the theory required to explain the construction of positron beams and positronium formation. In addition, it gives the background for understanding the results obtained during this work and the discussion of these results.

2.1 Positron Creation

The positron (e^+) is the antiparticle of the electron, and has a positive charge and positive magnetic moment. Hence positrons behave oppositely to electrons in electromagnetic environments. Otherwise, within current experimental limits, the inertial mass of positrons and electrons is exactly the same. The Dirac wave equation published in 1928 [6] allowed for negative energy states of the electron, which Dirac later hypothesised was related to a new particle with the same mass as an electron, but opposite charge. The positron was first observed in 1932 by C. D. Anderson [7], in cloud chamber studies of the composition of cosmic rays.

Positrons can be produced either by radioactive decay or by pair production. In the case of radioactive decay, a radioactive source undergoes β^+-decay. This decay results in the transformation of a proton (p) into a neutron (n), with an accompanying formation of a positron and a neutrino (ν_e). In the latter case, high-energy electrons (e^-) are bombarded into dense materials so that *bremsstrahlung* is created, which consists of energetic photons (γ) created from the deceleration of the electrons. The photons can in turn produce

positron-electron pairs. These reactions are shown in Equations 2.1a and b [8, 9].

$$p \rightarrow n + e^+ + \nu_e \tag{2.1a}$$

$$\gamma \rightarrow e^+ + e^- \tag{2.1b}$$

Both methods produce positrons with a high mean energy and a large energy spread. Many experimental and industrial applications require that positrons have a narrow energy spread, and a process is therefore needed to slow down - or *moderate* - positrons. Moderation is described in more detail below.

Positrons in vacuum are stable particles, but those that come in contact with normal matter will annihilate with electrons. Annihilation is a process where positrons collide with electrons and change into high-energy photons, generally referred to as gamma (γ) rays, resulting in the loss of the two particles. The most common annihilation reaction is shown in Equation 2.2 [10], wherein two gamma rays are emitted subsequent to the annihilation.

$$e^+ + e^- \rightarrow 2\gamma \tag{2.2}$$

Both gamma rays will be emitted with an energy of 511 keV, which is the electron (or positron) rest mass, as long as the electron and positron involved in this annihilation are both at rest. These gamma rays are also emitted in opposite directions as long as the particles are at rest.

2.1.1 Radioactive Sources

Positively β-decaying radioisotopes are used in many positron laboratories as sources. The most commonly used radioisotopes are ^{64}Cu, ^{58}Co and ^{22}Na. The half-life of ^{64}Cu is quite short at 12.7 hours, while the half-lives of ^{58}Co and ^{22}Na are longer (71 days and 2.6 years, respectively). ^{22}Na is usually the preferred radioisotope, as many positron experiments are active over several years. The most common decay reaction is shown in Equation 2.3 [11]. In this process a proton decays into a neutron, resulting in ^{22}Ne. A positron is emitted to preserve the charge balance, together with a gamma ray with an energy of 1.27 MeV.

$$^{22}Na \rightarrow \ ^{22}Ne + e^+ + \nu_e + \gamma \tag{2.3}$$

^{22}Na has a branching ratio of 0.906 for positrons, which means that it emits a positron in 90.6% of all decay events, with energies up to 543 keV. The total decay scheme is shown in Figure 2.1.

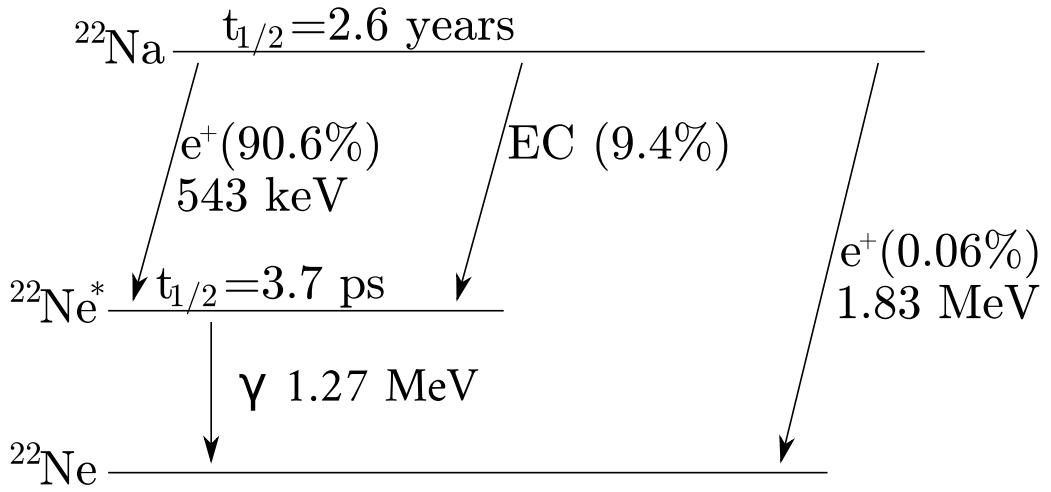

Figure 2.1: Decay scheme for ^{22}Na [11]. A positron with an energy of 543 keV is emitted in 90.6% of the decay reactions, which first produces excited neon and then ground-state neon by the emission of a photon (1.27 MeV). 9.4% of the decay events happen by electron capture (EC) and then photon emission, while a very small fraction (0.06%) occurs by the emission of high-energy positrons (1.83 MeV). The accompanying neutrino emission is not shown in this figure.

2.1.2 Accelerator Sources

Linear particle accelerators (LINACs) are usually needed to generate positrons by pair production. When using LINACs, high-energy electrons can be shot into high-Z materials, where positrons are created after the generation of bremsstrahlung [12]. In this technique, positrons are created with energies extending almost up to the impact energy of the electrons. This implies that the minimum energy required for a LINAC to produce positrons is twice the rest mass energy of the particles, as both electrons and positrons are made during pair production. Positrons are then controlled by magnetic and/or electric fields, and moderated to lower energies.

LINACs are very expensive machines, but the produced positrons can be shared among many users. Pair production via LINACs also has the advantage of a very high particle flux. Despite this, many positron laboratories use β^+-decaying radioisotopes [13–15], and the radioisotopes seems to be favoured over LINACs for the production of slow positrons.

2.2 Positron Moderation

Both radioactive sources and LINACs produce positrons at energies up to the positron rest mass energy mc_0^2 and with a large energy spread ΔE. These positrons are impractical to work with in most experimental settings, due to resulting problems with spectroscopy measurements and the inability to form larger bunches of positrons. To optimise the

number of positrons that can be trapped in vacuum, most experiments require a beam of low average energy and narrow energy spread. Positrons with a kinetic energy in the eV range are typically required for optimal trapping. In order to solve this problem, one could consider using techniques such as removal of unwanted positrons by cutting them away with electrical filters and apertures. These techniques are often used in order to obtain electrons with a narrow energy distribution. However, the number of available positrons is generally much smaller than electrons in similar set-ups, and the low efficiency of apertures therefore leads to a loss of positrons which is undesirable for most positron systems.

To maximise the number of positrons that are available for manipulation and storage it is therefore necessary to *moderate* the positrons, a process which is the starting point for forming of a high-quality positron beam. When positrons interact with a solid material, a fraction of the positrons may be re-emitted from the surface with a low mean energy, a narrow energy spread and a small angular distribution. Figure 2.2 shows a comparison of the typical energy spectrum of moderated positrons to that of positrons emitted from a radioactive source.

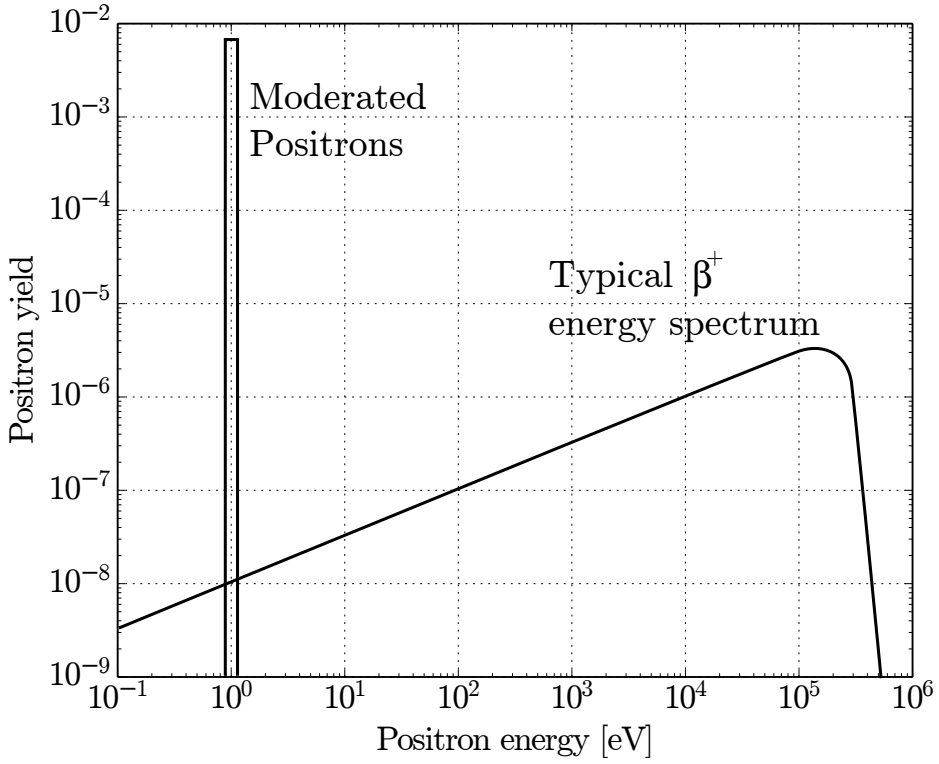

Figure 2.2: Typical spectra of the positron energy, before and after the moderation process, demonstrating the increase in the amount of low-energy positrons. The initially broad energy distribution becomes very sharp following moderation, with an energy spread in the order of a few eV. Image after [16].

The fraction of positrons that are emitted from the moderator is called the *moderator efficiency* ϵ, and can be defined as in Equation 2.4 [16]. Currently, the efficiency of all initial moderation lies below 1%, which means that over 99% of the positrons annihilate inside the moderator.

$$\epsilon = \frac{\text{number of slow positrons from moderator}}{\text{number of positrons from source}} \tag{2.4}$$

The working mechanism of moderators lies in the nature of positrons and their behaviour in solids. When a positron is shot into a solid its kinetic energy decreases very rapidly due to several physical processes, such as inelastic collisions, which will be described in more detail in Chapter 2.5. Positrons in the bulk of a material will generally reach thermal equilibrium within a very short timescale (∼10 ps). Thermalised positrons can then diffuse through the solid for a few hundred picoseconds, and most positrons are lost to annihilation events against electrons. However, a fraction of the diffusing positrons will reach the surface of the solid, where they may be emitted into the vacuum. The characteristics of these positrons will depend on the solid from which they are emitted, and the next section details the two commonly used types of moderators.

2.2.1 Metal Foil Moderators

In order to remove a positron from the material one would typically have to supply an ionisation energy, where the minimum ionisation energy is given by the work function of the material. The work function of an electron (ϕ_-) is defined as the energy needed to move an electron from the bulk of a solid to outside the surface. There are two contributions to the work function: the surface dipole barrier (D) and the chemical potential of the electron (μ_-). The positron work function (ϕ_+) is determined in the same way as the electron work function, where the chemical potential of the positron (μ_+) is defined as the difference between the lowest positron band and the crystal zero, which is the average potential between the atoms of the crystal. The dipole barrier D is a small electric dipole layer at the surface that originates from a spill-over of electrons into the vacuum, which shifts the crystal zero by an amount D towards the vacuum. D is positive for electrons, and negative for positrons. The total work function for electrons and positrons can be found in Equations 2.5a and b [17].

$$\phi_- = +D - \mu_- \tag{2.5a}$$

$$\phi_+ = -D \pm \mu_+ \tag{2.5b}$$

Note that in the case of electrons, the chemical potential has to be subtracted. For positrons, the chemical potential is either subtracted or added, depending on its position relative to the crystal zero. ϕ_+ can therefore have a near-zero or even negative value, which makes it possible for the positrons to be spontaneously emitted from the surfaces of some materials.

Metal foils have been popular as positron moderators, as many metals have negative positron work functions and emit positrons quite efficiently. The first successful attempt at a slow positron beam was made in 1958, and used a chromium-plated mica surface as a moderator, with an efficiency of $\epsilon \sim 3 \cdot 10^{-8}$ [18]. Moderators have become progressively better in the decades after this, where the best single crystal moderator to date is W with $\epsilon \sim 3 \cdot 10^{-3}$ [15, 19]. These moderators can be made with either single crystal or polycrystalline materials, and with different geometries. Three typical moderator geometries are illustrated in Figure 2.3. Back-scattering is the simplest of these geometries and have been used with both ^{22}Na and ^{58}Co sources. Back-scattering moderators are quite easy to realise as they do not require a thin, self-supporting film, but the efficiency is lowered because the source blocks some of the positron flux. The Venetian blinds have been used with polycrystalline materials, which are generally simple to produce. The disadvantage is of course that the moderator geometry is more complex than the back-scattering one. The transmission geometry appears to be the best of these three geometries, combining a simple design and a high ϵ.

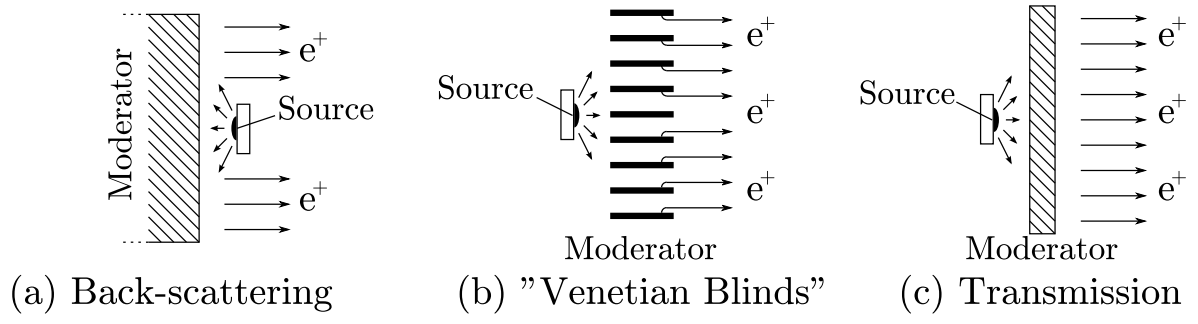

Figure 2.3: Three common moderator geometries, after Schultz and Lynn [17].

Although polycrystalline materials are much easier and cheaper to fabricate than single crystal films, the large amount of grain boundaries and defects means that more positrons are trapped inside the material and unable to reach the surface. Contamination on the moderator surface also plays an important role in the moderator efficiency. The emission of thermalised positrons is only energetically favourable when the positron work function is negative (or close to zero), so surface contaminants or defects that increase the work function will decrease the efficiency. For many metal foils, good moderation qualities are achieved by annealing at a high temperature after installation near the source [20, 21].

2.2.2 Rare Gas Solid Moderators

Rare gas solid (RGS) moderators have emerged as an alternative to the metal foil moderator. The slowing down of positrons in rare gas solids is similar to that of metal foils, where the initial energy loss is due to inelastic collisions with the ion lattice. Contrary to metal solids, rare gas solids are insulators with band gaps ranging from about 9.3 eV (xenon) to 21.4 eV (neon) [22]. Below a certain level, the positron energy in materials with a wide band gap is mostly lost by creating excitons or by positronium formation. However, due to the inelastic collisions the energy quickly drops below the threshold for these processes. Energy loss below this point is very slow as the only available process is phonon excitation. All rare gas solids have small but positive positron work functions (<10 eV), which means that positrons can only be emitted from the surface if their kinetic energy is larger than the work function. As positrons thermalise relatively slowly in rare gas solids due to the band gap, a large fraction of positrons will therefore have enough energy to overcome the surface barrier despite the work function being positive. This process is described by the *hot positron model* [23, 24].

Due to the slow thermalisation, positrons emitted from an RGS moderator typically have a larger energy spread than those emitted from single crystal films. The energy spread is important in positron trapping systems where the trapping potentials are tuned to certain positron energies, and a large energy distribution will lead to a lower trapping efficiency. The disadvantage of the large energy spread in RGS moderators is compensated by a large increase in moderator efficiency as compared to metal foils [15]. Table 2.1 shows a comparison of efficiencies, energy spread and positron work function for a variety of different moderators based upon available data.

Table 2.1: Efficiency ϵ, energy spread ΔE and positron work function ϕ_+ for a selection of moderators. The first four materials are rare gas solids, while the two last materials are used as metal foil moderators.

	Ne	Ar	Kr	Xe	W	MgO
ϵ (%)	0.70[a]	0.13[a]	0.14[a]	0.13[a]	0.32[b]	0.001[c]
ΔE (eV)	0.58[a]	1.7[a]	1.8[a]	3.2[a]	0.7[b]	1.5[c]
ϕ_+ (eV)	>5.5[a]	1.7[d]	1.5[d]	1.6[d]	-3.0[e]	-

[a] After A. P. Mills and E. M. Gullikson [23].
[b] After A. Vehanen *et al.* [19].
[c] After K. F. Canter *et al.* [25].
[d] After E. M. Gullikson and A. P. Mills [24].
[e] After Schultz *et al.* [26].

RGS moderators are typically made by introducing the gas in the source chamber and freezing it directly onto the source holder, which means that the shape of the holder determines the moderator geometry. So although the main advantage of RGS moderators is the increased efficiency, another benefit is the fact that they can be remade by evaporating the old moderator and introducing new gas. Consequently, if the moderator efficiency decreases due to a build-up of impurities on the surface, it can simply be remade to ensure a higher ϵ. On the other hand, rare gases solidify at very low temperatures and low pressures, and thus require both cryogenic units and vacuum systems. New geometries have appeared together with these moderators, as RGS moderators are mostly constrained by the geometry of the source holder. Designs that have been used so far include cylindrical, parabolic and conical source holders, which all provide large surfaces for positron absorption and re-emission [27].

2.3 Positron Trapping

For some types of positron experiments such as Doppler broadening measurements for material characterisation [28], it is sufficient to use a relatively small and continuous flux of positrons directly from a positron source. If greater positron fluxes are required, it is possible to use a stronger radioactive source or a more intense LINAC beam. However, these methods are often very expensive, and over a certain limit it becomes almost impossible to further increase the flux. An alternative to this, as long as a continuous beam is not necessary, is to stack and accumulate the positrons in a trapping apparatus. The use of a trap enables cooling and compression of the particles, and the available positrons can become concentrated into fewer bunches.

In the context of positron systems, the term 'positron beam' will refer to a compressed plasma of positrons, with a typical number in the range of 10^6-10^8 particles. The line between non-plasma and plasma is not sharply defined, as it depends on the number of particles and the dimensions of the positron cloud. The term plasma is generally used when the positrons display collective behaviour, such as Debye shielding. Debye shielding occurs when the external electrical field is shielded from the interior of the plasma. This is true for positron clouds with more than 10^6 positrons, with typical beam dimensions [29].

The most commonly used apparatus for trapping positrons is the Penning-Malmberg (PM) trap. This apparatus, in addition to its most important developments, will be outlined in the sections below. A more detailed physics description of PM traps and the behaviour of trapped particles can be found in for example [30].

2.3.1 Penning-Malmberg Trap

The Penning-Malmberg trap uses a combination of magnetic and electric fields to trap particles [31]. A solenoid provides a homogeneous and longitudinal magnetic field, which radially confines the positrons. The electric field is provided by a number of cylindrical electrodes. These electrodes are set to different potentials in order to make a potential well, with the lowest potential on the middle electrode. This confines the positrons in the longitudinal direction.

An important improvement of the PM trap is the use of a buffer gas inside, which acts to lower the energy of positrons entering the trap. This technique was developed by Surko *et al.*, and a PM trap which employs buffer gas for cooling energetic positrons is therefore called a Surko trap [32]. These traps usually have several stages, each with successively lower gas pressure and electrostatic potential. The layout of a typical Surko trap can be found in Figure 2.4.

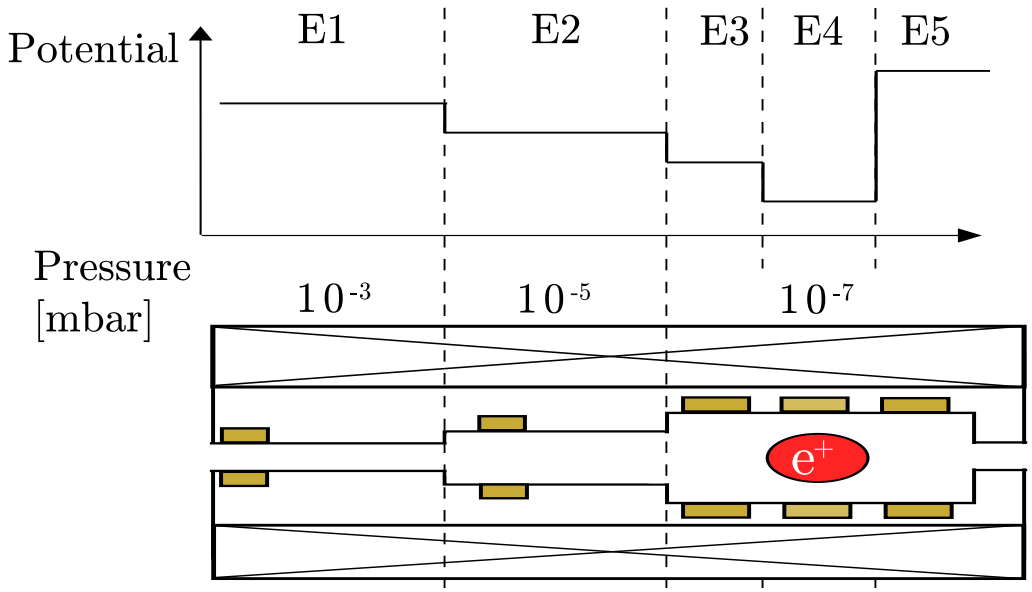

Figure 2.4: A Surko trap, with the Penning-Malmberg type of particle confinement and buffer gas [16]. The positrons are confined radially by a longitudinal magnetic field, and they become confined axially by the electrodes E3-E5 in a potential well after having lost enough energy. Cooling takes place in the regions of the electrodes E1-E4, where the gas pressure decreases gradually from the entrance of the trap. The decreasing gas pressure gives an optimal cooling process by inelastic scattering, while at the same time providing a relatively long lifetime.

It may initially seem very counterintuitive to introduce a gas inside the trap, as the positrons will ultimately annihilate against the electrons in the gas atoms and molecules. However, only a small number of positrons will be stored in the trap in the absence of buffer gas, as many of the incoming positrons become reflected on the potential of the

last electrode E5 and travel back to the source. With a buffer gas present, the positrons may lose enough energy via collisions to become trapped by the electric field.

In order for the cooling to be practical, the positrons have to lose energy to inelastic collisions with other particles at a high efficiency. As the positrons cool down, they should no longer be able to overcome the potential of the preceding stage of the trap, and will thereby not be able to escape in the upstream direction of the beam line. With reference to Fig. 2.4, this means that energetic positrons are admitted at E1 and gradually lose energy to the buffer gas, and as they travel to the region of electrode E2 they should be unable to return to the region of electrode E1. Eventually the positrons become trapped in the bottom of the potential well. The Surko trap is constructed so that each stage has a lower electrode potential and a lower buffer gas pressure. This maximises both the positron lifetime and yield in the trap. In practice, this is in some cases be accomplished by constructing the trap with several tubes with increasing diameter, which are then differentially pumped.

The cooling time and the lifetime for positrons inside the trap will depend on the density and type of buffer gas. For the cooling process to be efficient, the buffer gas must have a small cross-section for annihilation and a large cross-section for inelastic processes such as rotational and vibrational excitation. A good buffer gas for the initial cooling is N_2, as it cools positrons very efficiently by electronic excitation ($E > 8.6$ eV) [33]. Below this energy N_2 becomes quite inefficient as electronic excitation is no longer the dominant process for inelastic collisions. In order to cool down the positrons further, gases like SF_6, CF_4 and CO_2 may be introduced, which mostly cool by vibrational and rotational excitation (8.6 eV $> E > 0.05$ eV) [34]. For positron energies lower than this ($E < 50$ meV), the nitrogen gas again becomes important as the positrons lose energy by vibrational and rotational excitation of N_2 down to room temperature. Up to 30% of the incoming positrons become trapped in the last stage of the trap due to the buffer gas cooling, and they cool down to room temperature in $\sim$0.1 s.

A common arrangement for the creation of slow positron beams, as in the AEGIS positron system, is to have two trapping stages. The first trapping stage is then a Surko trap with a high buffer gas pressure, and the second trap is a PM trap that can accumulate large amounts of positrons. This will be explained further in Chapter 3.

2.3.2 Other Cooling Mechanisms

An alternative to the buffer gas is to use a strong magnetic field that cools the positrons by cyclotron radiation [31]. An advantage of this technique is that the number of positrons is completely preserved (no losses). However, cyclotron radiation is only observed for very

strong magnetic fields (in the order of ∼T), which can be both difficult and expensive to generate.

A limitation for both buffer gas cooling and cyclotron cooling is that the positrons can only reach a temperature equal to the temperature of the surroundings. A method has been developed for further cooling positrons to a lower temperature [35]. This method involves sympathetic cooling of positrons with previously laser-cooled ions, where the two species are confined in the same trap. This cooling technique has been shown to result in a positron plasma at <5 K in a room temperature trap, with a potential for achieving temperatures down to 100 mK.

2.3.3 The Rotating Wall Technique

In theory, a positron plasma confined in a PM trap could have an infinite lifetime. However, even in a perfect vacuum the lifetime is limited because the positron cloud will start to expand due to inherent field asymmetries [36]. Scattering on background gas molecules will also contribute to the annihilation rate. By applying a rotating electric field, a so-called rotating wall (RW), this effect can be counteracted so that the radial expansion stops. As the dimensions of the positron plasma are kept constant, the lifetime of the particles will increase. The plasma can even become compressed, if the rotating wall exerts a great enough force. [37].

The RW technique is implemented by using one of the central trapping electrodes in the PM trap. The electrode for the RW is segmented into four parts and a sinusoidal voltage is applied to each segment individually with a phase difference of 90°. For the positrons, the forces induced from this electrode will appear to be rotating. Since the rotating wall exerts a force on the positron plasma, the positrons become more energetic and the temperature of the plasma will increase. A very small buffer gas pressure ($\sim 10^{-8}$ mbar) is enough to counteract the heating, and is usually used together with the RW.

A positron plasma in a magnetic field B with the density n_p will rotate around the axis of the magnetic field with the frequency f_E, as defined by Equation 2.6 [29]. In the normal regime of the rotating wall, the frequency of the plasma will usually not be related linearly to the RW signal f_{RW}. Therefore, it is not easy to predict how much the plasma will be compressed for different values of f_{RW}. A recent development of the rotating wall application is the discovery of the so-called strong-drive regime by Cassidy *et al.* [38]. In this regime, there is a direct relation between the applied RW signal and the rotation frequency of the positron plasma, so that $f_E = f_{RW}$. Hence there is a linear relationship between the RW frequency and the plasma compression, and strong-drive compression therefore enables better control of the achievable plasma density. The RW frequency can

be used to change the plasma density up to the Brillouin limit $n_{p,max}$, which is defined by the magnetic field and the positron mass (m_e) given by Equation 2.7 [39]. This is the fundamental limit of plasma compression because the internal potential of the plasma is in equilibrium with the magnetic field, and occurs when the plasma is rotating with half of the cyclotron frequency.

$$f_E = \frac{n_p e}{4\pi\epsilon_0 B} \tag{2.6}$$

$$n_{p,max} = \frac{\epsilon_0 B^2}{2m_e} \tag{2.7}$$

ϵ_0 in the above equations is the permittivity of free space, while e is the positron charge and m_e the positron mass.

Some aspects of the RW compression are still poorly understood at present, but it seems that the strong-drive regime is only achievable when the axes of the magnetic field and accumulator are accurately aligned. Nevertheless, the RW technique is very useful even without the strong-drive regime, as the positron lifetime in the trap increases and the diameter of the plasma can be reduced down to a fraction of the electrode diameter.

2.4 Positronium

Positronium (Ps) is the bound state of a positron and an electron, sometimes called an exotic atom. Ps is purely leptonic, and is the lightest bound state of two particles known. It was experimentally discovered in 1951 by Deutsch [40,41]. This state is usually described as being quasistable since Ps has a binding energy of 6.8 eV, but annihilates relatively fast in the order of pico- or nanoseconds.

An important property of positronium is the spin state. Ps can exist in two different configurations, according to the spin orientations of the two particles [42]. The spins of the electron and positron are anti-parallel in the singlet state, which results in a total spin of 0. This state is known as parapositronium (p-Ps). Positronium can also be formed in the triplet state, where the two particle spins are parallel and the total spin is 1. This state is referred to as orthopositronium (o-Ps). The relative amount of p-Ps:o-Ps made during Ps formation is 1:3, which can be derived on kinematic grounds. p-Ps typically annihilates with a lifetime of 125 ps [43], emitting two photons each with an energy of 511 keV (2γ-annihilation). For o-Ps the lifetime is 142 ns [44], where three photons are emitted with a total energy (1022 keV) that is randomly divided between the three photons. Annihilation via one gamma ray (511 keV) is also possible for o-Ps, but is strongly suppressed as there is no additional body to accept the excess momentum from the process. A notable point here is that the lifetime of p-Ps and o-Ps differs by three orders of magnitude. These

annihilation lifetimes and photon energies are valid for positronium in vacuum and in ground state, that is with the principal quantum number $n = 1$.

Positronium as an atom is very similar to hydrogen, and many of its properties can be treated by scaling the properties of H [45]. For instance the Ps energy levels E_n^{Ps} can be calculated by scaling the H energy levels E_n^H as in Equation 2.8 [46].

$$\mathrm{E}_n^{Ps} = \frac{\mu_{Ps}}{m_e} Z^2 \mathrm{E}_n^H \tag{2.8}$$

In the above equation, m_e is the electron mass, and Z is the atomic number. For positronium, Z=1. The reduced masses of H and Ps are given in Equation 2.9a and b [46].

$$\mu_H = \frac{m_e m_p}{m_e + m_p} \approx m_e \tag{2.9a}$$

$$\mu_{Ps} = \frac{m_e}{2} \approx \frac{\mu_H}{2} \tag{2.9b}$$

The Ps radius can also be found by scaling the H radius, as given in Equation 2.10 [46], and the radius is then found to be twice that of hydrogen.

$$a_{Ps} = \frac{\hbar^2}{\mu_{Ps} e^2} = 2a_0 \tag{2.10}$$

Here, a_0 is the Bohr radius and $\hbar$ is the reduced Planck's constant. From Eq. 2.8 and Eq. 2.10 it can be seen that the positronium energy levels are scaled down by a factor of two as compared to hydrogen, while the radius is increased by the same factor.

2.5 Positron-Matter Interactions

Positrons implanted into matter will rapidly lose their energy, and can interact with the material in different ways before annihilation occurs. These processes are described in the following section. This is intended as a brief overview of positron-matter interactions, and will therefore not contain the details of all possible cases. A more in-depth discussion of all the processes outlined here is made by Puska and Nieminen [47].

A summary of the different interactions can be seen in Figure 2.5. Positrons that arrive at a surface can either be implanted into the material, or they can be back-scattered (case 1 in Fig. 2.5). The size of the fraction of back-scattered positrons will depend mainly on the atomic number of the material, the energy of the incoming positrons and their angle relative to the surface of the material [48].

The high-energy positrons that are able to enter the solid lose energy to the sur-

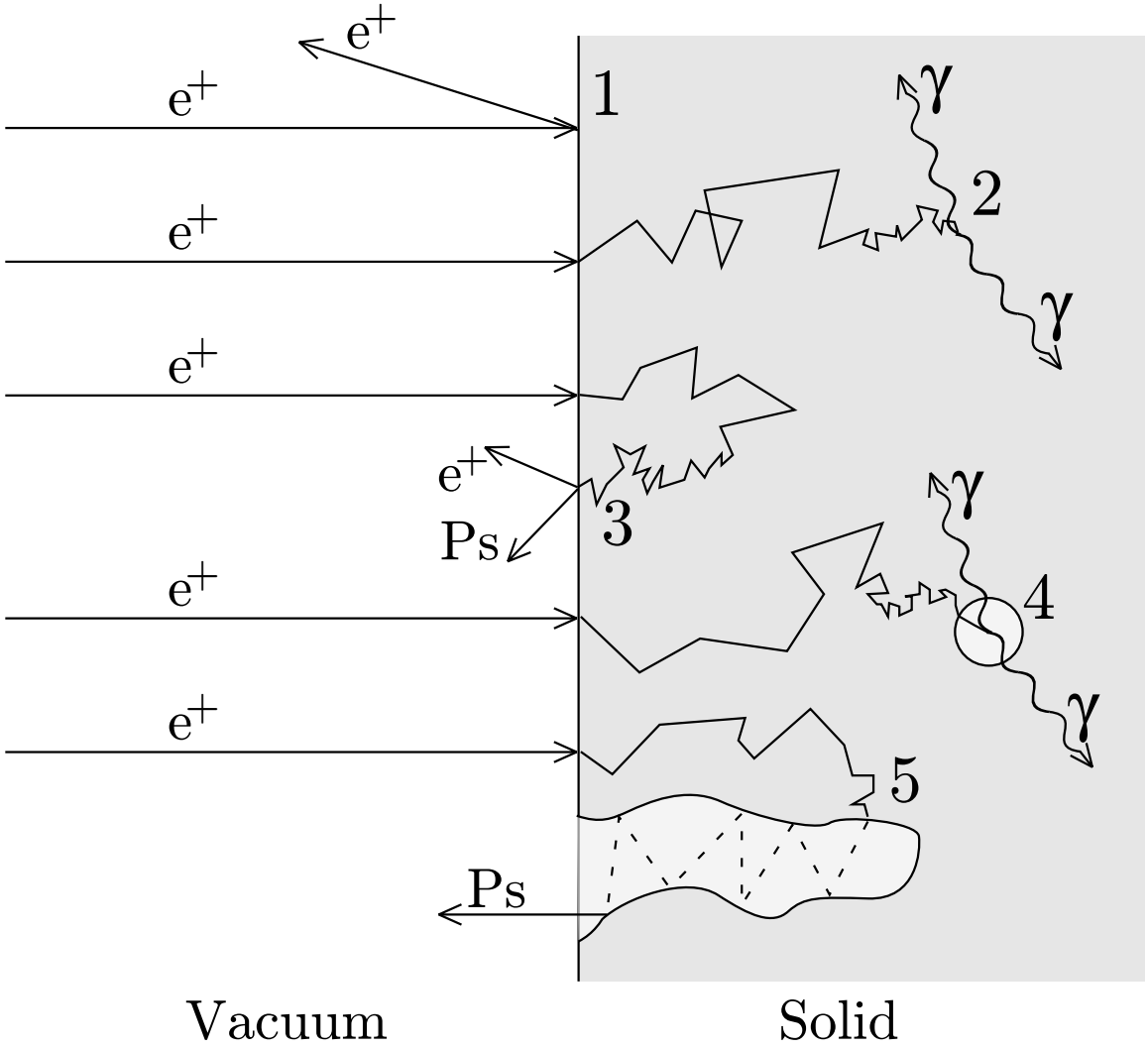

Figure 2.5: Schematic overview of some of the different processes that positrons can undergo when implanted into solids [5].
1: Back-scattering of high-energy positrons.
2: Thermalisation, diffusion and eventually annihilation in the material.
3: Re-emission of either positrons or positronium after thermalisation and diffusion.
4: Annihilation of a positron or positronium atom trapped in a defect.
5: Formation of positronium in defects that are connected to the surface, and subsequent escape into vacuum.

rounding lattice and are typically thermalised within a few picoseconds. The positrons thermalise by a series of processes, and an overview of these is given in Table 2.2. The initial thermalisation is caused by inelastic scattering on valence and core electrons, which causes electron excitation, as well as scattering on atomic nuclei. These processes are important at an energy ranging from 100 keV down to a few electronvolts, or a fraction of an electronvolt in the case of metals, and takes most of the positron energy in the order of femtoseconds. The next process for energy loss is the excitation of plasmons and excitons in the material. Plasmons are quantified oscillations in the free electron density,

while an exciton is a bound state of a electron and a vacancy. The exciton vacancies are located in the valence band in semiconductors, and can occur in metals as an interband phenomenon. The thermalisation slows down below a few eV, as the main mechanism of energy loss becomes phonon excitation. Phonon excitation will start to dominate in insulators and semiconductors when the positron energy becomes smaller than the band gap energy. This process will dominate much later in metals, as the interband energy is much smaller than the band gap energy.

Table 2.2: Processes that positrons undergo while thermalising in solids. It takes only a few picoseconds for high-energy positrons to reach the same energy E_{th} as the environment.

Positron energy	Dominant effect
$E \gg E_{th}$	Inelastic scattering on nuclei and electrons
$E > E_{th}$	Plasmon and exciton excitation
$E \approx E_{th}$	Phonon excitation

Thermalised positrons move around by diffusion, and will eventually annihilate with an electron if they remain in the material, as in case 2 in Fig. 2.5. In essence, thermalised and diffusing positrons can be described as delocalised Bloch states. This annihilation inside the material can also follow after the formation of positronium in bulk, if binding to an electron is energetically favourable. Implanted positrons can penetrate materials to depths ranging from a few nanometres to some micrometres, depending on the positron beam energy and material density.

A fraction of the implanted positrons will diffuse back to the surface of the material, both thermalised and before complete thermalisation. When positrons are embedded in a material, their annihilation rate increases due to the local density of electrons and consequently the positron lifetime decreases. The typical positron lifetime is $\sim$100 ps, which is relatively long compared to the thermalisation time of a few picoseconds. Thus, positrons can diffuse through the solid most of their lifetime as thermalised or nearly thermalised species, and have the opportunity to reach the surface of the material. One outcome of this can be a perpendicular emission of positrons from the surface, as in case 3 in Fig. 2.5. If the positrons are thermal they can only escape the surface if the work function of the material is negative, and they can only escape a positive work function material if they are epithermal. This is the process that is employed in moderators, and both moderators and work functions are explained in detail in Section 2.2. If the positron binds to an electron at the surface, it can also be emitted as positronium into the vacuum.

Positrons can also become trapped in the material as they diffuse, if they encounter

voids, defects or grain boundary interfaces. This is because many types of defects represent potential minima for the positrons. The wave function of the positron then goes from being delocalised to being very localised. In this case the positron will most likely annihilate inside the defect (case 4 in Fig. 2.5). The lifetime of positrons in defects can increase up to several hundred picoseconds, due to the relatively lower electron density in the defect. This change in lifetime depends on the type and size of the defects, and is the basis for positron spectroscopy of materials. For certain materials, the positron can pick up an electron and form positronium inside open-volume defects that are large enough ($\geq$1 nm) [49]. These trapped positronium atoms will also eventually annihilate. For larger pores that are connected to the surface of the material, it is possible for the positronium to diffuse through the pore and escape into back vacuum (instance 5 in Fig. 2.5). Positronium atoms that travel through pores typically experience many inelastic collisions with the pore walls, and can therefore escape into vacuum thermalised or nearly thermalised.

2.6 Positronium Formation and Spectroscopy

2.6.1 Positronium Formation

From the discussion above one can separate positronium formation into two distinct processes, namely formation in the bulk and formation on the surface of materials.

Ps Formation in the Bulk

Bulk formation can happen when the creation of Ps is more energetically favourable than the separation of the electron and the positron. If these Ps atoms do not reach a surface during diffusion, they will eventually annihilate. However, those that reach the surface have a chance of being emitted into the vacuum if their work function is negative, in the same way as for positrons. The positronium work function can of course be positive, in which case the positronium will not be emitted from the surface. This work function is shown in Equation 2.11 [17].

$$\phi_{Ps} = \phi_+ + \phi_- + E_B - \frac{1}{2}R_\infty \tag{2.11}$$

The work function ϕ_{Ps} consists of the separate work functions of the positron (ϕ_+) and the electron (ϕ_-), in addition to the positronium binding energy in vacuum ($\frac{1}{2}R_\infty$) and the smaller binding energy within the solid (E_B). The binding energy in vacuum is $\frac{1}{2}R_\infty \approx$ 6.8 eV, and E_B is smaller than this because the electron in the Ps atoms is affected by the repulsive forces of the surrounding electrons. Hence the formation of Ps in materials

releases less energy than in vacuum. The value of ϕ_{Ps} can be described as the energy needed to separate the positron and electron in the solid (E_B), in addition the the energy required to move both from the solid (ϕ_+ and ϕ_-), minus the energy gained by forming Ps again ($\frac{1}{2}R_\infty$). A negative work function of about 0.1 eV is favourable in the interest of forming Ps in the bulk material.

Ps Formation on Surfaces

Positrons may bind to electrons as they are leaving the surface of a material, thereby creating positronium. The formation of positronium on surfaces or in large defects can be described by the Ps formation potential, which is defined as in Equation 2.12 [17].

$$\epsilon_{Ps} = \phi_+ + \phi_- - \frac{1}{2}R_\infty \tag{2.12}$$

The formation potential ϵ_{Ps} consists of the individual work functions of the positron and the electron, as well as the binding energy $\frac{1}{2}\mathrm{R}_\infty$. The electron work function is always positive while the positron work function can be negative, which means that the total formation potential may be negative. When ϵ_{Ps} is negative, the formed Ps can be ejected from the surface with a relatively high energy in the order of eV.

Ps Formation in Metals, Semiconductors and Insulators

The behaviour of positrons in solids depends on whether the material is a metal, semiconductor or insulator, as these have very different densities of free, delocalised electrons [27]. Metals have a high density of delocalised electrons, which prevents the formation of Ps atoms in the bulk as the electrons screen the Coulomb attraction between the positron and any single electron. With reference to Equation 2.11, this means that the binding energy E_B decreases. In these materials, Ps formation has never been observed in the bulk of the material, and only happens at the surface. For implantation of high-energy positrons, this means that Ps formation requires a positron to diffuse back to the surface and acquire an electron before being emitted. Typically, the back-diffused positrons become trapped in a surface state and are eventually thermally de-trapped as positronium. Metals have a high density of available surface states, which means that surface formation of Ps can be quite efficient.

For insulators the formation of Ps at the surface happens with a much lower efficiency due to the lack of surface states. However, Ps can be formed in the bulk of insulators, since they have a lower electron density. Semiconductors lie between metals and insulators, and surface formation of Ps is generally favoured over bulk formation.

2.6.2 Positron-Positronium Converters

An important part of the AEGIS experiment is the formation of positronium, as it is a crucial part of the intended antihydrogen ($\bar{H}$) production process. The positron-positronium conversion should preferably lead to the formation of a large fraction of positronium atoms that are emitted into vacuum at thermal or nearly thermalised temperatures. Obtaining cold Ps atoms is important because it increases the efficiency of the antihydrogen formation (see Appendix A), while producing a large fraction of Ps atoms increases the total amount of antihydrogen atoms that can be produced.

As explained above, only some of the interactions between positrons and matter result in the formation of positronium. Moreover, only pure insulators seem to supply the thermal Ps atoms that are needed in the antihydrogen production, and the direct yield of these materials is inconveniently small. Another option for attaining cold Ps atoms is to first produce Ps at a slightly higher energy (1-3 eV), and then do the cooling in a second step. Methods for cooling Ps are being researched extensively, and two main approaches have been developed: cooling by inelastic collisions [50] and laser cooling for Ps atoms that are already at low temperatures. Only cooling via inelastic collisions is relevant for this work, and will be described in some detail here. Note that the fraction of p-Ps atoms can be disregarded here, as the lifetime of p-Ps is too short for this state to be useful for antihydrogen production and further experiments.

One way of realising cooling by inelastic collisions is to form positronium in porous insulating materials. In this way, the Ps atoms are formed inside the material, and can escape back into vacuum as long as the pores are connected to the surface. Some considerations must be taken in order to describe the expected cooling process of Ps atoms inside pores. Positronium atoms have a de Broglie wavelength λ_{Ps} as described by the well-known relation in Equation 2.13, which is defined by the positronium rest mass m_0 and the positronium energy E_{Ps}, as well as Planck's constant h.

$$\lambda_{Ps} = h/\sqrt{4m_0 E_{Ps}} \tag{2.13}$$

When the Ps atoms are trapped inside pores such as nanochannels, they will move around and interact with the walls of the pores, where the interaction is dependent on the dimension a of the pores. As long as λ_{Ps} is smaller than a, the Ps atoms behave as classical particles that undergo inelastic collisions against the walls [51]. These inelastic collisions continue until λ_{Ps} is on the scale of a, at which point quantum effects must be considered. One factor is that the scattering inside the channels must be treated by superimposing the wavefunctions of the Ps atom and that of several atoms in the wall. This gives a

certain probability for back-scattering on the walls, but also for entering the solid again, which reduces the thermal Ps yield for every collision. Another component of this is the quantum confinement of the Ps atoms. A channel can be modelled as an infinite potential well, with an associated minimum energy level for the Ps atoms. The minimum energy can be calculated from Equation 2.14a, which also gives a lower limit for the temperature that the Ps atoms can reach (as in Equation 2.14b) [52].

$$E_{Ps} = \frac{\hbar^2 \pi^2}{ma^2} \tag{2.14a}$$

$$T = \frac{2E_{Ps}}{3k_B} \tag{2.14b}$$

In order to thermalise positronium the energy would have to reach about 40 meV, which corresponds to a temperature of 309 K. This energy can be reached for $a \approx 6$ nm, and this implies that quantum confinement does not interfere with thermalisation as long as a is bigger than 6 nm. Positronium in channels smaller than this will not cool down to room temperature.

Cooling inside cavities can have adverse effects on the positronium production, as the positronium lifetime is generally shorter in cavities than in vacuum. This is mostly due to a phenomenon called pick-off annihilation, which in some cases can reduce the lifetime of o-Ps down to a few picoseconds. Pick-off annihilation occurs when the o-Ps atoms get sufficiently close to an electron with a spin anti-parallel to the positron. In this case, the positron will annihilate against the electron with anti-parallel spin rather than the one it is bound to. o-Ps annihilation by the pick-off mechanism will emit 2 gamma rays in the same way as annihilating p-Ps. Pick-off annihilation will therefore decrease the Ps lifetime in the material and diminish the maximum fraction of o-Ps that can be emitted into vacuum. The rate of pick-off annihilation varies with the material type, with the rate being higher for metals and semiconductor materials. Additionally, the pick-off rate changes with the dimension of the pore size and presently the research indicates that the rate decreases with increasing pore diameter [53].

Taking these factors into consideration, some observations can be made for what kind of material would make a good positron-positronium converter for the AEGIS experiment. An insulating material with pores connected to the surface would provide a good conversion efficiency, and would allow for thermalisation of the positronium atoms. The size and arrangement of these pores would have to be adjusted in order to optimise the positronium production and lifetime. Earlier experiments have tended towards using porous silica (SiO_2) as a converter, made either with ordered channels as pores, or disordered pores created with sol-gel methods [13, 54].

2.6.3 Detecting Positronium

Highly specialised techniques have been developed in order to observe and investigate positronium formation in materials, mainly based on detecting annihilation gamma rays. Two common techniques are described in the following, where the latter method has been used during this work.

Positron Annihilation Lifetime Spectroscopy

Positron annihilation lifetime spectroscopy (PALS) is a widely used method for investigating positron behaviour in matter and distinguishing positronium formation in different materials [55]. As mentioned earlier, positrons can exist in materials for up to a few hundred picoseconds before annihilating with electrons, whereupon the annihilation gamma rays can be detected. The basic principle of PALS is to implant single positrons into a material and measure the timing of the annihilation with respect to a start signal. The implantation is repeated numerous times in order to get a good statistical basis for the annihilation signals. Positronium in the material can be observed with this method because o-Ps typically has a lifetime much longer than the positron lifetime in the material, and therefore annihilates much later.

PALS requires that the positrons involved in the material implantation and positronium formation are temporally tagged. One way of doing the tagging is to implant single positrons at specific time intervals where the time is measured with high precision. The tagging thereby acts as a temporal start signal for the measurement. The positrons that are implanted into the material eventually annihilate, where some positrons may form positronium before the annihilation. The annihilation gamma rays are then picked up by photon detectors, and this acts as the stop signal for the measurement. By integrating all the gamma ray signals between the start and stop signals, a lifetime spectrum can be constructed. These lifetime spectra will typically have a large main signal (prompt peak) from the annihilation of positrons and p-Ps. If o-Ps is formed, it will be observable as a higher count rate in the time period after the prompt peak. PALS is utilised as an investigative tool in materials science, as both Ps formation intensity and lifetime depends on material properties. For instance, the Tao-Eldrup model [56, 57] and the related extensions of this model can be used to establish the pore structure in insulating materials.

Single-Shot Positron Annihilation Lifetime Spectroscopy

A method that has been developed recently and that circumvents some of the issues of PALS is single-shot positron lifetime spectroscopy (SSPALS) [58]. With this method, a large amount of positrons is implanted in a material all at one, and the resulting annihilation radiation is detected in real time. The lifetime spectra from SSPALS will look similar to those from PALS, but the data collection time of SSPALS is much shorter. Both SSPALS and PALS can be used for depth profiling of materials by varying the incident positron energy, but the time required to perform PALS means that SSPALS is much preferred for depth profiling. Spectra can then be obtained corresponding to different depths within a sample, which can be used for distinguishing between surface and bulk effects, and studying materials with different layers.

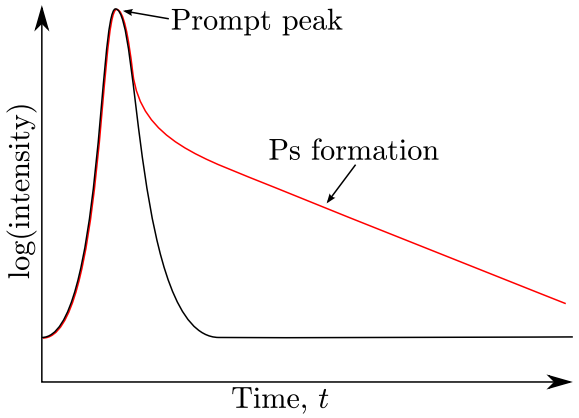

Figure 2.6: Examples of idealised SSPALS spectra. One spectrum shows positron annihilation and no positronium formation (black curve), and one spectrum shows evidence for Ps formation after the prompt peak (red curve).

The time resolution in SSPALS depends on the temporal width of the implanted positron plasma, and will therefore typically not be as good as the time resolution of PALS. Idealised SSPALS spectra (or integrated PALS spectra) with and without positronium formation can be seen in Figure 2.6. Real SSPALS spectra will have a quite high background noise due to several types of radiation not caused by positrons (cosmic rays, stray photons).

2.7 Positronium Laser Excitation

The mean lifetime of positronium can be enhanced up to the millisecond range by exciting positronium to a high-n (Rydberg) state. A Rydberg state is an electronically excited state where the principal quantum number n is typically 10 or more, and for positronium it is very similar to the excited states of hydrogen atoms. Excited positronium is usually denoted as Ps*. The excitation of Ps to Rydberg levels can be achieved by striking the positronium cloud with nanosecond laser pulses as the positronium atoms exit the converter material.

2.7.1 Achieving Rydberg excitation

Exciting positronium from ground state to a Rydberg level requires an energy of about 6.7 eV, which necessitates a UV radiation in the range of 180-185 nm. This wavelength is extremely difficult to achieve even with state of the art equipment, and direct excitation of Ps is therefore beyond the present technological capabilities. Additionally, most optical components, such as lenses and prisms, are highly absorptive at these wavelengths.

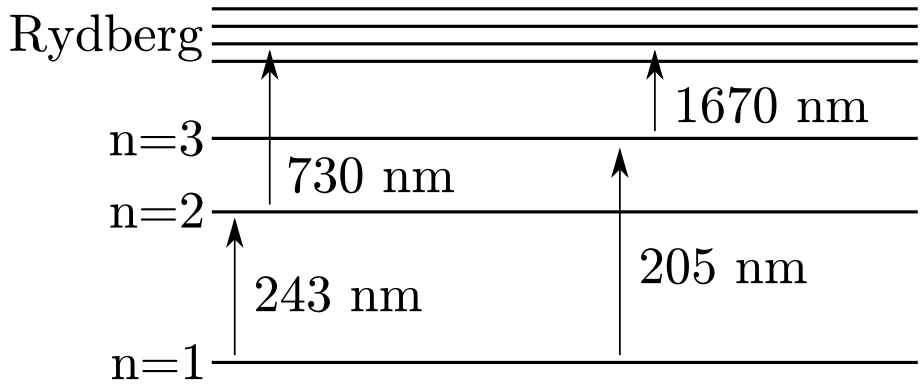

Figure 2.7: Two possible transition routes for positronium excitation to Rydberg states. The transition route on the right will be used in AEGIS, where the first transition of 1→3 will be done with a 205 nm laser pulse, and the second transition of 3→ n will be done with a laser pulse at ∼1670 nm.

A more efficient and realistic alternative for excitation entails the use of two laser pulses with different wavelengths striking the positronium. One laser pulse with UV wavelength would first excite Ps from the ground state to one of the first excited states (either $n = 2$ or $n = 3$). The second laser, being in the IR range, would give another kick to the excited Ps and thereby realise the transition to Rydberg levels. These two transition routes are shown in Figure 2.7. In the literature $n = 2$ is the most thoroughly investigated excited Ps state, both for testing theoretical models of Ps and as a stepping stone for Rydberg excitation [59, 60]. However, in the AEGIS experiment excitation of Ps to $n = 3$ will be employed. This is discussed in detail by Castelli [61]. The following sections will briefly explain the theory behind laser excitation of Ps and spectroscopy of excited Ps.

Excitation to n=3

The excitation of positronium to the $n = 3$ state (also denoted as the 3P state) is done via photon absorption by the ground state ortho-Ps produced and emitted by a positron-positronium converter, as shown in Eq. 2.15 [62].

$$Ps + \gamma \rightarrow Ps^* \tag{2.15}$$

The precise transition wavelength for this absorption process has been accurately calculated by Castelli [61], and is $\lambda_{1\to3} = 205.0474$ nm. This wavelength will have a certain uncertainty due to physical effects such as Doppler broadening and motional Stark effects.

To further compare with the alternative, the excitation to Rydberg via $n = 2$ requires two laser pulses with energies of ∼5 eV and ∼1.7 eV, and the lifetime of the $n = 2$ state is 3 ns. The excitation via the $n = 3$ state requires laser pulses with energies of ∼6 eV and ∼0.7 eV, and the lifetime of the $n = 3$ state is about 10.5 ns. Advantages of employing the $n = 3$ excitation is that it uses less overall laser power to reach saturation and avoids the problem with the very rapid decay of the $n = 2$ state back to the ground state. Additionally, between the competing processes of excitation to a Rydberg state and ionisation, the former is favoured because of the lower energy of the second laser pulse.

Excitation to Rydberg levels

Starting from the $n = 3$ level, positronium can be excited to Rydberg levels by photon absorption, where the photon has a wavelength of 1650-1700 nm depending on the intended Rydberg level. Efficient excitation to n between 10 and 25 has earlier been demonstrated using a slow positron beam [60], but with the $n = 2$ state as a step between the ground state and the Rydberg levels. The upper limit for Rydberg excitation is $n = 27$, after which ionisation starts to affect the positronium atoms [62].

2.7.2 Observing Laser Excitation

The fraction of Ps excited to the $n = 3$ state can be measured by observing the difference in lifetime between Ps and excited Ps. Two methods can be used for this purpose: quenching of the excited state in a magnetic field, or photoionisation with a second laser pulse [60].

As mentioned earlier, the 3P states of positronium will decay down to ground state in 10.5 ns in the absence of a magnetic field. In the presence of a magnetic field, the 3^3P state can be mixed with the 3^1P state due to the Zeeman effect. These excited Ps atoms will decay back to the ground state as p-Ps, where the p-Ps atoms annihilate with a lifetime of 125 ps by 2γ-annihilation. Photoionisation of the excited state will break the binding in the positronium atoms, releasing the positrons and electrons. The positrons will then annihilate relatively quickly against electrons in nearby materials.

Both of these processes lead to a decrease in the amount of o-Ps atoms that annihilate by 3 gamma rays, albeit in different ways: magnet quenching converts the Ps atoms from a triplet state to a singlet state, while photoionisation frees the positron from the Ps atom. In practice, the laser excitation can then be observed by comparing lifetime spectra acquired with the SSPALS technique, with the laser switched off and on. The

lifetime spectrum with the laser switched on should have an observable depopulation of the o-Ps annihilations following the laser pulse, as compared to the spectrum without the laser.

Positronium excited to the Rydberg state can similarly be observed in SSPALS spectra due to a difference in lifetime. However, in the case of Rydberg-Ps, the lifetime will be much longer than for ground state o-Ps. As a consequence, the presence of Rydberg-Ps should be notable as an excess of o-Ps annihilations several hundred nanoseconds after the prompt peak in the lifetime spectrum. This is because the Ps* atoms travel at a certain velocity after being emitted from the converter sample and will annihilate against the surrounding vacuum chamber walls, typically after a few hundred nanoseconds. The timing of these excess annihilations therefore do not correspond to the lifetime of the excited positronium atoms, but rather the time it takes for them to reach the chamber walls.

2.7.3 Excited Positronium and Antihydrogen Production

Exciting positronium to a Rydberg state is essential for the planned antihydrogen production in AEGIS. In this planned production, a charge-exchange reaction between excited positronium and antiprotons ($\bar{p}$) will result in the formation of antihydrogen ($\bar{H}^*$) in a Rydberg state, as shown in Equation 2.16 [63].

$$Ps^* + \bar{p} \rightarrow \bar{H}^* + e^- \tag{2.16}$$

This reaction will be employed because of the large expected cross section of the antihydrogen formation ($\sigma \sim 10^{-8}\text{cm}^2$), where the cross section is proportional to the principal quantum number of the excited positronium atoms as n^4 [1]. Additionally, the resulting formation of excited $\bar{H}$ atoms plays a significant part in the AEGIS gravity measurement. The $\bar{H}^*$ atoms will have to be accelerated in order to form a beam, and for neutral atoms this can only be done efficiently for excited atoms with a large dipole moment, by a process called Stark acceleration. In light of this, the formation of large amounts of positronium and a subsequent efficient laser excitation become very important steps in the antihydrogen production and gravity measurement of AEGIS. More details on the schemes for antihydrogen production and the significance for the AEGIS experiment can be found in Appendix A.

Chapter 3

Experimental

This section discusses the set-up of the AEGIS experiment, the positron beam line and the laser system. Other parts of the positron system and positron experiments that are described in more detail are the positron-positronium converters, the diagnostic tools and the system operation.

3.1 The AEGIS Experiment

The AEGIS collaboration was started in 2006 as a continuation of the ATHENA collaboration at CERN. The main objective of the experiment is to directly measure the Earth's gravitational acceleration ($\bar{g}$) on antihydrogen with an accuracy of 1%. More precise measurements will become pertinent after the first results of this gravity measurement have been attained. AEGIS is currently in Stage 1 of its experimental life, where the main goal is to produce cold antihydrogen. The AEGIS experimental area is physically located at CERN, Geneva, in the AD-hall where the Antiproton Decelerator (AD) is located. All experiments at CERN related to antimatter studies are connected to the AD via magnetic transfer lines and receive antiprotons ($\bar{p}$) via this decelerator.

For the purpose of this work, it is practical to divide the AEGIS experimental apparatus into three sections. The first section is the main (antihydrogen) apparatus, which houses all the main parts that are needed for the production of antihydrogen and positronium.

The second section is the positron system, which can deliver a positron beam either to the main apparatus, or to a separate test chamber. The assembly of the positron system was started in 2011, and the test chamber was installed in the end of 2013. The system consists of a positron source, a complex for accumulating large amounts of positrons, and a region for transferring positrons and testing positronium formation.

The last section is the laser system, which can deliver laser pulses to both the main apparatus and the positron system. The positron and laser systems will be described in greater detail in the later sections of this chapter. The following will give a brief overview of the main apparatus and experiment, in order to provide an insight into the principle and goal of the gravity measurement.

3.1.1 The Antihydrogen Experiment

Measuring $\bar{g}$

An outline of the planned AEGIS antihydrogen production process is shown in Figure 3.1. The red box encloses the part of the process which is most relevant for this work, namely positron-positronium conversion and excitation of positronium. The steps required to produce an antihydrogen beam and measure its gravitational acceleration can be condensed down to [64]:

1. Capturing fast antiprotons being sent from the AD-ring and cooling them down to temperatures less than 1 K by electron-antiproton sympathetic interactions,

2. Accumulating large amounts of positrons from a decaying ^{22}Na source,

3. Producing positronium atoms by implanting positrons in a porous silica target, which acts as a positron-positronium converter,

4. Using lasers to excite Ps to Rydberg states (Ps*) via an excitation to $n = 3$,

5. Forming cold Rydberg $\bar{H}^*$ via charge-exchange reactions between antiprotons and Rydberg-Ps,

6. Accelerating the antihydrogen atoms via Stark acceleration, thereby forming the antihydrogen beam,

7. Measuring the vertical displacement of the $\bar{H}^*$ atoms due to gravitational acceleration with a Moiré deflectometer.

The gravity measurement itself will be done by accelerating the antihydrogen atoms and measuring the vertical displacement at the end of the beam line with a Moiré deflectometer [65]. This deflectometer will consist of two gratings placed after each other and a position-sensitive detector. These gratings will create an interference pattern which is purely kinematic, meaning that it is formed by the particle trajectories crossing the gratings, and that it is not a product of diffraction. This is possible because the two gratings

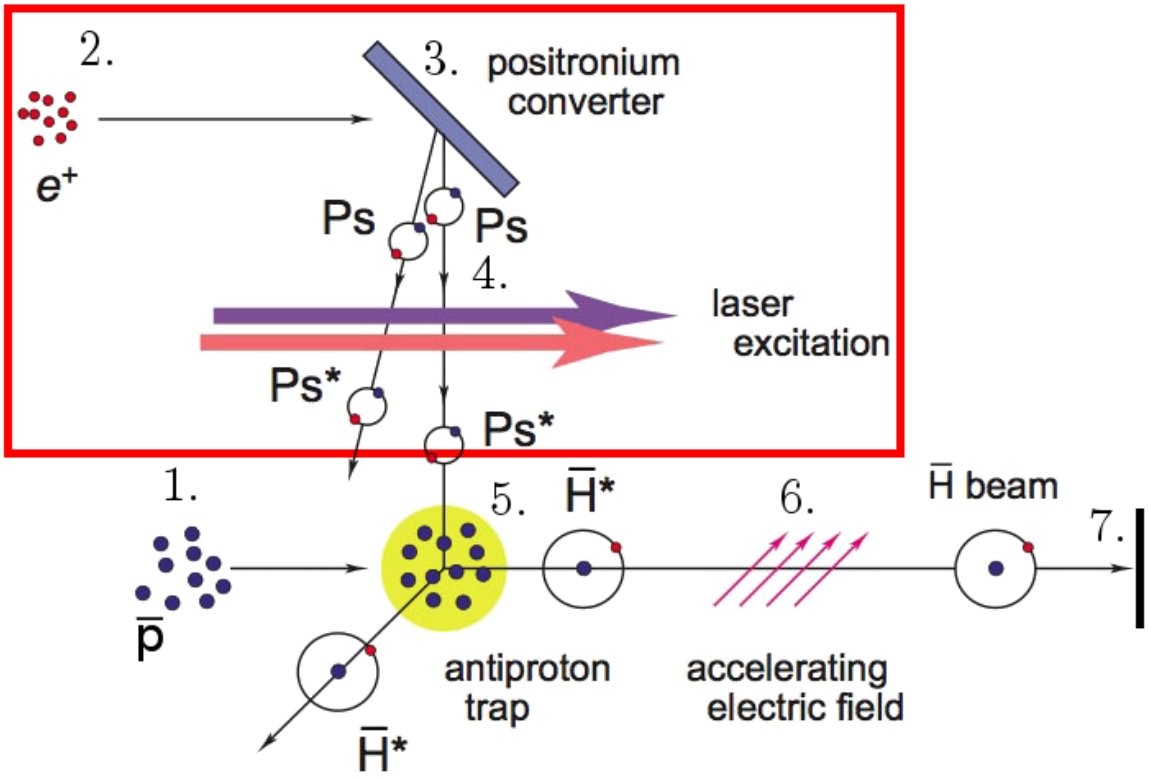

Figure 3.1: Schematic representation of the principle behind the AEGIS antihydrogen production and gravity measurement, after Kellerbauer *et al.* [64]. The numbers 1.-7. indicate the main steps of this experiment, as explained in the text. The red box highlights the production of positronium from positrons, as well as the laser excitation of positronium.

have periodical apertures whose diameters are larger than the de Broglie wavelength of the antihydrogen atoms. The position-sensitive detector (for instance a pixel detector) will then measure the shadow pattern of the atoms that make it through the two gratings. Numerical simulations performed in [64] have shown that about 10^5 atoms of antihydrogen at a temperature of 100 mK are needed to measure the gravitational acceleration to a precision of 1%.

The AEGIS Main Apparatus

A cross section of the main apparatus in AEGIS is shown in Figure 3.2. This apparatus is contained within one large cryostat and can be divided into two large areas, one which is within a 5 T magnet and one which is within a 1 T magnet. The apparatus receives positrons with an energy of 300 eV from the positron system and antiprotons with an energy of 5 MeV from the AD ring.

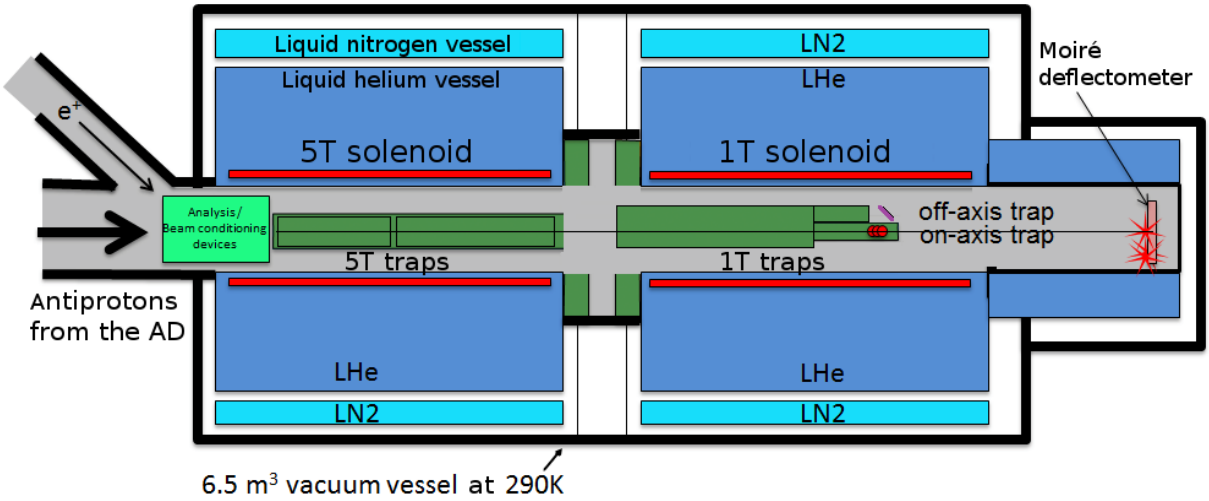

Figure 3.2: A simplified overview of the AEGIS main apparatus, where antihydrogen atoms will be produced and the antigravity measurement will be done. There are several detectors for the beam analysis just at the entrance of the the main apparatus (light green). The middle region of the apparatus is held at a high vacuum, and this is the beam line for antiprotons and positrons (in grey). Electrodes and strong magnetic fields are used to trap and control the particle clouds. Within the 5T magnet are traps for catching and accumulating antiprotons and in the area of the 1T magnet are the traps that enable positronium formation, antiproton trapping and antihydrogen formation (dark green). See the text for a further explanation of these traps. The Moiré deflectometer will soon be installed at the end of the beam line, used for detecting the vertical displacement of the antihydrogen beam. Superconducting magnets are installed in two sections around the beam line, giving the name for these two sections: a 5 T and a 1 T solenoid (red). These solenoids are cooled down to cryogenic temperatures in order to be superconducting, and are therefore installed inside a vessel containing liquid helium (4 K, dark blue). Between this vessel and the normal atmosphere is another vessel containing liquid nitrogen (77 K, light blue).

The main apparatus has a center which consists of several traps and a beam tube held at a high vacuum. The 5 T region contains two traps that are mainly used for catching and accumulating antiprotons sent from the AD ring. The 5 T catching trap is used to cool down the fast antiprotons as they enter the main apparatus, and this is done by letting the antiprotons lose energy to electrons via inelastic collisions. The 5 T accumulation trap is used to collect a large amount of antiprotons. The accumulation trap is necessary in order to create an antiproton cloud with a sufficient number and density to interact with the positronium cloud.

The 1 T region contains two sets of traps that are designed to separately treat positrons and antiprotons. The positrons that are sent down to the main apparatus are captured in the 5 T region, and will further be sent to the 1 T diochotron trap. This trap will move the positron cloud off-axis from the main beam axis of the trap. This off-axis positron

beam will then be sent to the positron launch trap, also referred to as the off-axis trap, where it is compressed both radially and longitudinally. This cloud will be accelerated towards the positron-positronium converter in the main apparatus, where positronium will be created and subsequently excited by laser pulses. Meanwhile, the antiprotons are sent from the 1 T region and captured by the antiproton stopping trap, which is used to compress the antiproton cloud. The antiprotons and excited positronium atoms are finally sent to the antihydrogen formation trap, where the two particle clouds will interact to form antihydrogen. A special Moiré deflectometer will be installed at the end of the beam line in the near future, in order to measure the vertical displacement of the antihydrogen atoms as they are transported.

The two large solenoids are superconducting, and have to be cooled down to 4 K during operation. Two tight vessels are installed around the solenoids, the first of which is filled with liquid helium (LHe) and the second of which is filled with liquid nitrogen (LN2). The LHe vessel ensures a temperature of 4 K in the experiment, and the LN2 (at 77 K) provides at buffer zone between the helium vessel and the ambient atmosphere.

3.2 The AEGIS Positron System

This section will describe the components of the positron system in more detail, as well as the operational principles of the different components. A scheme of the entire positron system can be found in Figure 3.3. Good vacuum conditions are ensured throughout the system by several roughing, cryogenic and ion pumps. The different parts of the system are separated by pneumatic valves when the system is off.

3.2.1 Positron Source

The source used in this experiment originally had an activity of 18 mCi when it was commissioned in 2011. As the half-life of ^{22}Na is 2.6 years, an activity of around 7 mCi (260 MBq) is expected during this work. The source assembly used here, including all of the coils, pumps and components except for the sodium itself, is provided by `First Point Scientific Inc.`, a company specialised in supplying commercially available positron systems.

A scheme of the positron source and source holder is shown in Figure 3.4. The sodium source is installed on a tantalum-coated titanium head, and is enclosed by walls made from titanium. Tantalum is a high-Z material and is used to reflect positrons, as it has a very high probability of positron back-scattering at 25%. The positrons that contribute

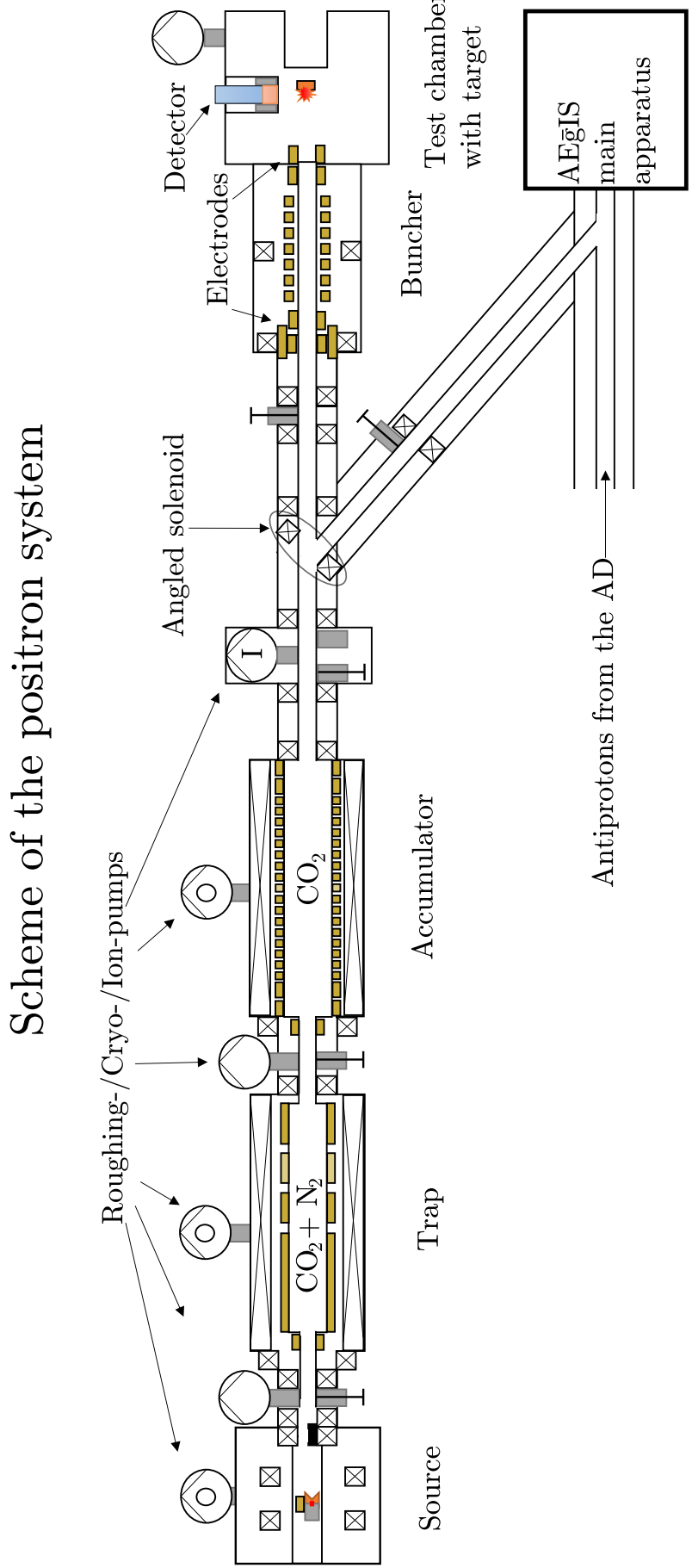

Figure 3.3: The AEGIS positron system, with all the main components (after [66]). The source is where the radioactive ^{22}Na is situated. The trap is the region with the initial trapping and cooling of positrons, while large amounts of positrons can be gathered and cooled in the accumulator. The positrons are dumped from the accumulator and into the transfer line, where the positron beam can be sent into the main apparatus or towards the buncher electrodes and test chamber.

to the beam are therefore those that are emitted towards the moderator, as well as some of those that are reflected by the tantalum.

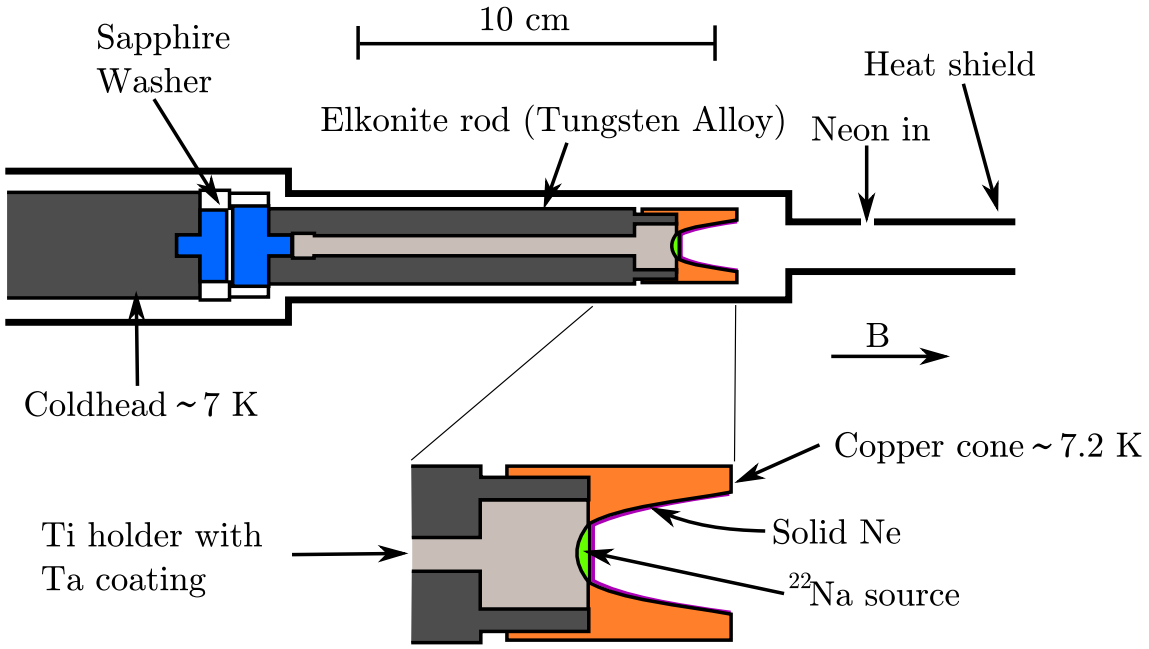

Figure 3.4: Positron source and source holder used at AEGIS. The ^{22}Na source is mounted on a titanium holder coated with tantalum, which is situated inside an elkonite rod. A sapphire washer divides the elkonite rod into two electrically isolated parts, and the rod can be cooled down to 7 K via a cold head [67].

The source holder itself is a rod made of elkonite, which is a tungsten-copper alloy. Elkonite has good thermal conductive properties, and is also a good shield for gamma radiation emitted from the source due to its high density. The elkonite rod is split into two parts that are kept electrically insulated through the use of a sapphire (Al_2O_3) disc. Sapphire has good thermal properties and bad electrical conductive properties, which means that a bias voltage can be applied over the source. A copper cone is mounted on the rod so that it surrounds the positron source. This conical geometry has earlier been established as the best structure for growing RGS moderators and obtaining efficient positron moderation [68].

Moderator

In this positron system solid neon is used as a positron moderator, and it is grown directly onto the source and copper cone. Neon solidifies at around 10 K at low pressures. The elkonite source holder is therefore cooled down to 7 K with a helium-pump refrigerator (this component is commonly referred to as the *cold head*), and the source chamber is kept in a high vacuum. This has the added benefit of minimising the amount of surface contaminants on the moderator. A potential of 18 V is set over the source, and

this is mainly used to accelerate the positrons towards the next section of the positron system. As mentioned earlier, neon moderators have a wide band gap, which means that positrons thermalise very slowly inside the material. Most positrons reaching the surface are therefore not thermalised, and can be emitted from the neon surface despite the positron work function being positive. The extra potential over the source will of course also accelerate a fraction of thermal positrons out from the moderator.

The moderator is re-grown every 4-5 days to ensure a high efficiency and good moderator characteristics. The growth of a new moderator is initiated by heating the source chamber to 25 K so that the old moderator is evaporated, and the old Ne gas is pumped out. The chamber is then cooled to 8.8 K, at which point new Ne gas is injected into the chamber, where the gas condensates and solidifies on the source surface. The solid neon layer is then annealed at 9.3 K, as the initial layer contains many defects. Lastly, the chamber is cooled down to 7 K, with the entire process taking around 45 minutes. The growth of the moderator is fully automated and controlled by the system computer.

The mean energy of the positrons emitted from the moderator is around 17 eV, and the moderator efficiency lies at $\epsilon \sim 2.5\times10^{-3}$ [66]. The efficiency of the moderator in this system degrades over time. The largest decrease in efficiency happens during the first few hours after a new moderator is made [5], as impurities are formed on the surface and the moderator relaxes to a stable state. After this, the moderator is relatively stable for several days. Because of these moderator characteristics, the positron system is usually not used until several hours after the moderator growth. This is to ensure a stable moderator behaviour and a constant number of positrons for measurements that go over several hours.

3.2.2 Trap

The first region that the positrons arrive at after the source is a Surko trap with a rotating wall, as described in Section 2.3. This Surko trap is used as an initial step for cooling down the positrons, and is just referred to as the 'trap'. The confining magnetic field in the trap is $B_{trap} = 0.07$ T. The cooling in this first trap has to be very efficient, as many of the incoming positrons have rather high energies. To achieve this, a large amount of buffer gas has to be introduced, which gives a relatively high pressure of up to 10^{-4} mbar inside the trap. The positron lifetime is concomitantly very low at a few hundred milliseconds.

The three phases of filling, storage and dumping the trap are shown in Figure 3.5. These phases are controlled by six electrodes (Mod, Inlet, 1, 2, 3 and Gate), where the magnitude of the potentials can be changed in the order of 100 μs. In the first phase, the

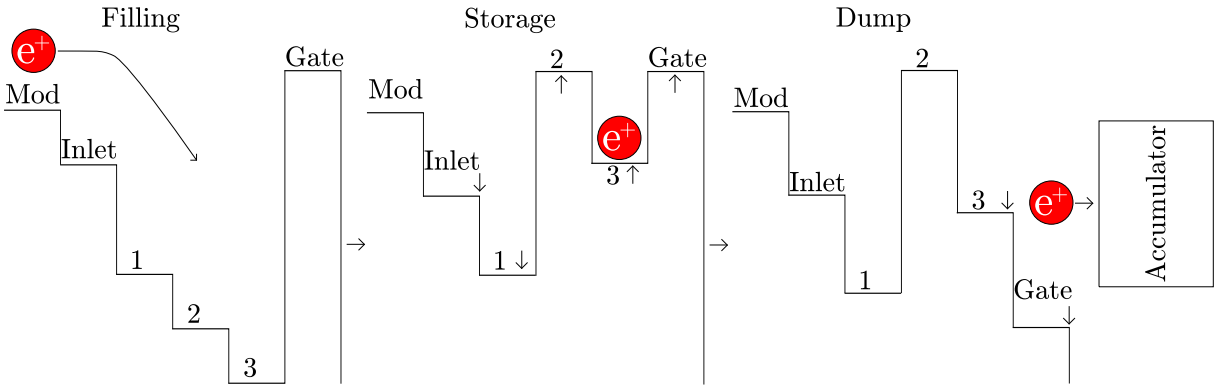

Figure 3.5: Illustration of the storage process in the trap [5]. The electrode potentials are modified in three steps. Positrons are admitted into the trap in the filling stage. Potentials are then raised in the storage step to trap positrons. The Gate potential is lowered in the last step, dumping the positrons into the accumulator.

Inlet electrode is kept at a low potential, and positrons can enter from the source. The positrons lose their energy to inelastic collisions against small amounts of CO_2 and N_2 gas that are pumped into the trap, and are reflected at the Gate electrode. A fraction of the reflected and cooled positrons do not have enough energy to overcome the potential of electrode 2, and become trapped in the region of electrode 3. In the storage stage the potentials of electrode 2 and 3 are raised, trapping the positrons. In the end the potential of the Gate electrode is lowered as fast as possible, dumping the positron bunch into the accumulator trap. This entire process takes 0.15 s, where each positron bunch is referred to as a 'pulse'.

3.2.3 Accumulator

Following the Surko trap, there is a second trapping region which consists of a Penning-Malmberg trap with a rotating wall, which employs a small amount of buffer gas. This second trap is called the 'accumulator', and has a confining magnetic field of $B_{acc} = 0.1$ T. The accumulator is distinguished from the Surko trap by its function, as it can accumulate a large number of positrons that are already cooled. The construction and processes in the accumulator are otherwise very similar to that of the trap, but there are some differences that change the function substantially. Only CO_2 is used as a buffer gas in the accumulator, and the pressure is held at $6{\cdot}10^{-8}$ mbar. As a consequence, the positron lifetime is on the scale of minutes rather than hundreds of milliseconds. The lifetime and compression of the positron plasma inside the accumulator is further improved by the application of a rotating wall, which is switched on during the entire accumulation process. This rotating wall has not been found to be in the strong-drive regime [5], but still enhances the plasma characteristics.

Additionally, the electrodes in the accumulator form a harmonic potential well rather than a stepped potential, which is realised by 21 electrodes. The harmonic potential well is illustrated in Figure 3.6. The electrodes are designed so that only the two boundary electrodes (Ec1 and Ec2) and the central electrode (Ring) are connected directly to power supplies. All the other electrodes are connected to the boundary potentials with resistors so that the harmonic shape is formed. The shape of the potential well leads to an efficient cooling of the positrons. Moreover, the size of the positron plasma in the longitudinal direction decreases as the positrons cool down, which means that the plasma shrinks somewhat as it is stored.

Another difference between the accumulator and trap is that the filling can be done several times by lowering and increasing the inlet electrode. Positron pulses can be admitted at the same rate as the dumping rate of the trap, so that a new pulse is added every 0.15 s. The accumulator can thereby gather several hundred pulses from the trap, which forms a positron plasma with a large number of positrons. When the desired number of pulses is reached, a signal is sent to dump the positron plasma from the accumulator and into the transfer line. The harmonic potential in the accumulator is then raised to a linear falling slope so that the plasma is accelerated out from the accumulator (see Fig. 3.6). The magnitude of this potential is adjustable, and the positrons can be dumped with an energy between 50 eV and 400 eV. An energy of 100 eV is used for transfer to the test chamber.

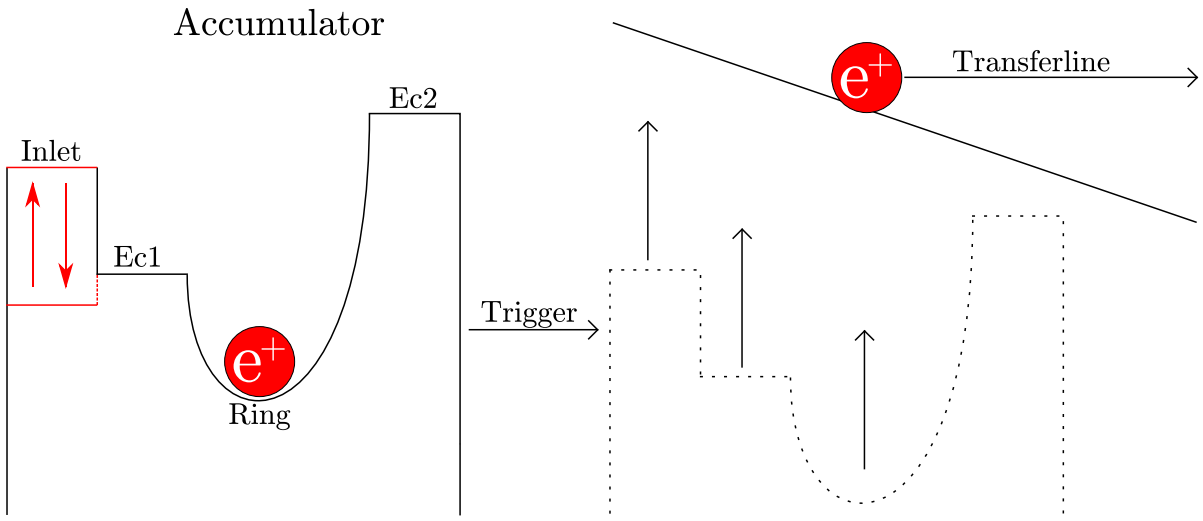

Figure 3.6: Illustration of the storage process in the accumulator [5]. The potential on the Inlet electrode is lowered for every pulse coming from the trap. The Ring electrode, together with the two endcap electrodes (Ec1 and Ec2), define the harmonic well. Positron pulses are accumulated in the harmonic potential until a trigger arrives. The positron plasma is then dumped into the transfer line, by changing the harmonic well into a linear potential.

When doing experiments in the positron system, 1000 pulses are typically stored in the accumulator before dumping the positron plasma into the transfer line. With this number of pulses, the expected number of positrons in the plasma lies around 3×10^7, which is in agreement with measurements done with calibrated detectors [5]. Accumulating 1000 pulses takes 150 s, so the positron plasma can be dumped approximately every 2.5 minutes. In these earlier measurements it was also found that the lifetime of the positrons inside the accumulator is around 450 s, which means that the number of positrons in the plasma can be maximised by storing for almost 8 minutes. However, accumulating for 8 minutes leads to a longitudinal expansion of the plasma, and results in very time-consuming measurements. For these reasons, the positron beam is usually comprised of 1000 pulses.

3.2.4 Transfer Line

The transfer line facilitates the transport between the accumulator and the positron test chamber or alternatively to the main region of the experiment, as illustrated in Figure 3.3. The positrons move together as one bunch in the transfer line after being dumped from the accumulator, with a temporal spread of ∼20 ns.

Positrons dumped from the accumulator are transported magnetically for a length of ∼60 cm, when they are transferred to the test chamber. The radial confinement in this first part of the transport is controlled by 6 main solenoids around the transfer line, in addition to some smaller correction coils. There is no longitudinal confinement, as the transport is dynamic and ends with the positron implantation in the test chamber. The positron beam can be steered into either the test chamber or the main region using a remote-controlled beam switch. This switch is in practice managed by the angled solenoid, indicated above in Figure 3.3. If this solenoid carries the current, the positron beam is directed towards the main apparatus. When the angled solenoid is not switched on, the positron beam is steered towards the region with electrostatic transport.

After the magnetic transport, the positrons are injected in a region with a series of 28 electrodes [69], as shown in Figure 3.7. Terminating the magnetic field a distance away from the test chamber is necessary because some positronium experiments can only be performed in the absence of magnetic fields. Moreover, some of the diagnostic tools in the test chamber are sensitive to magnetic fields. The electrostatic transport also serves to focus the positron beam on the target region with a small spot size, in addition to accelerating the positrons in order to implant them with an energy up to several keV. The first electrode is made of μ-metal, which is a nickel-iron magnetic alloy with a high permeability, and is often used to shield against magnetic fields. The μ-metal electrode

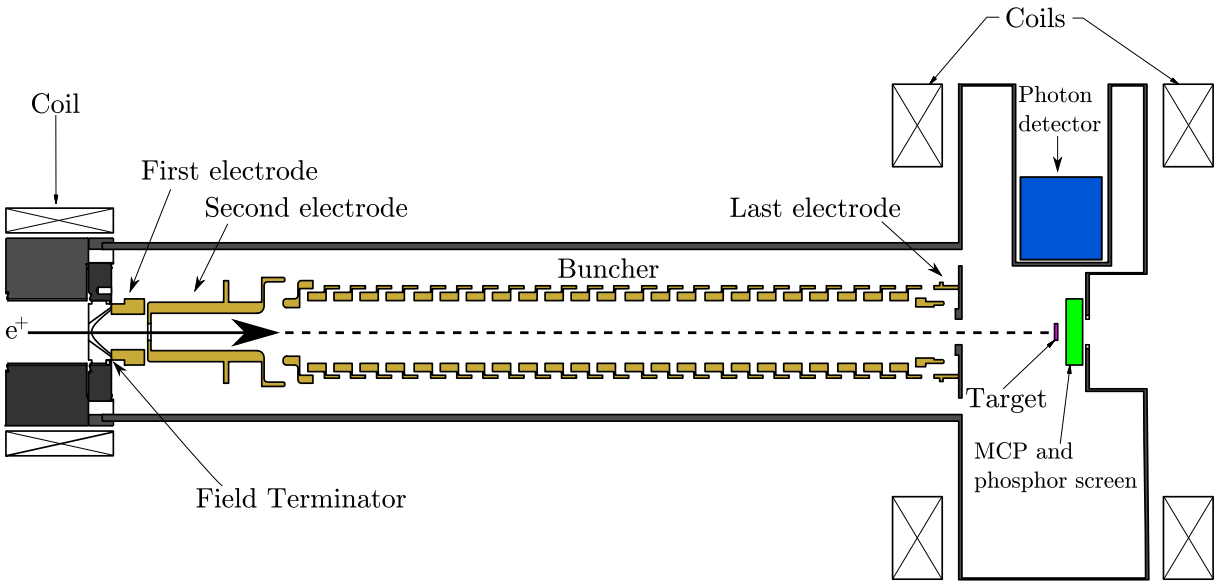

Figure 3.7: Outline of the last part of the transfer line, with the positron test chamber on the right. This part of the transport is facilitated by several electrodes, where the series of 25 buncher electrodes can be used to accelerate the positron cloud. The positrons are implanted in the target region, where a closely placed photon detector can be used to observe the positron annihilation. The MCP assembly can be used to investigate the geometry of the positron cloud, and is explained further below.

therefore works as a magnetic field terminator, reducing the magnetic field from 85 G to 2 G in less than 1 cm. This electrode is held at −800 V and is connected to a second electrode held at −2100 V. The next 25 electrodes are all initially held at −535 V, and together these comprise the buncher, which will be described in more detail below. The last lens is held at −3000 V and is placed downstream of the buncher electrodes. This is the main electrode for focusing the beam on the target region, although all the electrodes must have the correct voltage in order to keep the beam from diverging during transport. Some complications arise when switching from magnetic to electrostatic transport, usually resulting in a larger angular divergence of the beam and subsequent loss of a fraction of the positrons at the first electrodes. This is an intrinsic effect of switching the transport method, and a more detailed description can be found by Canter [70].

Buncher

The buncher consists of 25 electrodes at 1.6 cm each, resulting in a total length of 40 cm. This is much longer than the extent of the positron cloud, which is estimated to be ∼12 cm. A length of 12 cm corresponds to a positron energy of 100 eV and a temporal spread of ∼20 ns, which assumes that the temporal spread is constant through the transfer line. The buncher is mainly responsible for compressing and accelerating the positron cloud, whereas

the focusing in the target region is facilitated by all the electrodes working in unison along the transfer line. Similar techniques with buncher electrodes have been implemented in other positron systems [71], resulting in a considerable temporal compression of the positron beam.

As stated above, the buncher electrodes are initially held at a potential of −535 V. When the positrons enter the region of these electrodes, a potential with a parabolic shape is set between the first and the last electrode. This potential compresses the positron bunch by accelerating the last positrons in the cloud more than those that are close to the test chamber. The result is a positron cloud with a much smaller temporal spread, and a much higher velocity. The parabolic potential is superimposed on a high-voltage potential, which serves to accelerate the entire positron cloud, as shown in Figure 3.8.

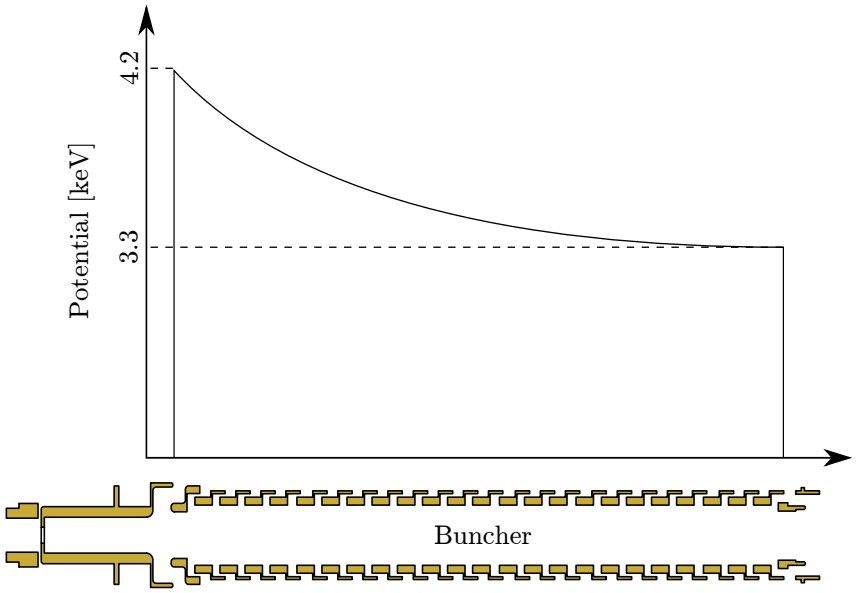

Figure 3.8: Example of the high bias voltage and parabolic potential in the buncher as it is switched on. The potential values in this plot are the same that are used during the experiments presented later.

The bias voltage and the parabolic potential in the buncher is generated by a high-voltage (HV) pulser (`FID GmbH technology`, model `FPG 10-003NM30`) with a range of 3-10 kV. The pulse duration is 30 ns and the rise time is 2-3 ns. The synchronisation of the pulsed potential of the buncher with the positron cloud dumped from the accumulator is ensured with a digital delay generator (`Stanford Research Systems DG645`). The functionality of the buncher electrodes was planned from the commissioning of the positron system, but the HV pulser only became available during this work. The last part of the transfer line has therefore only used the base voltage of −535 V when transporting positrons, up until the point of this study. The implementation and synchronisation of the high voltage potential in the buncher will be presented below.

3.2.5 Test Chamber

The test chamber is the end point of the positron apparatus, and is used for positronium production and other experiments involving positrons. The layout of the test chamber is shown in Figure 3.7.

The chamber contains a sample holder which is connected to an actuator installed at one of the flanges perpendicular to the beam line. The sample holder is elongated, and up to three different samples can be installed at any one time. The actuator can be used to move the sample holder, and in this way several samples can be investigated sequentially without opening the chamber. The positron beam can also be implanted into the sample holder itself, which is made from aluminium. Additionally, the holder can be moved completely out of the beam line using the actuator. When the holder is removed, the positrons annihilate on the MCP assembly where no positronium is formed. The MCP assembly is a diagnostic tool which is described in Section 3.5.3. A viewport is installed in the chamber behind the MCP assembly, and is used for a dedicated imaging camera. Another flange on the top of the chamber has an indent, which is used for housing a photon detector during positron measurements. Another viewport is installed on the side of the test chamber opposite of the sample holder actuator. This viewport allows for the admittance of laser radiation for the positronium excitation experiments.

Two magnetic coils are installed around the test chamber, which can generate a field parallel to the beam. By using these solenoids, the magnetic field in the test chamber is tunable from less than 2 Gauss up to 300 Gauss, which allows one to perform spectroscopic experiments that require different environmental conditions [72, 73].

3.3 The AEGIS Laser System

The AEGIS laser system system employs a Q-switched Nd:YAG laser as a source for laser radiation, and the Q-switched laser itself is a custom-made IR pumped laser assembly manufactured by `EKSPLA`. The laser assembly provides separate pulses at three different wavelengths: 1064 nm, 532 nm and 266 nm. These wavelengths correspond to the first, second and fourth harmonic of the Nd:YAG laser radiation. The second and fourth harmonics are created by non-linear KTP crystals ($KTiOPO_4$). The UV and IR wavelengths required by the AEGIS experiment are produced in two separate and independent parts of the system. A layout of the laser is shown in Figure 3.9. A more in-depth description of this system can be found in [62, 74].

As mentioned earlier, a wavelength of about 205 nm is required to excite positronium from ground state to $n = 3$. The UV laser pulse is produced in the following way.

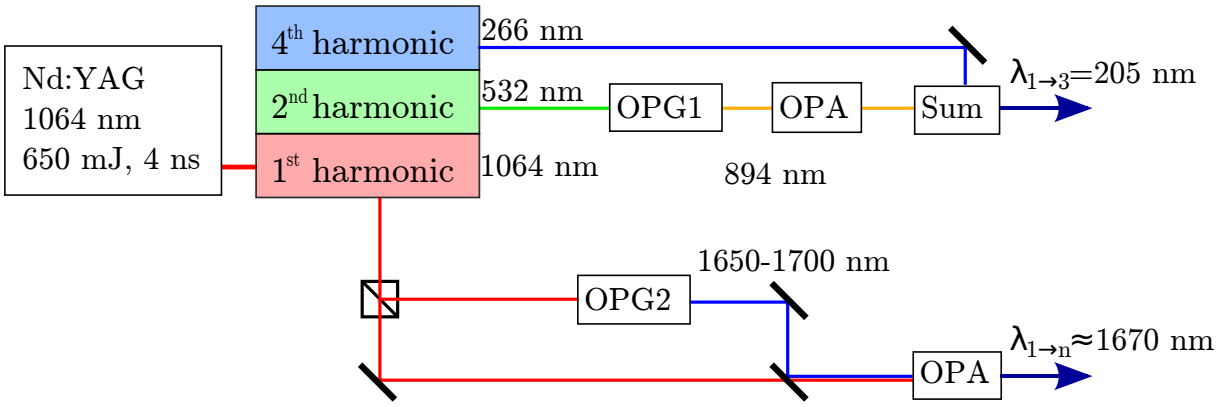

Figure 3.9: Laser system used to excite positronium to a Rydberg state via the $n = 3$ state. The UV laser pulse is constructed from the Nd:YAG laser by summing the 266 nm fourth harmonic and the 894 nm radiation generated in an OPG and amplified in and OPA. The IR laser pulse for excitation to a Rydberg state is constructed from the first harmonic via an OPG and OPA. Image after Caravita [62].

Radiation at 894 nm is generated in an OPG (Optical Parametric Generator), which is pumped by the 532 nm second harmonic of the Nd:YAG. This radiation is also amplified by an OPA (Optical Parametric Amplifier). The 894 nm radiation is then frequency summed with the 266 nm fourth harmonic of the Nd:YAG in a non-linear barium borate (BBO) crystal. The wavelength of the laser can be tuned between 204 nm and 206 nm. In the current configuration, the generated UV laser pulse has a time length of 1.5 ns, with a bandwidth of about 112 GHz and a energy tunable up to 60 μJ. The spatial shape of the laser pulse is somewhat elliptical, with a vertical FWHM of 6 mm and a horizontal FWHM of 4 mm.

The second laser pulse excites the positronium from $n = 3$ to a Rydberg state, and the wavelength of this pulse is ∼1670 nm depending on which Rydberg level is required. This IR wavelength is constructed in two stages. The required wavelength is initially created from the first harmonic generation within an OPG crystal, and then the pulse is amplified by two OPA crystals. Subsequently, a dichroic mirror is used as a filter for the 1064 nm radiation, as it is unsuitable for the Rydberg excitation, leaving only the amplified radiation.

Additionally, the 1064 nm radiation from the Nd:YAG can be used directly for the photoionisation of positronium excited to the $n = 3$ state. As mentioned, this can be done in order to more easily observe the excitation of Ps atoms. The time length of this laser pulse is 4 ns, and an energy up to 55 mJ can be used. This laser pulse has a circular spatial shape, with a diameter of 8 mm. The 1064 nm radiation and the UV radiation have been used during this work.

After the required laser pulses are produced, a transfer line transports the laser pulses

from the laser system to the experimental area. For transport to the main apparatus, the two laser pulses follow different paths. For transport to the test chamber in the positron system, the two laser pulses are superimposed in time and space, and transported by the same optical system. The laser pulses are aligned in the target region of the test chamber by monitoring, with a CCD camera, their position on a 1 inch `Macor` ceramic screen. This screen is placed inside the vacuum chamber a few centimetres away from the target. A synchronisation between the laser pulse and the positron beam is obtained with a custom-built FPGA-based synchronisation device, with a time resolution of 2 ns.

3.4 Positron-Positronium Converters

During this work, several samples were tested and compared as positron-positronium converters. All of these samples were made from monocrystalline silicon materials with different characteristics. The following will describe these samples and the production method, together with the positronium formation process and the earlier research into these materials.

3.4.1 Samples and Production Method

The positron-positronium converters used in this study are samples with an array of etched nanochannels connected to the surface. Nanochannels into the bulk of the material are made in the samples by electrochemical etching with hydrofluoric (HF) acid. The etching process is done by lowering the samples into a 75 ml solution consisting of 47 ml of HF (48%) and 28 ml of ethanol. Two electrodes are in contact with the solution, with an etching current in the order of milliamperes and an etching time of 15 min. The samples are subsequently heated to 100°C in order to induce oxidation, which creates a thin layer of silica on the internal surface of the nanochannels.

Four samples in total were used in this study, from three types of silicon: p-type with a (100) crystal orientation, p-type with a (111) crystal orientation and n-type with a (100) crystal orientation. One sample of each silicon type was etched at 10 mA for 15 minutes, and an extra n-type (100) sample was etched at 20 mA for 15 minutes. An overview of the produced samples is given in Table 3.1. The p-type (100) sample was produced early in 2014 for initial testing in the positron system, while the other three samples were made during this work.

The etching and oxidation processes can be repeated several times to increase the diameter of these channels [54]. The initial etching process at 10 mA and subsequent oxidation results in nanochannels with a diameter of approximately 5-8 nm with a depth

Table 3.1: Silicon samples that were tested as positron-positronium converters in this work, detailing the silicon type, etch process and annealing step.

Silicon type	Etch process	Resistivity
p-type (100)	15 min at 10 mA	0.15-0.21 ohm-cm
p-type (111)	15 min at 10 mA	0.15-0.21 ohm-cm
n-type (100)	15 min at 10 mA	0.1-1.0 ohm-cm
n-type (100)	15 min at 20 mA	0.1-1.0 ohm-cm

of 1-2 μm in p-type silicon with a (100) crystal direction. As the p-type (111) sample has the same resistivity as the p-type (100), the channel formation will likely be at the same rate in these two samples. The resistivity of the available n-type silicon is less well-defined than the p-type silicon, and as such the etching rate of the HF solution is not known. The etched nanochannels can be imaged with a scanning electron microscope (SEM), and an earlier image of the p-type (100) sample can be seen in Figure 3.10a.

3.4.2 Positronium Formation

Figure 3.10b illustrates the positronium formation in these samples. The incoming positrons are slowed down in the silicon and then diffuse in the material. As the channels are closely spaced, the positrons are likely to reach the interface between silicon and silica within their lifetime, where it is energetically favourable for the positrons to enter the silica. Positronium is formed in the bulk of the silica, and then diffuses to the surface of the nanochannels. Ps atoms emitted into the nanochannels have a kinetic energy of 1-3 eV. Most of the Ps formed in these samples is therefore from the bulk of the silica, but a small contribution is also made by surface formation of Ps on the internal surface of the channels.

Ps atoms inside the nanochannels will collide with the walls, and experience loss of kinetic energy by inelastic collisions. The implantation depth of the positrons scale with their kinetic energy. The formed Ps atoms will therefore experience more collisions with the nanochannel walls as they travel towards the material surface and will have a lower mean velocity when emitted into the vacuum, if the implanted positrons have a high kinetic energy. So achieving thermal Ps atoms in these samples is dependent on implanting the positrons deep enough.

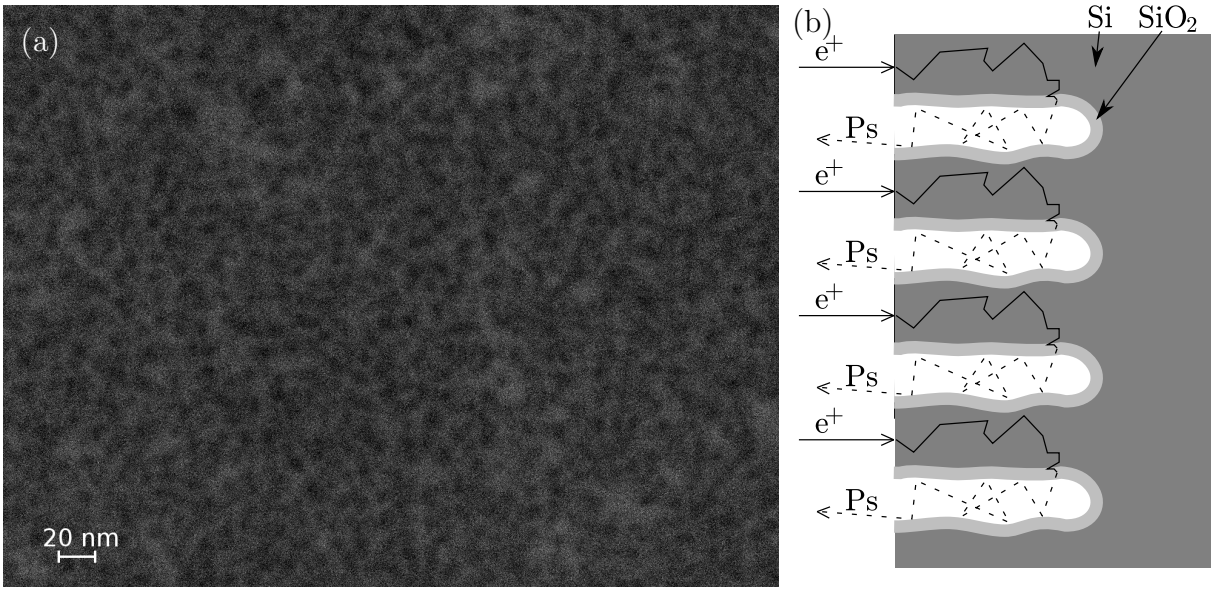

Figure 3.10: a) Example of the surface of the p-type (100) sample with nanochannels formed as described in the text. This sample was imaged at the university in Trento, image courtesy of Sebastiano Mariazzi. b) Principle of a positron-positronium converter consisting of silicon with nanochannels, where the surface of the channels has been oxidised to SiO_2.

3.4.3 Previous Research

Using etched and oxidised silicon as a positron-positronium converter offers several advantages compared to other silica materials with disordered pores, such as aerogel. The etching process can be adjusted in order to change the pore size, and the process itself results in an ordered and reproducible structure. The fabrication process used for these samples is also very simple. p-type silicon with a (100) crystal direction has earlier been investigated thoroughly as a positron-positronium converter, see for example [75,76]. This material forms positronium for a wide range of channel dimensions, where the channels are perpendicular to the surface, with a measured efficiency up to 40% for a channel diameter of 5-8 nm. The efficiency of positronium formation depends on the positron implantation energy into the target and the channel diameter. p-type silicon with a (111) crystal direction has been less investigated in previous work, and never with the same systematic investigation of positronium formation. As the nanochannels in p-type (100) silicon form along the $\langle 100 \rangle$ crystal direction and perpendicular to the surface, it is expected that the nanochannels in p-type (111) silicon are formed at an angle to the surface [77]. This is because etched nanochannels in p-type Si are preferentially formed along the $\langle 100 \rangle$ crystal direction. Channels formed in p-type (111) Si therefore likely have a higher degree of interconnectivity than the perpendicular channels in p-type (100) Si. n-type silicon has not been used extensively for positronium formation, and the channel structure and

positronium formation is therefore less known.

3.5 Diagnostic Tools

Several detectors are used in the positron system to trace particle trajectories and measure the properties of the positron plasma. Different photon detectors and photomultiplier tubes are investigated during this work, and an MCP assembly is used to characterise the spatial dimensions of the positron beam. The different detector types are described below [78], together with an overview of the specific detectors that are used in the positron system.

3.5.1 Plastic and Crystal Scintillators

Conventional detectors for high-energy photons usually consist of two parts: a photon converter and the actual detector. The photon converter transforms high-energy photons such as annihilation gamma rays to one or more low-energy photons. Converters are made of materials that display scintillation [10]. The electrons in the scintillator material are excited when struck by high-energy photons, and subsequently re-emit this energy in the form of visible light (low-energy photons). Depending on the material, this process can take from a few nanoseconds to tens of nanoseconds. Scintillating converters are typically either made from an inorganic crystal or organic plastic. Inorganic crystals generally have a very high quantum efficiency, so that almost every incoming photon results in many emitted low-energy photons. A disadvantage of crystals is that they exhibit a slower re-emission time. When organic scintillating materials are used, they are typically dissolved in a solvent and polymerised, forming a plastic. These plastic scintillators have a relatively low material density, which means that many gamma rays go through the detector without causing scintillation, resulting in a proportionately low efficiency. In addition, some plastic scintillators show a very delayed fluorescence, which can result in an after-glow on the acquired signal. However, these scintillators have a good temporal resolution and fast decay rate, which is advantageous for many measurements. These converters will generally accept any incoming photons with enough energy, including stray photons and cosmic radiation, and this makes proper shielding and small distances to the target important to reduce the noise. The second component in the detector assembly is either a photodiode or a photomultiplier tube.

In silicon photodiodes, the injected photons create a small current in the p-n junction due to the internal photoelectric effect. This current increases as more photons hit the photodiode. The flow of this current is restricted by using a resistor and a capacitor,

which generates a slowly decreasing (in the order of ms) voltage signal. Due to this, even an annihilation signal with a very small temporal spread will result in a signal that decreases over several milliseconds. Hence, the most valuable information from this type of detector is the peak voltage, which will be proportional to the total number incoming photons within a short time range. The large advantage of photodiodes is that they are not affected by magnetic fields. The positron system employs several CsI converters coupled to photodiodes that are installed external to the experimental apparatus. The CsI converters themselves are crystal scintillators. These detectors can be moved around due to their small size, and are used mainly to monitor the annihilation along the transfer line. These CsI detectors have been calibrated, and can for instance be used to estimate the amount of positrons annihilating in the test chamber or the transfer line [5, 66].

Photo-multiplier tubes (PMTs) utilize the photoelectric effect to transform an incident photon to an electron in a metallic photocathode at the entrance of the PMT. The PMT is connected to a high-voltage supply, and the electron is accelerated towards the first of several dynodes. When the dynode is hit by the electron, several secondary electrons are emitted, and these are further accelerated towards the next dynode. This creates an avalanche of electrons, and the signal is amplified. It takes the electrons a finite time to pass the dynode structure, sometimes tens of nanoseconds. As the secondary electrons are emitted with a small temporal spread, the amplified signal often has a pulse width of a few ns. PMTs produce a voltage signal, which is correlated to the energy and number of photons.

In this system, a scintillator attached to a PMT is installed in a cylindrical indent in the test chamber, so that the detector is 4 cm from the target holder (see Figure 3.7 for placement). This detector assembly is used to detect the positron annihilation in the test chamber and to create an accurate lifetime spectrum by SSPALS, which can be used to detect positronium formation. Two different PMT models from `Hamamatsu` have been used during this work: `H3378` and `R11265-100`. Several photon converters are also available, most notably a Pilot U plastic scintillator and a crystal scintillator made from $PbWO_4$. The plastic scintillator has a height of 38 mm and a diameter of 25 mm. The $PbWO_4$ crystal has a height of 20 mm and a square base with sides of 25 mm. A PbF_2 Cherenkov radiator was also used during this work, and its working principle will be described below.

3.5.2 Cherenkov Radiators

Cherenkov radiators are detectors that work with a principle which is quite different from scintillation [79]. When charged particles move through a medium with a velocity higher

than the phase velocity of light in that medium ($v_p > c/n$), the particles will emit light as they are slowing down. This is called Cherenkov light. The annihilation gamma rays that hit a Cherenkov crystal will ionise electrons, which then travel at a high velocity through the medium. These electrons will slow down by emitting Cherenkov light if their velocity is high enough. Cherenkov light can be amplified with a photomultiplier in the same way as light from plastic and crystal scintillators, so that an otherwise similar detector design can be used for these very different converters. The advantage of these detectors is an improved signal-to-noise ratio for positron detection, as only the high-energy annihilation photons are accepted. In addition, they have a very good temporal resolution, as Cherenkov light is emitted instantaneously. However, Cherenkov crystals have a much lower quantum efficiency as compared to scintillating materials, as only a few photons are emitted for each annihilation gamma ray. Moreover, low-energy gamma rays will create no Cherenkov light at all, so that the total detected signal from the 3γ-annihilation of o-Ps will be significantly lower.

The Cherenkov detector available for this system is made from PbF_2, and can be used together with the same PMTs as the scintillators. This PbF_2 detector has a diameter of 20 mm and a length of 60 mm.

3.5.3 MCP and Phosphor Screen

A multi-channel plate (MCP) coupled with a phosphor screen can be used to characterise a positron beam, specifically the geometry and relative intensity of a positron bunch impacting upon the MCP. The operational principle of the MCP is similar to that of the PMT, as it also uses the emission of secondary electrons for amplification. MCPs consist of continuously angled channels called *channeltrons* that are a few µm in diameter [80]. As these channeltrons are very small, several must be placed side by side in order to form an MCP. Channeltrons are made from a high-resistivity material that emits secondary electrons when hit by energetic photons or charged particles, such as positrons. A high voltage is typically applied over them, so that the secondary electrons are accelerated towards one end of the channel. Because of the angled distribution, the secondary electrons will hit the inside of the channels a bit further down, so that more secondary electrons are emitted, which can amplify the signal by several orders of magnitude. The signal can be further amplified by placing two or three MCPs in a series with the channels rotated at an angle to each other. The positron beam in this system can be implanted in the MCP, and the positron signal is then amplified by the emission of secondary electrons. The electrons generated by the MCP are accelerated towards the phosphor screen, which is excited by the incoming particles. The light emitted from the phosphor screen can then

easily be imaged by a CCD camera.

The positron system has one MCP and phosphor screen installed at the very end of the test chamber (see Figure 3.7), with the downstream side of the phosphor screen pointing towards a viewport. This MCP assembly was installed during this work, and was used to image the positron beam. The phosphor screen is thin, and light is emitted from both sides. The phosphor screen can be imaged by a camera (`Hamamatsu ORCA-R2` digital CCD camera, model `C10600-10B`) installed outside the test chamber. In this way the positron plasma can easily be imaged when the sample holder is completely retracted.

3.6 Operation and Data Processing

The positron system can be run either directly from the AEGIS experimental zone, or remotely from an outside control room. The entire system is controlled by `LabVIEW Virtual Instruments` (*vi*'s), version 2009. One *vi* is used mainly to control the timing of the positron dump from the accumulator. It is also possible to read out the signals from the CsI detectors instantly, which gives an overview of positron annihilation along the transfer line. In the current program version, one can choose between transferring to the antihydrogen apparatus or the test chamber, where the appropriate settings are chosen automatically for equipment such as electrodes and magnetic coils. A second *vi* oversees all the temperatures and pressures, as well as the pump status and the radiation monitors in the system in real-time. In this way, the system user can be alerted if any of these values are outside of the normal range.

Although different PMTs and photon converters can be employed in this system when acquiring SSPALS spectra, the data treatment following the data collection is always the same. The anode signal sent from the PMT is divided using a 50 Ohm `Mini-Circuits ZFRSC-2050B+` splitter and is then sent into two channels of a `Tektronix TDS5054B` 500 MHz bandwidth oscilloscope with a resistance of 50 ohm. One channel, with a gain of 1 V/div (vertical scale), is used to acquire the prompt peak, which is the initial high-intensity signal of positron annihilation. The other channel, with a gain of 100 mV/div, is used to record the low level part of the signal following the prompt peak in order to have a low digitisation noise [58]. Furthermore, the high-frequency noise of the low gain channel is reduced by using a low-pass filter with a cut-off frequency of 100 MHz. The two channels on the oscilloscope are then recorded by a computer and automatically merged to give the SSPALS spectrum.

Chapter 4

Results

4.1 Implementation of the Buncher

4.1.1 Positron Compression and Buncher Synchronisation

Measurements were done in order to synchronise the pulsed potential of the buncher with the positron beam from the accumulator. A fast photon detector with a PbF_2 crystal connected to a `Hamamatsu R11265-100` PMT was placed 4 cm from the target in order to detect the gamma rays generated by the annihilation of the transported positrons. The tests described below were performed with a parabolic amplitude of 900 V and a bias voltage of 3300 V, corresponding to a maximum voltage pulse of 4200 V when the buncher electrodes were switched on. An Al target was used as an implantation target when testing synchronisation and positron beam compression. 1000 pulses from the trap were stored in the accumulator before dumping the positron beam into the transfer line.

Figure 4.1a shows the maximum signal amplitude of the PbF_2 + PMT detector as a function of the time delay between the positrons being dumped from the accumulator and the buncher being switched on. Note that the time delay reported on the x-axis the figure is not the transport time of the positron cloud between the accumulator to the region with electrostatic transport. Rather, the time delay takes into account the intrinsic trigger delays introduced into the system by the pulser and the electronics of the accumulator, as well as delay in cables.

The synchronisation of the buncher electrodes is very important for the positron transport, as the positron cloud has to be in the region of these electrodes to actually be compressed and accelerated. When the potential in the buncher is activated too early (delay <15 ns), the positrons will be reflected at the entrance of the buncher and will therefore be prevented from reaching the target. Consequently, the signal amplitude on the detector will be 0 mV. However, if the buncher is activated too late (delay >60 ns),

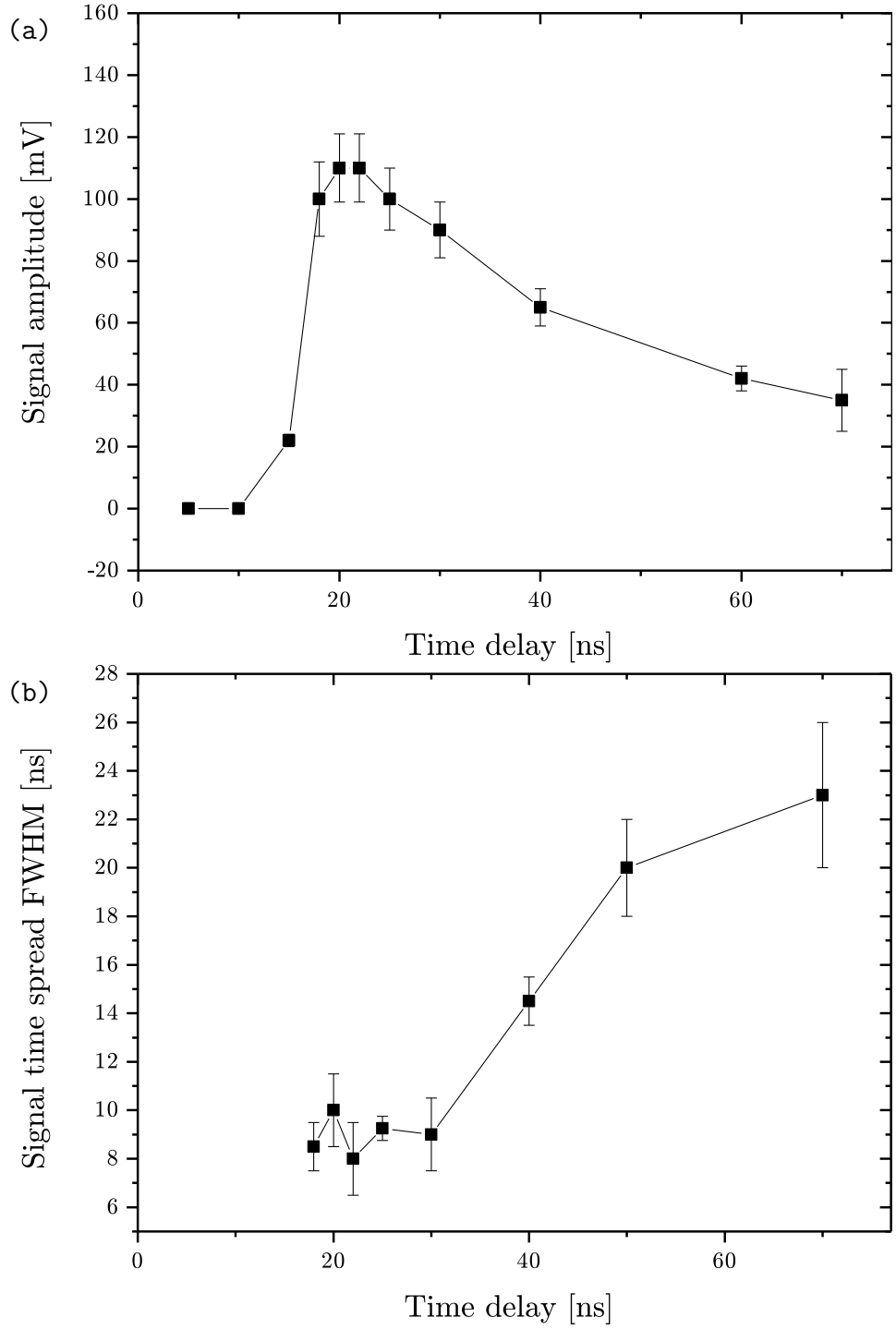

Figure 4.1: a) Maximum signal amplitude in the test chamber as a function of the buncher time delay, where the positrons annihilate on an Al target. a) Temporal FWHM of the signal in a) plotted against the time delay. Each data point is an average of 5 measurements, and the error bars are the standard deviations of the measurements. Where they are not visible, the error bars are within the points. Full positron compression takes place for a time delay between 18 and 25 ns, and this is also the time delay that results in the most efficient transport and highest signal amplitude. See the text for further explanation.

the positron cloud will mostly or completely have passed the electrode region, and will be unaffected by the parabolic potential. The resulting signal amplitude in the test chamber is around 40 mV. With a delay of about 20 ns, the signal amplitude is almost three times higher and reaches a value of 110 mV.

Another way to test the buncher is to measure the temporal spread of the positron annihilation signal as a function of the time delay. This measurement is shown in Figure 4.1b, where the full width at half maximum (FWHM) of the annihilation signal is plotted against the time delay of the buncher. Time delays below 15 ns are not relevant here, as those positrons never reach the target. For time delays longer than 25 ns, the FWHM is between 15-23 ns, which indicates that the positrons are not, or just partially, compressed. When the time delay is decreased from this, the FWHM becomes smaller and between 18-25 ns of delay it is approximately 7-9 ns. A comparison of two single positron annihilation signals is shown in Figure 4.2, with the buncher off and on. A time delay of 20 ns was set when the buncher was switched on. When the buncher is off, the FWHM of the annihilation time spread is 21 ns, while it decreases to ∼7 ns when the buncher is on.

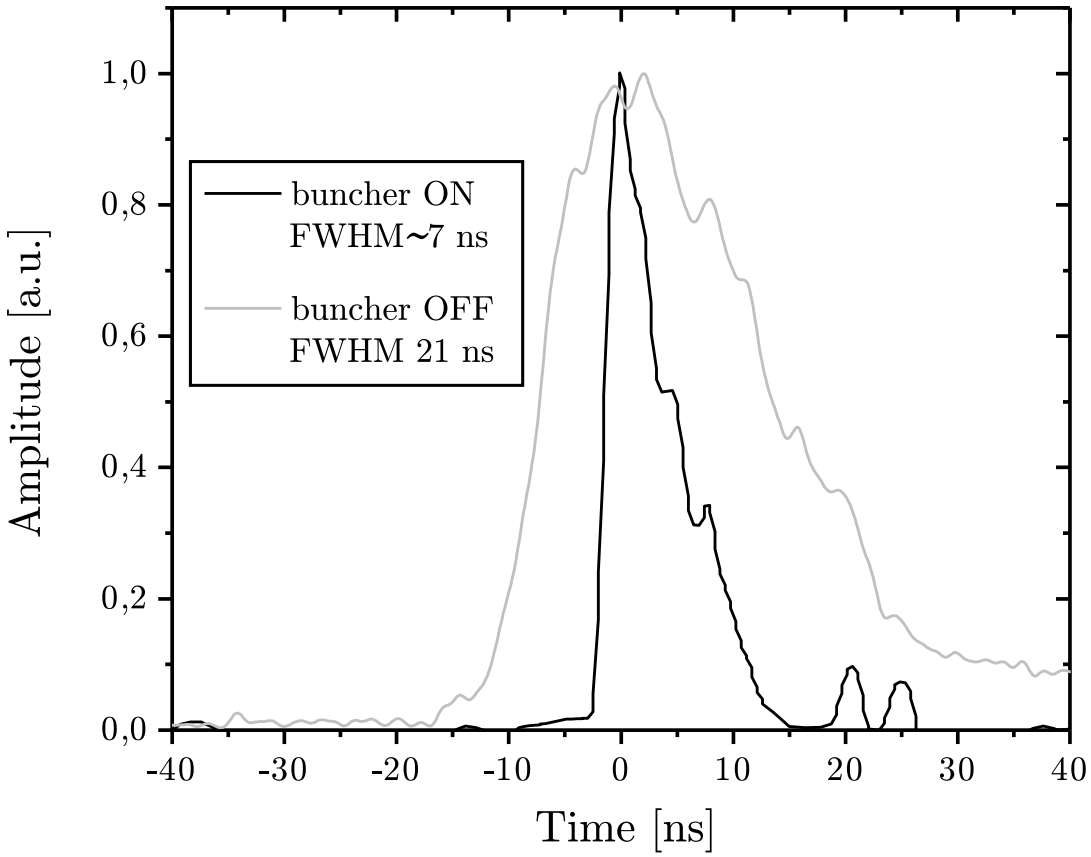

Figure 4.2: Comparison of the positron annihilation temporal spread on an Al plate with the buncher switched off (gray) and on (black). The FWHM is reduced from 21 ns to ∼7 ns when the high-voltage buncher potential is switched on. Note that the scale for the signal amplitude is linear.

4.1.2 Positron Focusing

The MCP assembly described in Section 3.5.3 was used to characterise the positron spot in the target region after the implementation of the buncher electrodes. The MCP assembly was placed ∼1 cm behind the target position. The sample holder can be moved to the edge of the test chamber with an actuator, in order to implant the positrons directly onto the MCP. The positron pulse was imaged on the phosphor screen of the MCP assembly with a charge-coupled device (CCD) camera. An image of the positron beam on the MCP is shown in Figure 4.3a, with the corresponding 3D map of the intensity shown in Figure 4.3b. For this measurement, the positron beam was compressed using the buncher electrodes and there was no strong magnetic field in the test chamber.

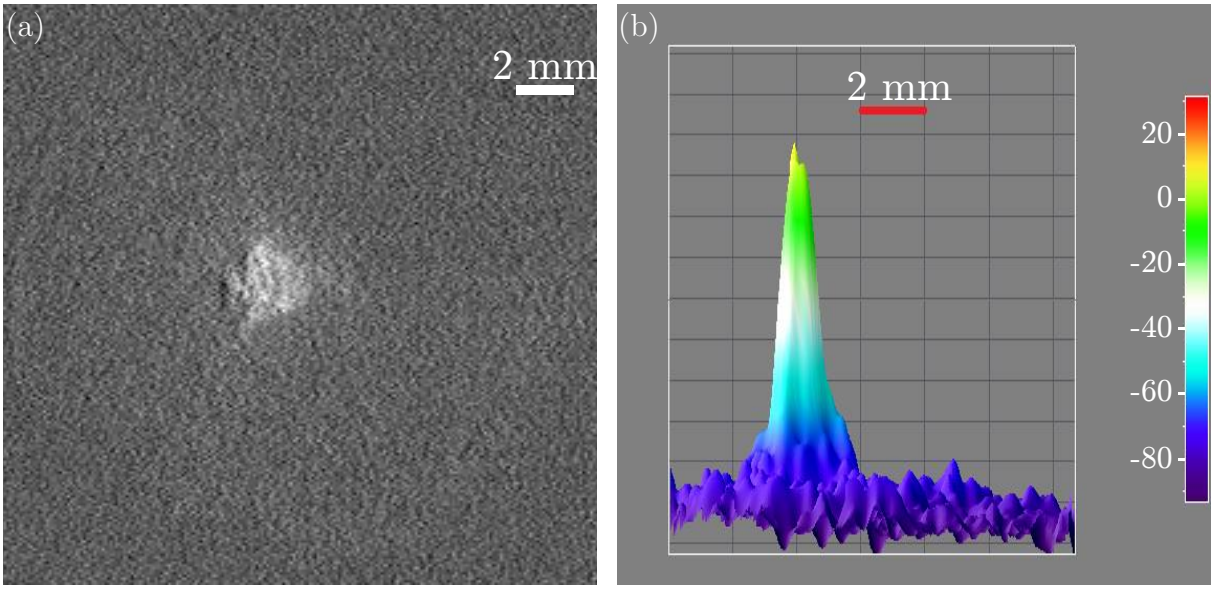

Figure 4.3: a) Image of the implanted positron beam acquired with an MCP assembly and `Hamamatsu ORCA-R2` camera, and b) the corresponding 3D intensity map. The positrons were implanted with the buncher on, and no magnetic field in the test chamber. The total diameter of the positron spot is less than 4 mm.

The diameter of the spot was found to be less than 4 mm. The efficiency of the transport along the entire transfer line has been estimated to be around 30%, by using a calibrated CsI detector connected to a photodiode [81]. This transport efficiency includes the losses during the magnetic transport, the change from magnetic to electrostatic transport and along the buncher. Thus, the spot of Figure 4.3a corresponds to the annihilation of around $1{\cdot}10^7$ positrons when $3{\cdot}10^7$ positrons are dumped from the accumulator. In this configuration, the magnetic field in the target region has been measured to be <1.8 Gauss in the direction parallel to the beam and <0.5 Gauss perpendicular to the beam, which is due to external magnetic fields.

Two coils capable of generating a field up to 300 Gauss are placed around the test chamber. These coils are used for experiments that require a certain magnetic field in the target region. When a magnetic field higher than 150 Gauss is set, the magnetic field has a positive effect on the extraction of the positron from the buncher and the fraction of positrons reaching the target increases to 40%. An image of the positron beam on the MCP with 250 Gauss in the test chamber is reported in Figure 4.4a and the corresponding 3D intensity map in Figure 4.4b. With this configuration, the diameter of the beam spot is somewhat larger at 5 mm. Taking into account the estimated transport efficiency, the image corresponds to about $1.2{\cdot}10^7$ positrons reaching the target when $3{\cdot}10^7$ positrons are dumped from the accumulator. So both the spot size and transport efficiency are increased by applying a magnetic field in the test chamber.

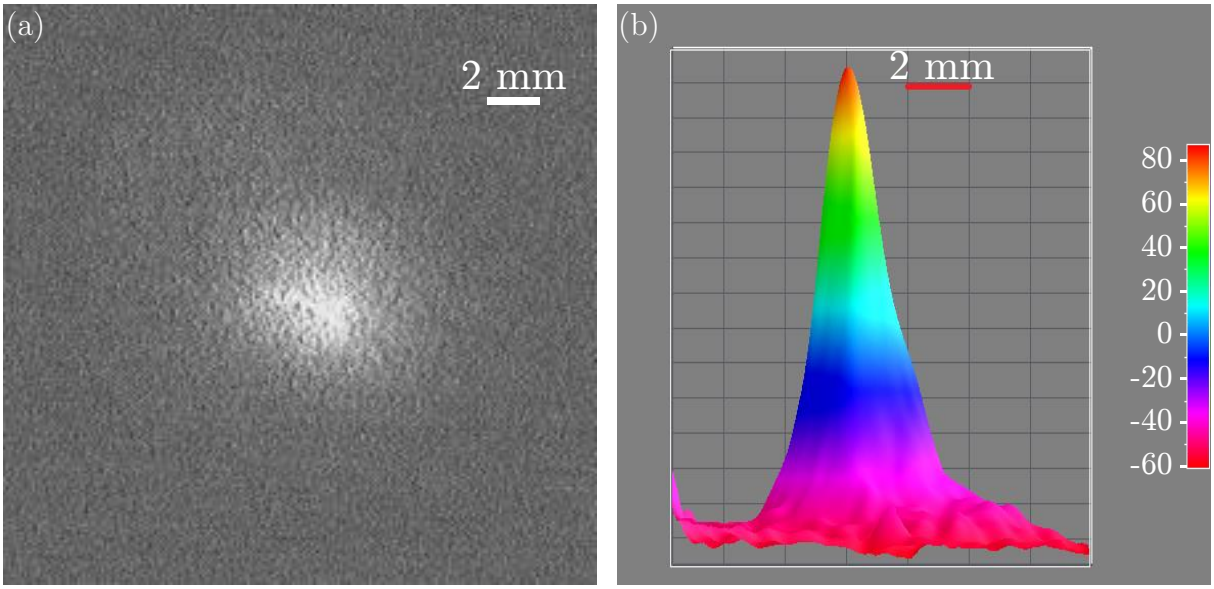

Figure 4.4: a) Image of the implanted positron beam acquired with an MCP assembly and `Hamamatsu ORCA-R2` camera, and b) the corresponding 3D intensity map. The positrons were implanted with the buncher switched on, and with a field of 250 Gauss applied in the test chamber. The total diameter of the positron beam is ∼5 mm.

4.2 Detector Comparison

The available PMTs and photon detectors were tested in order to find out which of the assemblies gave the best SSPALS spectra. The tests were performed with a field of 250 G in the test chamber and a potential of 4200 eV in the buncher electrodes, in order to benefit from the improved transport as described above. Figure 4.5 shows lifetime spectra acquired with a detector assembly consisting of a plastic scintillator and a `R11265-100 PMT` or a `H3378` PMT. These signals were obtained by annihilating the positron beam against the Al sample holder, which gives a baseline of zero positronium formation. The measurements were done by implanting 20 beam shots from the accumulator into the holder, and for each shot the spectrum was collected on the oscilloscope as described in Section 3.6. The signals were then normalised and averaged in order to create the results shown in the figure. It should be noted that the signal amplitude of these lifetime spectra is shown on a logarithmic scale. This is commonly done for lifetime spectra in order to highlight the features following the prompt peak, such as evidence of positronium formation.

The signals acquired with the two PMTs are very similar in the first parts of the spectra. The width of the prompt peak is approximately the same for the two PMTs. Note that the width of this peak relates to both the delay of the scintillator and the delay of the PMT, in addition to the temporal spread of the positron cloud itself. The similarity of the prompt peaks implies that the delay of the photon conversion is the same in the two PMTs. Following the prompt peak, the two PMTs behave very differently. The signal acquired with the `R11265-100` PMT falls off smoothly towards the background level of noise, with a relatively small amount of noise. The spectrum obtained with the `H3378` PMT also shows a general trend of a decrease, but with distinguishing after-peaks superimposed on it.

These after-peaks on the `H3378` PMT are very consistent in that they always appear with the same timing on the lifetime spectrum, and with the same relative amplitude to the main peak. This implies that the after-peaks are not a product of electrical noise or similar factors, but that they are rather due to some internal process in the PMT. These artefacts are in any case very detrimental to positron experiments, both with regard to measuring positronium formation and laser excitation of positronium. The `H3378` PMT was therefore not used any further during this work.

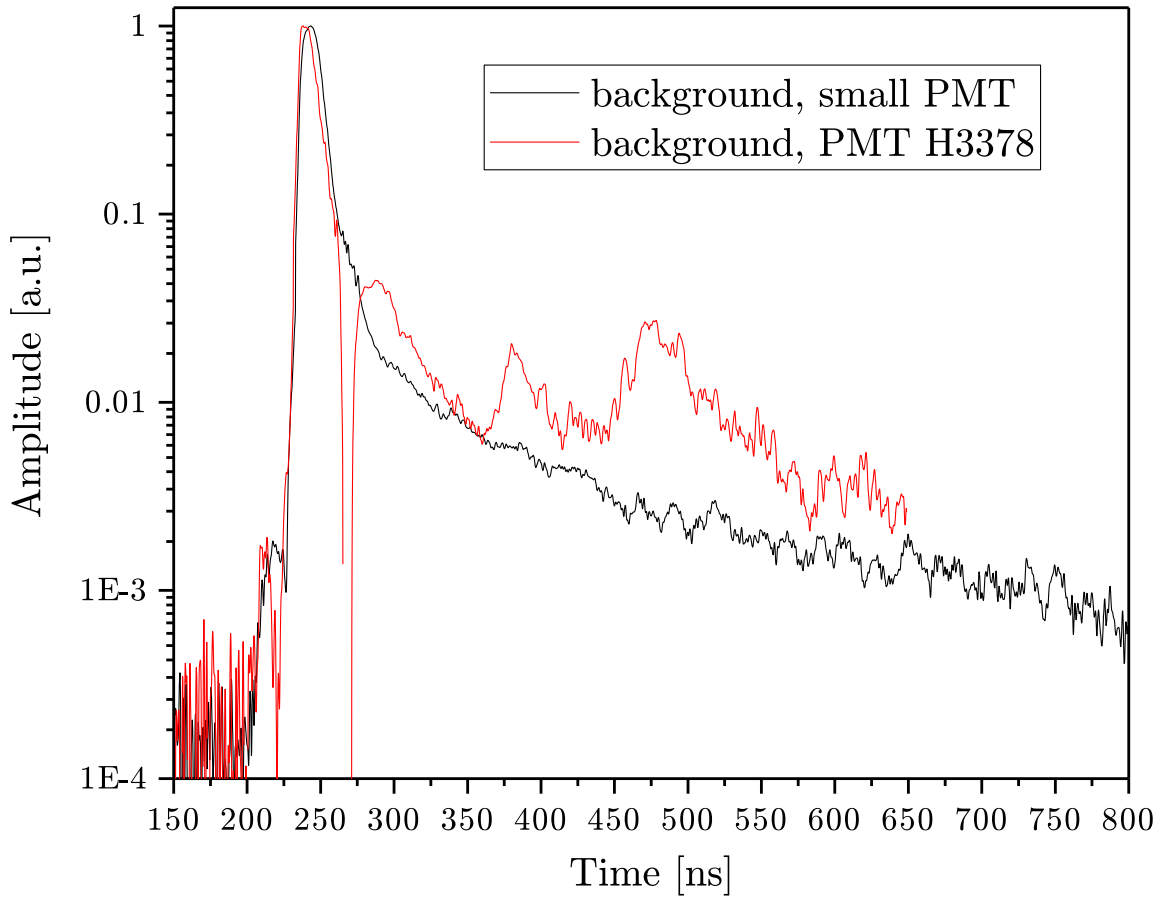

Figure 4.5: Comparison of the normalised positron annihilation signals against an Al plate, using a `R11265-100` PMT (black curve) and a `H3378` PMT (red curve) to record the signals. The same plastic scintillator was used as a gamma ray converter for these measurement. Each curve is the average of 20 beam shots from the accumulator. The signal on the `H3378` PMT is only recorded until the 650 ns time mark, due to the settings on the oscilloscope when the measurement was done. The two PMTs give lifetime spectra with a comparable width of the prompt peak, and similar amounts of noise on the signal prior to the prompt peak. After the prompt peak, the signal acquired with the `R11265-100` PMT falls off smoothly, and with a small amount of noise. The spectrum obtained with the `H3378` PMT displays characteristic after-peaks following the prompt peak, in addition to a valley directly after the main signal.

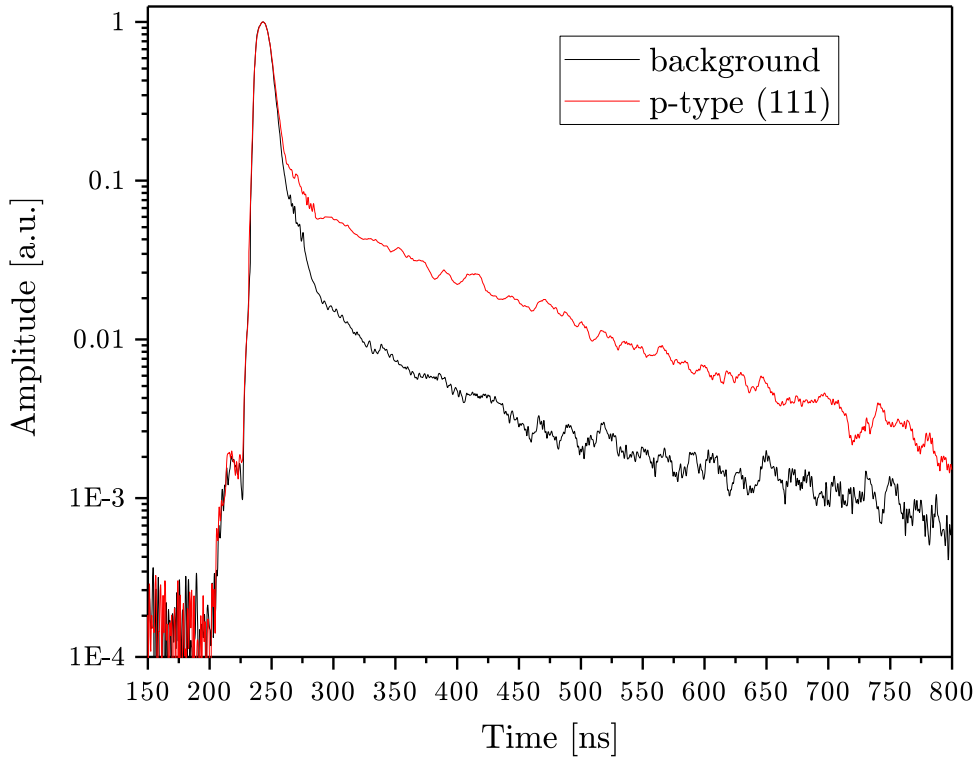

Figure 4.6: Comparison of normalised SSPALS spectra against an Al plate (black curve) and a p-type (111) sample (red curve), using a plastic scintillator and `R11265-100` PMT to record the data. Each spectrum is the average of 10 shots. The positronium formation from the p-type (111) sample is well-defined and the signal is not very noisy. The signal in the background spectrum falls slowly towards the background level of noise after the prompt peak, and does not reach the background level within the measurement time scale.

All the different photon converters have characteristics that affect the acquired SSPALS spectra, and the converters were therefore compared with regard to the features of the lifetime spectra. Figure 4.6 shows a comparison of two lifetime spectra acquired with a plastic scintillator and the `R11265-110` PMT. In this figure, one spectrum was obtained by annihilating positrons against the Al plate, while the other spectrum corresponds to implantation into the silicon p-type (111) sample. The p-type (111) sample was chosen as a comparison against the background because during the testing it displayed a clear difference from the background spectrum. This exact same procedure was then repeated for a PbF_2 radiator and a $PbWO_4$ crystal instead of the plastic scintillator.

The plastic scintillator has a low background noise, where the noise before the prompt peak has a normalised amplitude of around $2{\cdot}10^{-4}$. The temporal spread of the prompt peak is around 8 ns, which is in agreement with the lifetime spectra acquired in the section above. The signal after the prompt peak also has a low noise level, where the long tail of Ps formation would be easily distinguished. However, the tail of the background spectrum does not fall down to the background level of noise in the span of the measurement.

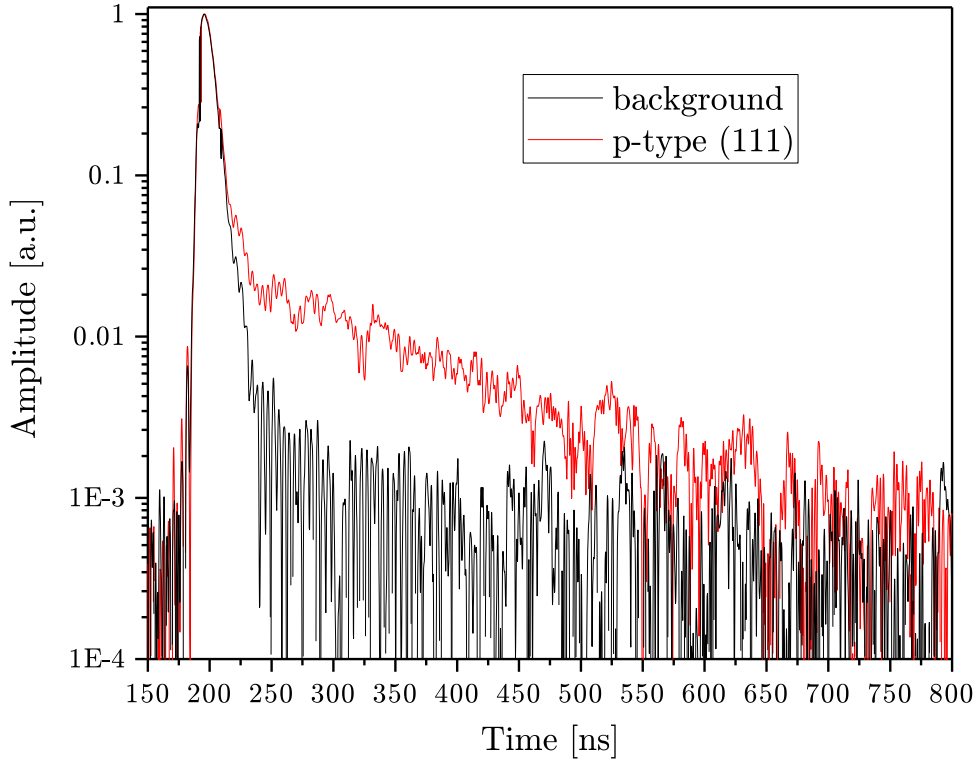

Figure 4.7: Comparison of normalised SSPALS spectra for annihilation against an Al plate (black curve) and a p-type (111) sample (red curve), using a PbF_2 Cherenkov radiator and `R11265-100` PMT to record the data. Each spectrum is an average of 10 beam shots from the accumulator. The measurements with the PbF_2 crystal have a very narrow FWHM of the prompt peak, and the background spectrum goes down to the background level of noise after the prompt peak within about 100 ns. The spectra are otherwise quite noisy, and the amplitude of the positronium formation following the prompt peak (red curve) is smaller than obtained with the plastic scintillator.

The corresponding lifetime spectra acquired with a PbF_2 detector is shown in Figure 4.7. The background noise level of the PbF_2 Cherenkov crystal is slightly higher, and reaches a normalised amplitude of $1{\cdot}10^{-3}$. The noise in the signal after the prompt peak is higher than for the plastic scintillator. An advantage of the PbF_2 crystal is the very narrow prompt peak, where the FWHM is around 6 ns. Additionally, the signal in the background spectrum, which contains only positron annihilation, drops off to the background noise level relatively fast compared to the plastic scintillator.

Due to the low quantum efficiency of the photon conversion in the PbF_2, the total amplitude of the prompt peak is only around 110 mV. As the other converters have a much larger quantum efficiency, their total signal amplitude is 6-8 V.

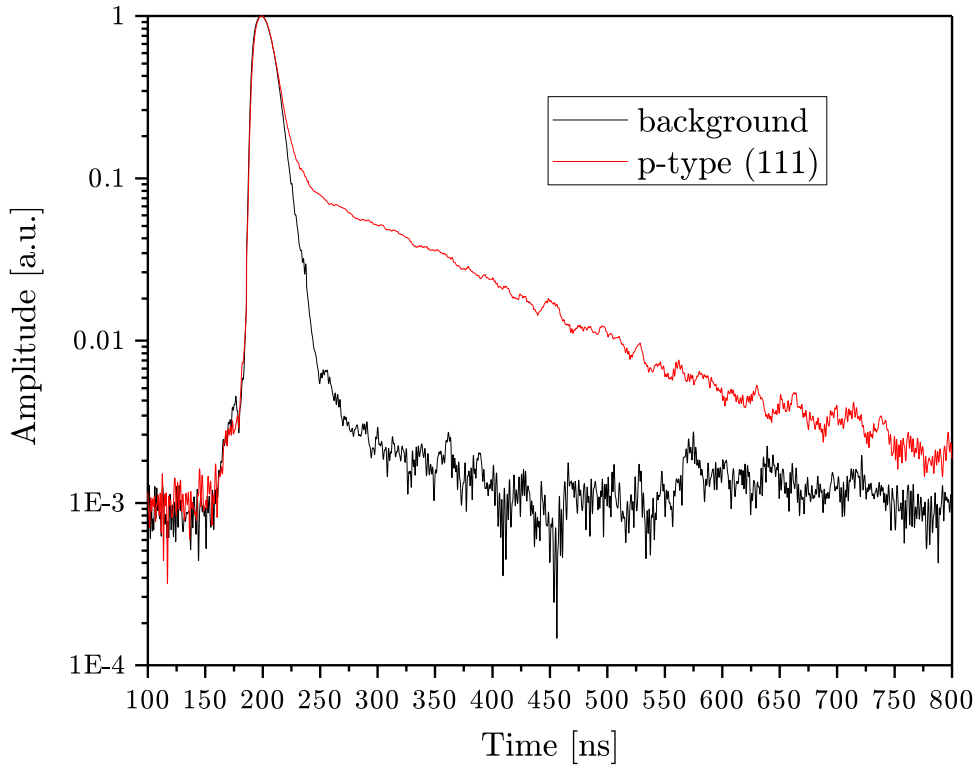

Figure 4.8: Comparison of normalised SSPALS spectra against an Al plate (black curve) and a p-type (111) sample (red curve), using a $PbWO_4$ scintillator and `R11265-100` PMT to record the data. Each spectrum is the average of 10 shots from the accumulator. The lifetime spectra obtained here are quite low with regard to the noise level, and the signal of the background spectrum drops off to the background level of noise very fast after the prompt peak. The $PbWO_4$ crystal also displays a much broader prompt peak than the other two photon converters.

Finally, Figure 4.8 shows the lifetime spectra acquired with a $PbWO_4$ crystal. The background noise level of the $PbWO_4$ crystal is quite high, as the normalised amplitude is around $1{\cdot}10^{-3}$. This detector also gives the widest prompt peak of the three detectors investigated here, with a temporal spread of 18 ns. Still, the signal obtained with the $PbWO_4$ has some clear advantages, with a low noise level in the signal after the prompt peak and a very fast drop-off for the background spectrum. In light of these advantages, this detector and the `R11265-100` PMT were chosen for the subsequent investigation of positron-positronium converters and laser excitation.

4.3 Positronium Formation in Different Converters

4.3.1 Lifetime Spectroscopy

Positronium formation in different positron-positronium converters was investigated by the SSPALS method described earlier. The data was recorded with a $PbWO_4$ scintillator coupled to a `Hamamatsu R11265-100` PMT, which was placed above the sample holder at a distance of 4 cm from the target center.

The SSPALS spectra of the p-type (111), p-type (100) and n-type (100) samples etched with a current of 10 mA can be seen in Figure 4.9. A background spectrum, where the positrons annihilated against a metal plate, is also included in this figure. Each spectrum has been constructed from 10 beam shots from the accumulator that have been averaged. The spectra have also been normalised in order to make the comparison of positronium formation straightforward.

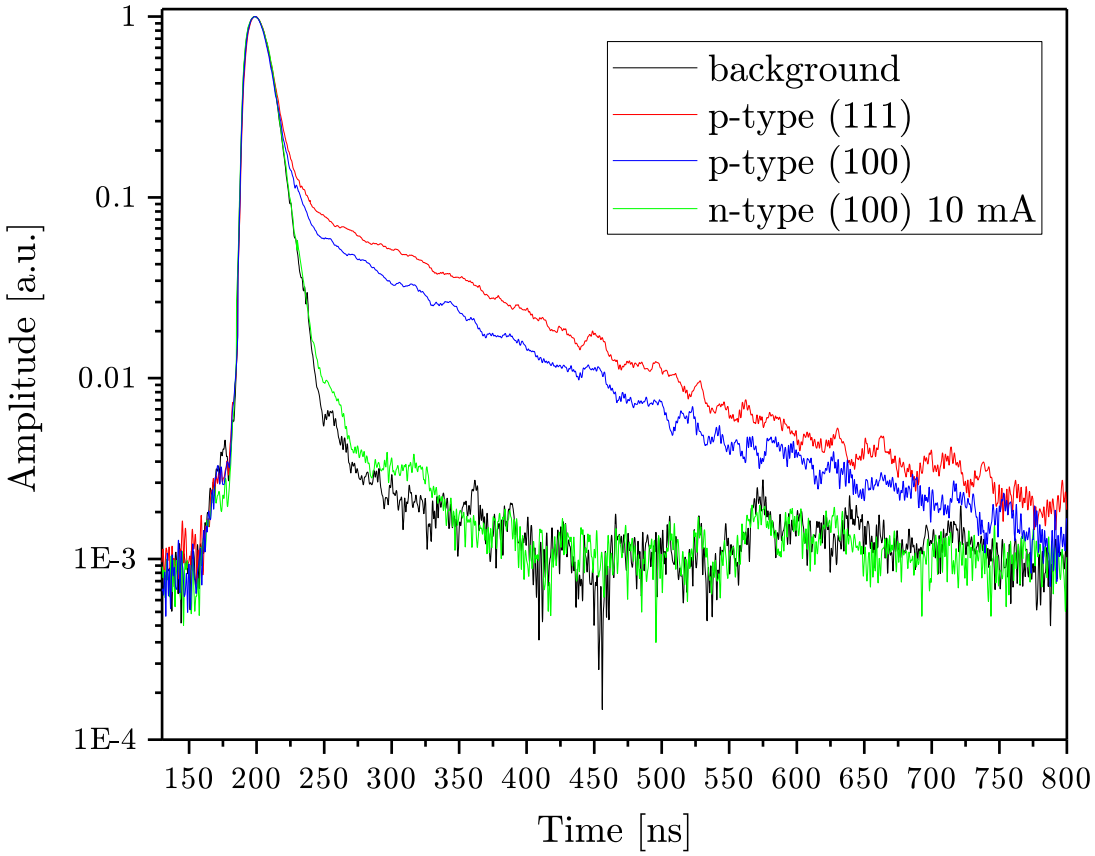

Figure 4.9: Comparison of normalised SSPALS spectra for an Al plate (black) and three nanochannel Si samples: p-type (111), p-type (100) and n-type (100) as indicated in the legend. The two p-type samples show higher levels of annihilation radiation after the prompt peak, with the p-type (111) sample having a slightly higher signal. The n-type sample shows only a small deviation from the background spectrum. All the spectra here are averages of 10 shots from the accumulator.

The annihilation against the metal plate displays a large annihilation peak followed by a fast decrease down to the noise level, as expected. The signal decreases down to the noise level in about 100 ns. The slower decrease in the signal for the p-type (100) and p-type (111) samples after the prompt peak indicates a non-background radiation, which is visible from ∼20 ns up to 600 ns after the prompt peak. The only possible source for this signal is long-lived o-Ps that is produced in the target. This long tail of positronium formation has a slightly higher intensity in the p-type (111) sample, which suggests that the formation rate is higher in this material. The spectrum obtained for the n-type (100) sample is very similar to the background spectrum with only positron annihilation, which indicates that the positronium formation in this sample is very low.

A lifetime spectrum was also recorded for the n-type (100) sample etched with a current of 20 mA, together with a new background. These spectra can be found in Figure B.1 in Appendix B. This sample, as with the other n-type sample, displayed no positronium formation. It should be noted that this measurement was made some time after the previous lifetime spectroscopy, and that these spectra may therefore not be directly comparable. Among other factors, this measurement was only possible during a period with significant magnetic fields in the surrounding area, which is visible as excess noise on the acquired data.

The acquired SSPALS spectra for the two p-type samples can be used to estimate the positronium lifetime. The probability of positronium decay follows an exponential distribution, such that the lifetime τ_{Ps} is the point where the total number of Ps atoms has decreased to a fraction $\frac{1}{e}$ of the original number of Ps atoms. This distribution is described by Equation 4.1 [66, 81], where N_0 is the initial number of Ps atoms, and t is the time since the initial Ps formation.

$$N(t) = N_0 e^{-\frac{t}{\tau}} \tag{4.1}$$

The lifetime can be determined from the SSPALS measurements by subtracting the background positron annihilation from the spectrum containing Ps formation. τ can then be found by making an exponential fit to the resulting curve in the time region after the prompt peak, as seen in Figure 4.10. The result is a lifetime in the p-type (111) sample of $\tau_{p(111)} = 142.8 \pm 1$ ns, and in the p-type (100) sample of $\tau_{p(100)} = 111 \pm 1$ ns. The positronium lifetime for the p-type (111) sample is consistent with the vacuum lifetime for positronium, while the p-type (100) sample shows a somewhat lower lifetime. This curve fitting and lifetime estimation was not done for the n-type samples, as they did not show any Ps production.

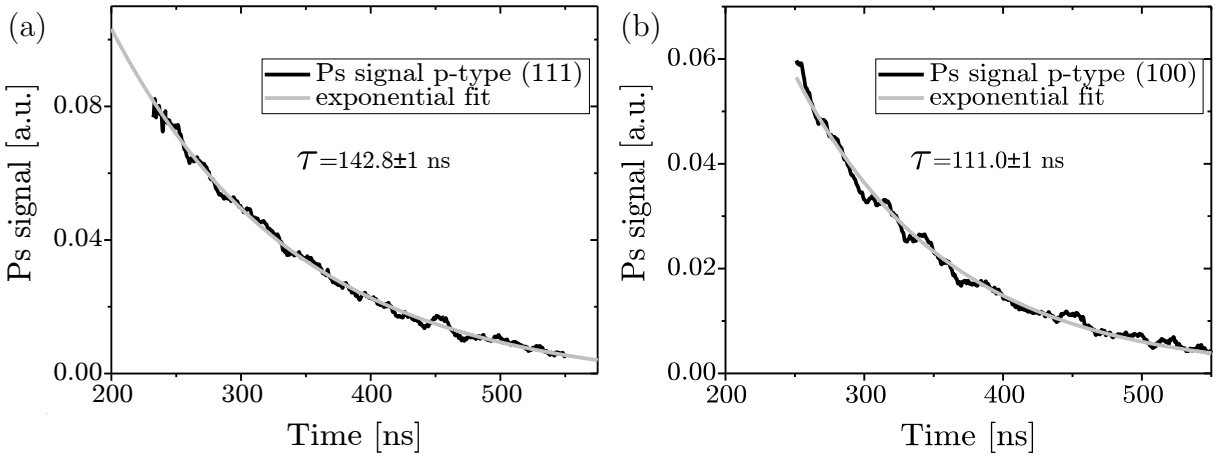

Figure 4.10: Lifetime estimation in the 50-350 ns region after the prompt peak for a) the p-type (111) sample and b) the p-type (100) sample. In both cases, the lifetime is estimated by taking the difference between the curve with Ps formation and the background. The smooth curve in each of these is the best fit of the acquired curve obtained from an exponential fit (see text). The Ps lifetime in the different samples is estimated as approximately 142 ns in the p-type (111) sample and 111 ns in the p-type (100) sample.

4.3.2 SEM Imaging

The p-type (111) sample and n-type (100) sample etched with 10 mA were further investigated using a scanning electron microscope (SEM). The imaging was done with a `ZEISS` SEM using a `SIGMA` field-emission gun, at CERN. Surface images of these samples are shown in Figure 4.11. The cross sections of the same p-type and n-type samples are shown in Figure 4.12. The samples were prepared for profile imaging by manually breaking them. During imaging, several sites of interest were investigated, both for the surface of each sample and the cross section. The images presented here are representative examples of the sample characteristics, meant to illustrate sample features on the nanometre scale.

The n-type (100) sample etched at 20 mA and the p-type (100) sample were both installed in the positron test chamber during the time period that the SEM imaging was performed, and no duplicates of these samples were available. Due to this, is was not possible to have these two samples imaged. However, a surface image of the p-type sample acquired earlier is shown in Figure 3.10a, and the n-type sample etched at 20 mA is expected to resemble the n-type etched at 10 mA.

The surface and profile images of the p-type silicon together indicate that the top layer of the sample contains a high density of oxidised nanochannels. This is supported by the high density of darker etched areas on the surface, which are very homogeneous with a diameter of 6-8 nm. The distance between these channels is on the same scale as the channel diameter. The profile image shows a lighter region close to the surface while

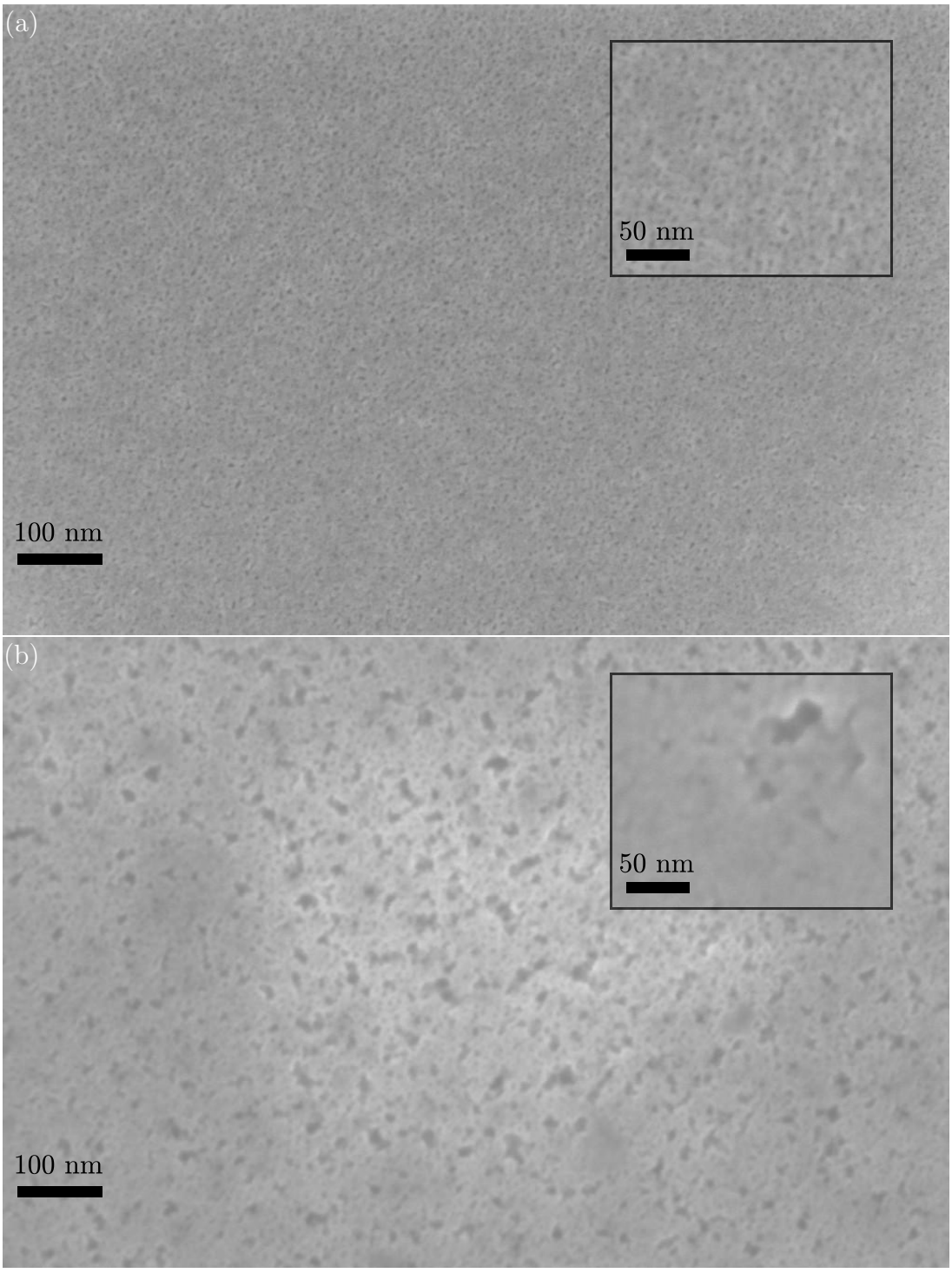

Figure 4.11: SEM images of the surface of a) a Si p-type (111) sample and b) a Si n-type (100) sample. The insets are images with a higher magnification. A working distance of 2.0 mm and a voltage level of 2 kV were used to obtain these images. The darker spots indicate areas where the etchant has attacked the surface of the sample. These areas are uniform in size for the p-type sample, with a diameter of <10 nm. The etched areas are also evenly distributed and have a very high density. For the n-type sample, the dark areas are of varying diameter and shape, and with a low surface density.

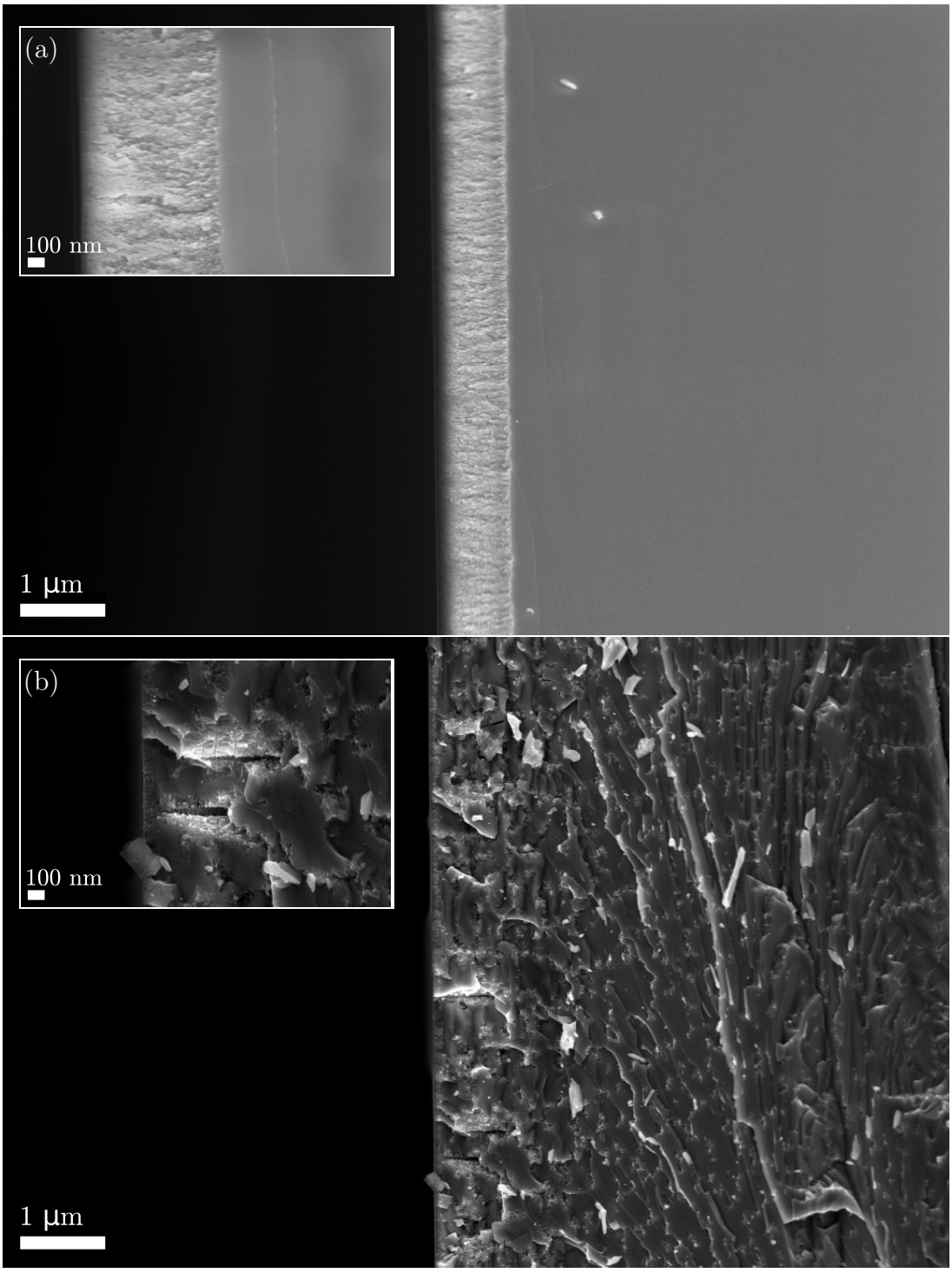

Figure 4.12: SEM images of the profile of a) a Si p-type (111) sample and b) a Si n-type (100) sample. The insets show images with a higher magnification. A working distance of 2.9 mm and a voltage of 3 kV were used to obtain these images. The profile of the p-type sample has a clear delineation between the gray silicon and the lighter silica area affected by the annealing. There is no such clear boundary for the cross-section of the n-type sample. This profile also looks rough when compared to the p-type, which is likely due to the cleaving process in preparation for the cross section images.

the bulk Si is dark, which indicates that the oxidised channels reach about 900 nm into the material. The depth of this region is constant throughout the cross section of the entire sample. It is difficult to discern individual nanochannels in this image, which is most likely due to the way in which the sample was fractured during preparation.

The same data for the n-type silicon suggests that this sample contains very few nanochannels. Although there are etched areas visible in the surface image, these are of varying size and of very low density. When considered in conjunction with the profile image, it is likely that these etched areas depict shallow pits rather than long nanochannels. These etched pits are very different from the ones in the p-type material, as the diameter varies from below 10 nm up to over 40 nm. The profile image of the n-type material displays no evidence of a high density of nanochannels or any oxidation of the material. Still, some structures that appear to be nanochannels are visible, such as in the inset in Fig. 4.12b. The fact that the lifetime spectrum of the second n-type sample etched at 20 mA shows no positronium formation indicates that changing the etching current, in this range, does not improve the nanochannel formation in n-type silicon.

4.4 Laser Excitation of Positronium

4.4.1 Excitation and Magnetic Quenching

The SSPALS technigue was also used to observe positronium laser excitation, and the results from the first attempt at positronium excitation is shown in Figure 4.13. This test was done by implanting the positrons into a silicon p-type (111) sample with and without the UV laser on. A magnetic field of 250 G was applied in the test chamber, in order to quench the excited Ps atoms and give a depopulation of the o-Ps annihilation following the prompt peak. Each spectrum shown here is the average of 15 beam shots from the accumulator, with 1000 pulses from the trap in every shot. The annihilation signal was detected with the $PbWO_4$ scintillator connected to the `R11265-100` PMT. The wavelength of the UV laser was 205.045 nm, with a power of 60 μJ. The time delay between the initial annihilation peak and the laser pulse was set to 16 ns. The effect of the laser pulse and magnetic field was investigated by calculating the $S(\%)$ parameter.

The $S(\%)$ parameter is a way of evaluating the excited fraction of o-Ps, and is the decrease in the area below the lifetime spectrum when the photoionisation or magnetic quenching effect is applied. This parameter is calculated from the areas A_{off} and A_{on} of the lifetime spectra, where the UV laser is off and on respectively, in the way shown in Equation 4.2 [60]. These areas are taken from a given time window after the prompt peak, were the depopulation of the o-Ps states is largest.

$$S(\%) = \frac{A_{off} - A_{on}}{A_{off}} \tag{4.2}$$

It should be noted that even though $S(\%)$ is a good tool for characterising the effect of the laser, it does not directly reflect the excited fraction of positronium atoms. The $S(\%)$ that is calculated from the lifetime spectra depends on a multitude of factors, including the efficiency of excitation to the $n = 3$ state, the subsequent fraction of quenched or photoionised positronium atoms and the spatial and temporal overlaps of the laser pulse and positronium cloud. The estimation of some of these factors is not straightforward, and it is therefore difficult to assess exactly how efficient the observed excitation is. Further considerations of the $S(\%)$ parameter can be found in the Section 5.4.

$S(\%)$ is the area difference between the spectrum with no laser and the spectrum with UV laser in the 250-450 ns range, where the range is indicated by the black bars in the inset of Fig. 4.13. With the magnetic quenching, $S(\%)$ is found to be 3.6±1.2%. This is a very small difference, but still consistent over several measurements.

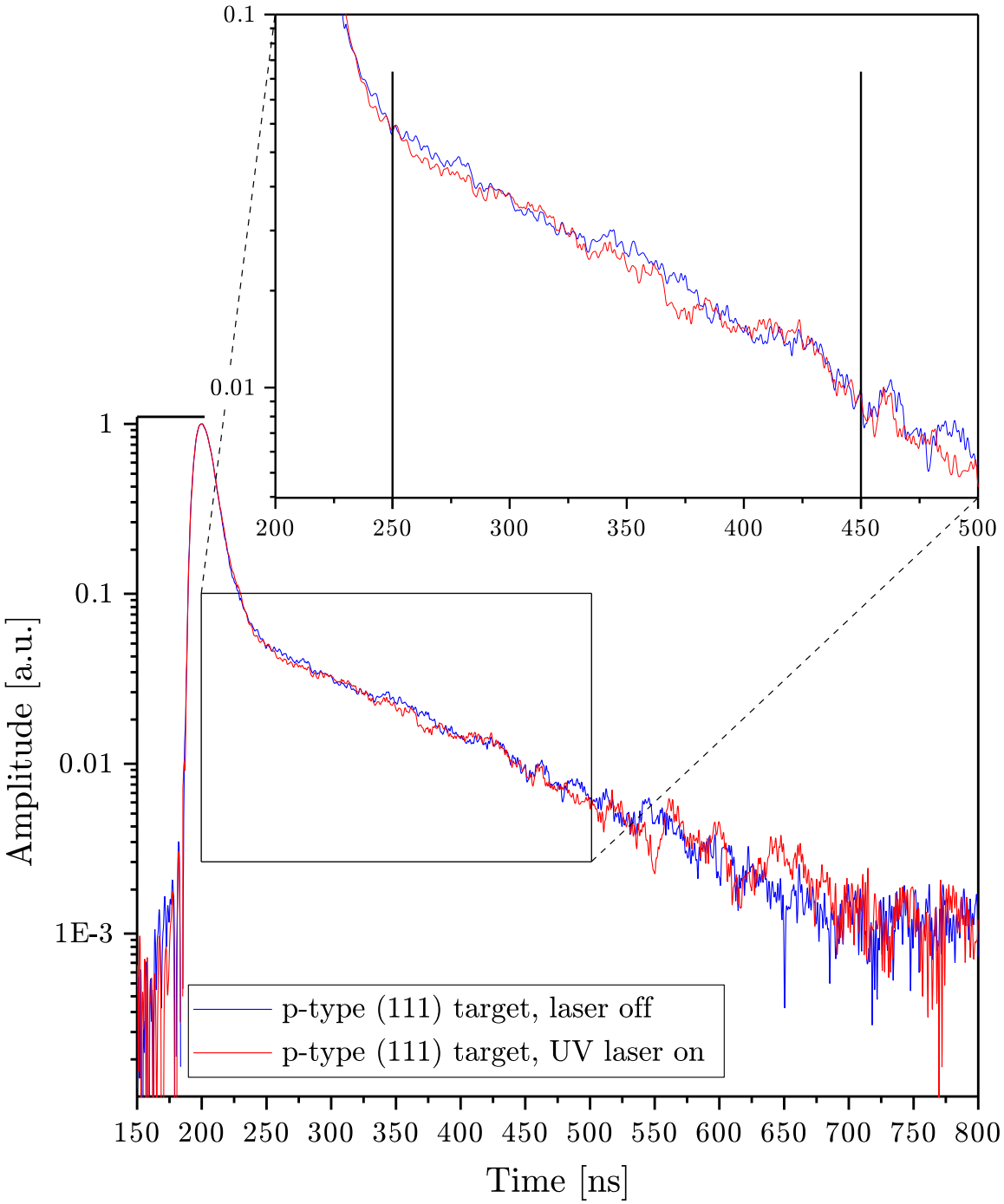

Figure 4.13: A comparison of normalised SSPALS spectra with positrons implanted in a p-type (111) sample, with a field of 250 G in the test chamber. Each spectrum is the average of 15 beam shots from the accumulator. One spectrum was acquired with the laser off (blue curve), and one with the UV laser turned on (red curve). Each curve is the average of 10 shots. The difference in areas between the two curves in the 250-450 ns range is 3.6%, where the range is indicated by the two black bars in the inset.

4.4.2 Excitation and Photoionisation

A second trial was performed in order to increase the measurable fraction of excited Ps. An IR laser pulse with an energy of 55 mJ and a wavelength of 1064 nm was superimposed on the UV laser pulse, and the measurements were otherwise performed in the same way as for the first test. The 250 G magnetic field was still switched on in the test chamber, as this field gave a sufficient beam focusing and a higher transport of positrons to the test chamber, when compared to a field of 0 G.

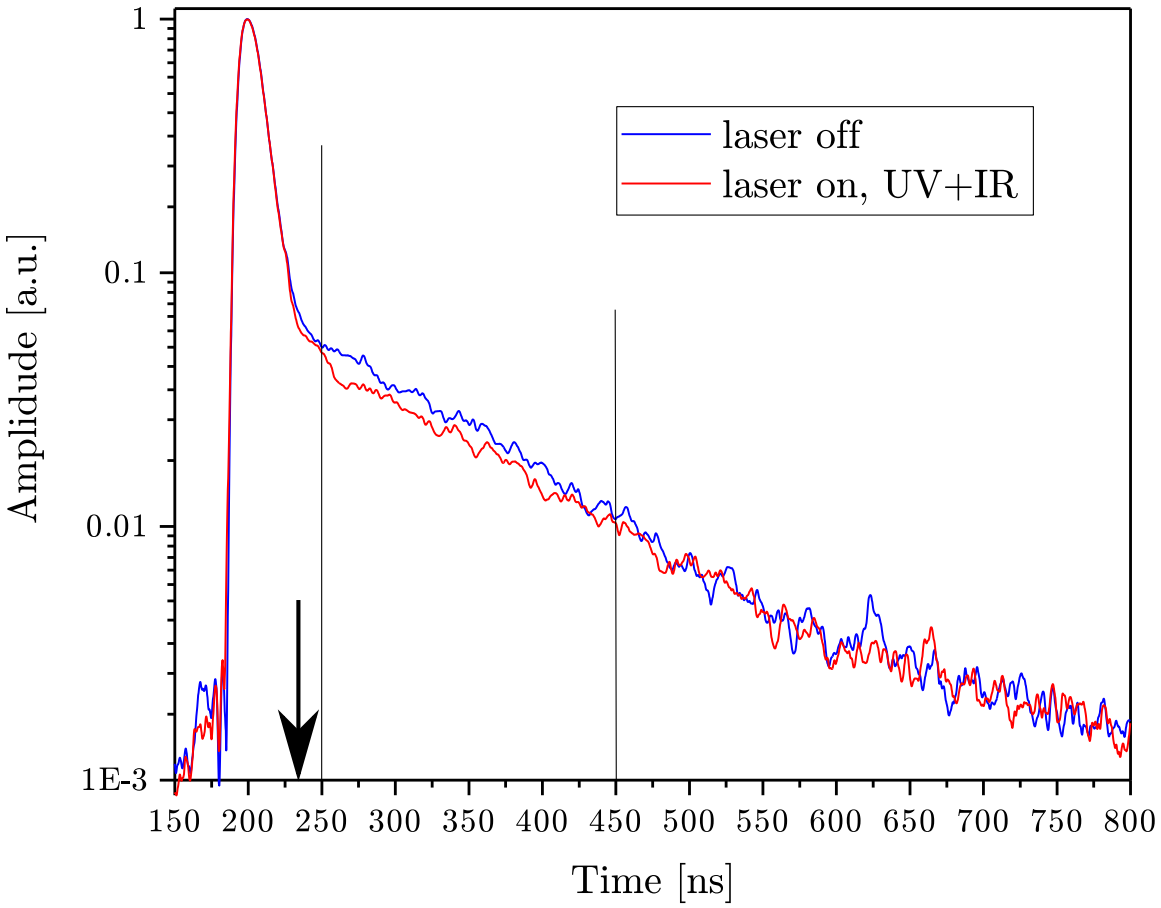

Figure 4.14: A comparison of normalised SSPALS spectra with positrons implanted in a p-type (111) sample. One measurement was done with the laser off (blue curve), and one with both the UV and IR laser on (red curve). Each curve is the average of 15 shots. The black arrow indicates the timing of the laser pulse. The area difference between the two curves in the range 250-450 ns is 15.5%, where the range is indicated by the black bars.

The purpose of the IR laser was to photoionise the excited fraction of positronium, in order to break the binding of these atoms. This was expected to lead to a further depopulation of the o-Ps states in the SSPALS spectrum following the IR laser pulse, and therefore a larger difference between the spectra with and without laser excitation, as explained in more detail in Section 2.7. The resulting SSPALS spectra are shown in Figure 4.14. In this case, the area difference between the two spectra in the 250-450 ns range

following the UV and IR laser pulses was 15.5±1.3%. So by employing photoionisation, $S(\%)$ increased more than four times compared to the magnetic quenching.

From these results it is obvious that $S(\%)$ is changed even though the same UV radiation is used for the excitation, which reinforces the idea that $S(\%)$ does not directly represent the fraction of excited Ps. It is then worth considering if $S(\%)$ is optimised with regard to the energies of the UV and IR laser energies. The measurements of $S(\%)$ as a function of the UV and IR laser energies are both shown in Appendix C. As expected, this fraction increases linearly in a certain energy range for the lasers, and then more or less reaches a plateau where $S(\%)$ stops increasing. These measurements show that the IR radiation used here is definitely in saturation, and the UV radiation is in, or very near, the saturation level. As a consequence, the number of excited Ps that are produced is not expected to be limited by the energies of the two laser pulses.

The linewidth of this excitation was then obtained by measuring the SSPALS spectra as a function of the UV wavelength. The $S(\%)$ parameter is plotted against the UV wavelength in Figure 4.15. The mean value of $S(\%)$ and its standard deviation were assessed for each wavelength, using 15 shots from the accumulator. The red curve in this figure is the best fit obtained with a Gaussian distribution. The UV wavelength that results in the largest $S(\%)$ parameter is 205.049±0.002 nm, which is quite consistent with the wavelength predicted from simulations [61]. This linewidth is dominated by the Doppler broadening effect, and has a FWHM of around 1100 GHz. It is worth noting here that the bandwidth of the laser is 112 GHz, which means that the laser is far from being able to address all the positronium atoms that are emitted from the sample.

The linewidth of the $S(\%)$ parameter can be used to evaluate the transverse positronium velocity and energy, as was done in [38]. The term 'transverse' refers to the direction parallel to the sample surface and along the axis of the laser pulse. The mean square velocity ($\langle v_x^2 \rangle$) can be calculated from Equation 4.3a, where $\Delta\lambda$ is the FWHM of the linewidth, λ_0 is the resonance wavelength of the excitation, and c is the speed of light. This equation assumes that the Doppler broadening of the excitation has a Gaussian distribution, which appears to be a good approximation from the Gaussian fit of the data in Fig. 4.15. The mean kinetic energy of the positronium parallel to the sample surface can then be found from Equation 4.3b, where m_{Ps} is the mass of the Ps atom.

$$\frac{\Delta\lambda}{\lambda_0} \approx \sqrt{8ln2}\sqrt{\frac{\langle v_x^2 \rangle}{c^2}} \tag{4.3a}$$

$$E_x = \frac{1}{2} m_{Ps} \langle v_x^2 \rangle \tag{4.3b}$$

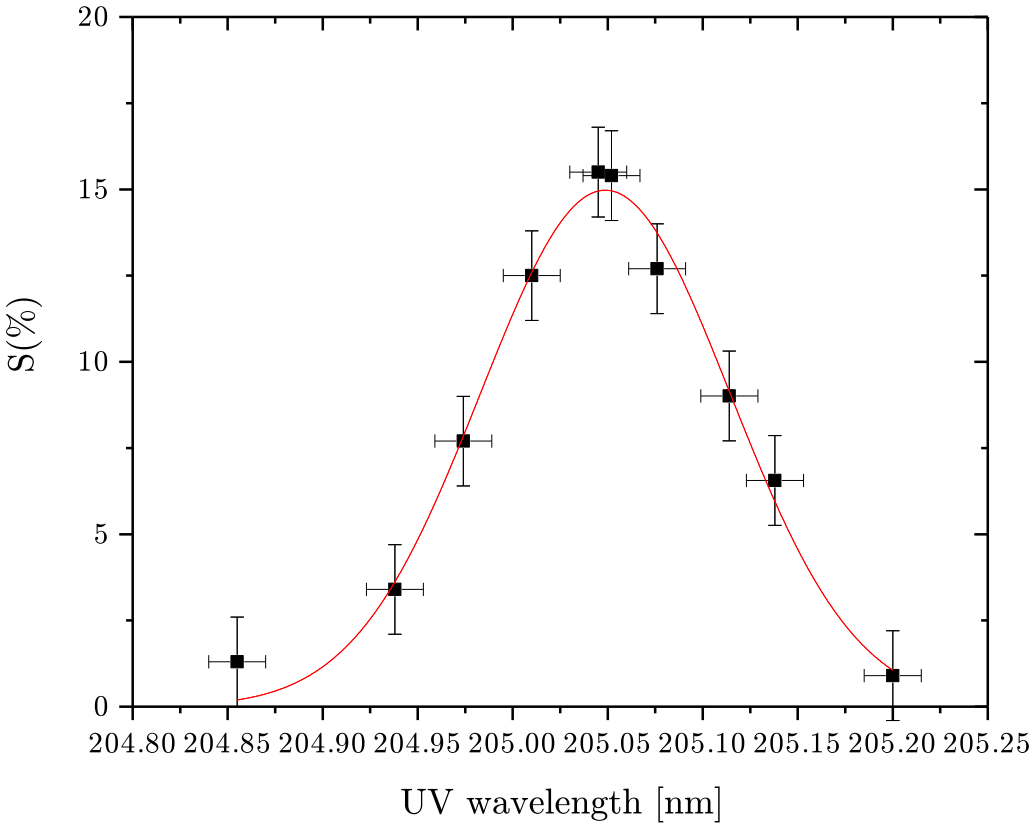

Figure 4.15: The $S(\%)$ parameter as a function of the UV wavelength, giving the linewidth of the 1^3S-3^3P transition. All these measurements were done with a UV laser energy of 60 μJ and an IR laser energy of 55 mJ. The excited fraction reaches a maximum close to the predicted resonant wavelength of 205.0474 nm, and decreases when the wavelength deviates from this wavelength. The solid curve is a Gaussian distribution fitted to the data. Each data point is an average of 15 lifetime measurements, where the error bars of the $S(\%)$ parameter is calculated from the standard deviation of these measurements. The error bars of the UV wavelength result from a variation in the laser output.

From these equations, the transverse velocity is estimated to be around 10^5 m/s. This corresponds to a transverse energy of about 150 meV. The temperature (T) can further be calculated from the relation in Equation 4.4, where k_b is the Boltzmann constant.

$$E = \frac{3}{2} k_b T \tag{4.4}$$

This indicates that the average transverse energy corresponds to a mean temperature of about 1200 K, which in turn means that the positrons are far from thermalised.

Chapter 5

Discussion

5.1 Consequences of the Buncher Implementation

A requirement for further experiments and measurements in the positron system is to have a temporal spread of the positron cloud which is much smaller than the positronium lifetime. This will result in a narrow FWHM of the SSPALS spectra, which makes it easier to detect positronium formation. Moreover, the amount of positrons transported to the test chamber should be maximised in order to improve the quality of the results. It has been shown that by optimising the synchronisation of the buncher electrodes, the FWHM of the positron annihilation signal can be reduced from 21 ns down to $\sim$7 ns. This has not been at the expense of the maximum signal amplitude in the test chamber. The maximum amplitude has been found to go from 40 mV to 110 mV when recording with the PbF_2 detector. This change in maximum amplitude is due to the compression of the beam, which concentrates the prompt peak and therefore understandably increases the recorded maximum signal.

A high-voltage potential of 4200 eV in the buncher electrodes was used to achieve these results. As mentioned earlier, the bias voltage in the buncher can be increased up to 10 keV. It will be possible to test a higher bias voltage in the future. This would serve to accelerate the positrons into the target with a higher energy. In addition, increasing the energy could even serve to further improve the temporal spread of the positron cloud, as the parabolic potential in the buncher is better at a high potential. Implanting positrons with a higher energy would also lead to deeper implantation in the target material, giving the formed positronium more time to thermalise on the way out.

The magnetic field in the test chamber was shown to affect the spatial dimensions of the positron cloud and the amount of positrons implanted in the target area. Efficient transport was possible both with and without a magnetic field, although the diameter of

the beam spot varied from less than 4 mm to 5 mm. The diameter of the converter target is 1 cm, and a change in the beam diameter from 4 to 5 mm should therefore not affect the positronium formation. Consequently, experiments can be done in this system both with and without a magnetic field in the test chamber.

5.2 The Impact of Detectors on the Measurements

5.2.1 Photomultiplier Tubes

For the investigation of detector assemblies, two PMTs were compared, and subsequently three different photon converters. The two `Hamamatsu` PMT models `H3378` and `R11265-100` were found to have similar prompt peaks, but the `H3378` PMT displayed very characteristic after-peaks following the prompt peak. It is difficult to determine the cause behind these after-peaks, as the `H3378` PMT is used in several positron systems [82, 83] and no similar issues have been reported. However, earlier research into PMT artefacts presented in [84] describes the possibility of after-peaks following the main signal, similar to what is seen here. In this case, the after-peaks are likely caused by a large number of photoelectrons striking the first dynode in the PMT, whereupon positive ions are released from the dynode materials. These ions travel back to and strike the photocathode material due to the bias voltage, which releases new electrons. The released electrons can create a new electron avalanche delayed by several nanoseconds compared to the main signal. This reaction can therefore produce smaller signals following the prompt peak. It is possible that these after-peaks could be removed by lowering the voltage gain on the `H3378` PMT or placing the entire detector assembly a bit further away from the test chamber. Any efforts to reduce the problem lead to a significantly lower main signal, and the `R11265-100` PMT was therefore used when investigating the photon detectors.

5.2.2 Photon Converters

An ideal photon converters for SSPALS should have three characteristics: a low noise level, a narrow FWHM of the prompt peak and a fast drop-off in the background spectrum. The $PbWO_4$ crystal was found to generate little signal noise, and the plastic scintillator was found to be even better in this regard. The PbF_2 crystal was found to have the narrowest prompt peak of the three detectors. The background spectra for the PbF_2 and $PbWO_4$ crystals were found to have a fast drop-off, while this was found to be delayed in the plastic scintillator.

The high noise level in the PbF_2 can be explained by the low quantum efficiency of

the crystal, which gives a lower total amplitude in the PbF_2 crystal. This leaves the PbF_2 converter more prone to electrical noise, since the same set-up is used for all the detectors. It is conceivable that this noise could be reduced by installing a voltage amplifier, which would amplify the signal before sending it to the oscilloscope. It might become useful in the future to carry out these tests, as PbF_2 crystals have been shown to be very good photon converters for SSPALS by Cassidy and Mills [85].

Another feature of the PbF_2 detector is that it gives a smaller total positronium signal when compared to the other detectors, which is as expected. This results directly from the way that the PbF_2 converts photons, which is by Cherenkov radiation. The low-energy gamma rays that are emitted from o-Ps annihilation are not registered by the PbF_2 detector. It has been estimated that Cherenkov radiators such as the PbF_2 give a positronium signal which is reduced by 30% as compared to other scintillators [85].

The drop-off of the background spectrum when measuring with the plastic scintillator is very slow compared to the other detectors, and does not reach the background level of noise within the time frame of the measurements. One reason for this could be that the plastic material has an excited state with a long lifetime, so that it continues emitting photons for several hundred nanoseconds. This after-glow in plastic scintillators and the consequences for SSPALS has earlier been discussed in [29].

The broadening of the prompt peak in the signal from the plastic scintillator and $PbWO_4$ crystal must be due to a delay in the fluorescence process, as this broadening is not found when using the PbF_2 radiator. These results fit well with earlier research which has indicated that the Pilot U scintillator has a decay time of 1.3 ns [86] and that the decay time of the $PbWO_4$ is around 10 ns at room temperature [87].

From the discussion of the different photon converters, it is clear that none of them are optimal with regard to positron spectroscopy. The main objective here was to find a detector which could easily measure the positronium formation and compare different positron-positronium converters. The slow drop-off of the background spectrum on the plastic scintillator would make it difficult to distinguish positronium formation and compare different positron targets, making this scintillator less than ideal. Moreover, it was also required that the converter had a noise level low enough to distinguish the depopulation of positronium states associated with laser excitation. Concerning this requirement, the PbF_2 crystal was found to be too noisy. The $PbWO_4$ crystal was therefore found to be the best suited photon detector in this system.

5.3 Positron-Positronium Converters

A significant result of the lifetime spectra of the nanochannel samples was that the p-type (111) sample had a larger fraction of Ps formation than the p-type (100) sample. This is most likely related to the structure of the channels inside the material. The SEM profile images of the p-type (111) sample do not clearly show nanochannels, but the theory predicts that the channels should not be formed perpendicular to the surface, as mentioned in Section 3.4.3. If the channels are formed at an angle to the surface, it is natural that there is more interconnectivity between these channels than what is found in p-type samples with a (100) crystal direction. More interconnectivity could result in a shorter path for the positrons when going from the silicon material to silica, where they form positronium, and then diffuse into a channel. As a result, a larger fraction of positrons would form positronium rather than annihilate in the silicon. Otherwise, the surface image for the p-type (111) sample shown in Fig. 4.11a and the earlier image of the p-type (100) sample shown in Fig. 3.10a indicate that these samples experience similar etch rates. Both samples demonstrate a high density of nanochannels that are homogeneous in size and in the same size range.

It should be noted here that this discussion has only concerned the relative amounts of positronium formed in the different samples, and not the absolute fraction of positronium atoms in relation to the implanted positrons. The method for calculating the amount of Ps atoms formed from an SSPALS spectrum requires both one signal for 0% Ps production and one for 100% Ps production [54]. From these measurements, a signal for zero Ps production is available (the background signal), but a signal with 100% Ps production cannot be made in the current set-up. Hence, only the relative fraction can be discussed, but this is sufficient for the purpose of this work. An estimate can be made from earlier measurements of p-type (100) samples by the positron group at the University in Trento [54, 75], which indicate that the Ps formation seen in the p-type (100) sample would correspond to a fraction of approximately 35% with the implantation energy used here. The production in the p-type (111) is somewhat higher, and therefore likely lies a few percentage points higher, i. e. around 40%.

The positronium lifetime was found to be approximately 142 ns in the p-type (111) sample and about 111 ns in the p-type (100) sample. A lifetime of 142 ns in the p-type (111) sample is practically the vacuum lifetime, which implies that the Ps atoms either spend a very short time in the channels before being emitted into vacuum, or that they somehow are less affected by the pick-off annihilation compared to the other sample. As the positrons are shot into the samples with the same energy, it is expected that they are implanted at the same depth. Consequently, the Ps atoms should spend a comparable

amount of time inside the samples. If it is the case that the p-type (111) has a larger degree of interconnectivity and porosity, this could explain the higher lifetime in addition to the increased fraction of Ps production which was discussed above. Larger interconnectivity in the p-type (111) material would indicate that there is more free space, and thus that the Ps atoms are less affected by pick-off annihilation (annihilation against electrons in the channel walls). As a result, a larger amount of the Ps atoms formed in the p-type (111) sample would be able to escape into vacuum and have a lifetime of 142 ns, as compared to the p-type (100) sample.

The n-type samples proved to have a behaviour quite different from the p-type samples that were tested, and displayed zero or close to zero positronium production. Based on the SEM images, it seems that no positronium is formed because there are no nanochannels in the etched material, and not necessarily because there is something inherently faulty with n-type silicon as a positron-positronium converter material. A new etching technique would probably need to be developed in order to form nanochannels in the n-type sample. This would of course require further testing with different etching currents and maybe a different solution with HF and ethanol. Such tests would further necessitate systematic experiments with SEM imaging and measurements of Ps formation.

5.4 Laser Excitation of Positronium

5.4.1 Excitation to $n = 3$

The results from the excitation to the $n = 3$ state of positronium were presented, where the signal from depopulation of the o-Ps states following the laser pulses was enhanced by magnetic quenching and photoionisation. When the 250 G field is used to quench the positronium atoms, $S(\%)$ is measured at around 3.6%, and this increases to 15.5% when an IR laser pulse is used in addition to photoionise the atoms.

The depopulation observed with magnetic quenching is very small, albeit consistent, and a signal of this size is difficult to work with. Tests such as the wavelength scan and laser energy scan would not be practical, due to the low total amplitude of the signal. Moreover, unexpected new magnetic or electric fields in the AD facility could completely disrupt the signal, as both the detectors and the positron system are susceptible to external disturbances. One could imagine the possibility of increasing $S(\%)$ via quenching by increasing the magnetic field, but this is not a feasible strategy. The upper limit of the solenoids installed around the test chamber is 300 G, so increasing the magnetic field would not be possible in this set-up. More importantly, employing a higher magnetic field would eventually lead to quenching of ground state o-Ps directly to p-Ps. This would lead

to a depopulation of the o-Ps states not related to laser excitation, making it impossible to evaluate laser excitation in the way presented here.

A wavelength scan for $S(\%)$ was performed, using the IR laser, which gave an expected Gaussian distribution of the linewidth. This linewidth was found to have a FWHM of around 1100 GHz, which is much larger than the bandwidth of the laser at 112 GHz. This means that the bandwidth of the laser would only able to cover about 10% of the emitted Ps atoms, which clearly will contribute to a lower than optimal excitation efficiency. The mean velocity of the Ps atoms in the transverse direction was also estimated from the Doppler broadening, which resulted in a velocity of $\sim 10^5$ m/s and thereby an average temperature of around 1200 K. This Ps temperature is in agreement with earlier results [75], which have shown that a higher implantation energy is typically needed in order to obtain thermal Ps. It is clear that the thermalisation and corresponding Doppler distribution of the Ps atoms affect the excitation efficiency, and that this will need to be addressed in order to improve the efficiency. The Doppler broadening would be much smaller if the emitted Ps atoms were thermal, and this would result in the laser being able to excite a larger fraction of Ps.

Several persuasive lines of evidence have been presented that together indicate that the observed results are due to $n = 3$ excitation. The resonance wavelength of the excitation was found to be in close agreement with the theoretically calculated values, with some uncertainties due to physical effects [61]. This excitation has never been reported before, and is an important step in achieving Rydberg excitation of positronium for the AEGIS experiment.

Considering these results, it is evident that the improvements described above and tests of different positron-positronium converters proved to be important for the laser excitation. For instance, the temporal spread of the positrons being implanted into a sample is related to that of the emitted Ps cloud. Consequently, if the temporal spread of the positron cloud is small, the temporal spread of the Ps cloud will also be small. As the laser spot is quite small and the power of the UV laser is largest in the middle of the spot, Ps excitation is most efficient when the Ps atoms are concentrated around the laser spot. A small temporal spread is therefore crucial in order to achieve a good geometrical overlap between the positronium cloud and the laser, and hence an efficient excitation.

5.4.2 $S(\%)$ and the Excitation Efficiency

As mentioned earlier, $S(\%)$ is not directly the excited fraction of Ps atoms and is affected by several elements in the measurements. The factors that affect $S(\%)$ as calculated in these measurements can be divided into three categories: factors that are related to

the n=3 excitation, factors that are related to the photoionisation, and lastly general parameters that are associated with both lasers such as the geometrical and temporal overlap. Concerning the n=3 excitation, there is a maximum theoretical fraction of Ps atoms that can be excited to this state, with 65% being the percentage calculated by Villa [88] for this set-up. This maximum fraction can be reduced if the energy of the laser is not high enough to bring the excitation into saturation, or if the bandwidth of the radiation is not enough to address all of the atoms in the emitted cloud. Similarly, the IR laser will have a related maximum fraction of atoms that can be photoionised and a saturation energy for which this maximum fraction is reached. The results presented in Appendix C indicate that the energies for the UV and IR lasers were within the saturation region for the n=3 excitation and further photoionisation. The geometrical and temporal overlap of the positronium cloud and the laser pulses are perhaps the factors that are most difficult to estimate. It was possible to calculate the mean transverse velocity of Ps from the wavelength scan, but the total velocity distribution is still unknown. Due to this, the geometrical overlap between the laser pulses and the Ps atoms cannot be decoupled from the temporal misalignment of the lasers. Further discussion of the $S(\%)$ parameter will be included in [89].

Although the exact factors influencing $S(\%)$ are difficult to estimate at present, the efficiency of the positronium excitation can still be evaluated. The first experiment with the UV laser radiation was carried out with the idea of detecting the excitation signal by looking at the depopulation of o-Ps due to magnetic quenching. An estimation of the maximum number of Ps atoms that could be quenched in this magnetic field has been performed with a custom simulation code made by Villa, Castelli and Caravita. This code does the numerical diagonalisation of the full interaction Hamiltonian of positronium in magnetic and electrical fields. The details on this simulation and corresponding code are under publication [90]. Initial results from this simulation have shown that a 15% reduction of the o-Ps population after the laser should be observable. This assumes a field of 250 G in the test chamber, as well as ideal spatial and temporal overlapping of the laser pulse and positronium cloud. Due to the factors affecting $S(\%)$ discussed above, a signal of only 3.6% was detected in the experiment.

Based on the experience described above, the remaining experiments were carried out using photoionisation of the excited Ps. Assuming that the photoionisation was 100% efficient, as suggested by Fig. C.1b, an ideal signal of 65% can be estimated. From the experiments presented here, an efficiency of around 15.5% was observed. Notably, the ratios of the observed signals and the ideal signals predicted by the simulations, both in the quenching and photoionization experiments, agree with each other. For the quenching

experiment the ratio is 3.6%÷15%=0.24, while for the photoionisation measurement it is 15.5%÷65%=0.238. The resulting excitation efficiency can then be estimated by calculating the ratio of the measured signal versus the expected signal, and is found to be around 24% in both cases. This means that about 16% of the positronium atoms emitted into vacuum are excited to the $n = 3$ state.

The excitation efficiency calculated here appears to go against what was found for the spectral overlap between the laser pulse and the Doppler broadening of the laser, which implied that the excitation efficiency should not surpass 10%. This discrepancy could be explained by for instance a power broadening of the laser bandwidth at high laser intensities. Power broadening with a corresponding higher excitation efficiency than expected has been observed earlier by Cassidy *et al.* [60], for the excitation of positronium to the $n = 2$ state. This phenomenon should therefore not be completely unexpected for the excitation to the $n = 3$ state.

The results obtained here and the earlier simulations also explain why $S(\%)$ is over 4 times larger when photoionisation is used, compared to the magnetic quenching. Independent of which technique is used, the estimated maximum amount of Ps atoms that can be excited by the UV laser pulse is 65%. When the IR laser pulse is used for ionisation, all the excited atoms may be ionised and can therefore contribute to $S(\%)$. In the case of magnetic quenching, the depopulation of o-Ps is dependent on the mixing of Ps states and subsequent rapid annihilation as p-Ps. The mixing of states caused by the field is a limiting step with this technique, which means that only a fraction of the excited Ps atoms are affected. As mentioned, an estimated total efficiency of only 15% can be reached with quenching, which means that the quenching will always give a smaller $S(\%)$ when the same set-up is used. Indeed, the photoionisation gives an $S(\%)$ parameter which is 4.3 times higher than for quenching, both in the observed and the ideals signals from the simulations.

Chapter 6

Conclusion

The goals of this work was to:

1. Implement the buncher electrodes in the electrostatic transport,
2. Find a detector that improved the SSPALS spectra,
3. Investigate different types of positron-positronium converters,
4. Make the first attempts at exciting positronium to the n=3 state.

Initially, only the implementation of the buncher and the investigation of converter materials were planned for this thesis. Several detector assemblies became available during the work, and some time was therefore dedicated to testing PMTs and photon converters. Due to results being obtained rapidly from these experiments, arrangements were also made for the laser excitation of positronium. The success in meeting these goals and the overall consequences for the experiment is evaluated in the following.

Positron bunching. Positron re-bunching was achieved in the buncher electrodes following the dumping of the positron cloud from the accumulator. The implementation of this high-voltage buncher potential lead to a reduction in the temporal spread of the implanted positrons by a factor of 3, as well as a much more efficient transport to the test chamber.

Detectors. The characteristics of several PMTs and gamma ray converters were exemplified through SSPALS spectra. It was found that the individual characteristics of the photon converters had a great impact on the obtained SSPALS spectra. An assembly with satisfying characteristics was found, and then used throughout the subsequent experiments.

Positronium formation. Several targets have been investigated as positron-positronium converters. The p-type (100) sample had characteristics as expected from earlier studies such as [75]. The p-type (111) sample exhibited a higher production of Ps than the p-type (100) sample, and appeared to have a high density of uniform nanochannels reaching a depth of approximately 900 nm. The two n-type (100) samples showed no evidence of positronium formation, and the obtained SEM images indicated that this was due to an near absence of nanochannels in the samples.

Laser excitation. Excitation of positronium to the $n = 3$ state was demonstrated for the first time in this study, using the p-type (111) sample as a converter material. This result is a significant step towards the planned antihydrogen formation process in the AEGIS experiment. A range of UV wavelengths were investigated, and these indicated a Doppler broadening of the linewidth and a resonance wavelength close to the expected one. The transverse positronium velocity calculated from this Doppler broadening showed that the positronium atoms were not thermalised, as expected from previous research.

This study has also demonstrated that extensive work with optimising the electrostatic transport in the positron system was necessary to obtain successful laser excitation. Additionally, it proved essential to find a detector assembly sensitive enough to detect the depopulation of o-Ps in the SSPALS spectra following the laser pulses.

6.1 Future Outlook

Although significant progress has been achieved during this study, further work is necessary on the positron system. Future developments in the system will be centred on two different areas: improving the results obtained during this work, and realising other planned experiments.

It will be necessary to lower the temperature of the produced o-Ps in order to create cold antihydrogen. Presently, the transversal positronium temperature is 1200 K. This transversal temperature can be reduced by using p-type silicon with a crystal orientation of (100), as the nanochannels are perpendicular to the material surface and the produced Ps will be emitted perpendicularly into the vacuum. Additionally, it is possible to increase the bias voltage used in the buncher electrodes. This will give the positrons a higher kinetic energy, which in turn will implant them further into the converter. The positronium in the nanochannels will therefore experience more collisions on their way out from the material, which will overall lower the average positronium energy. This method will probably require

a new optimisation of the electro-optical transport in the last part of the transfer line. If an energy below room temperature is required, it will also be possible to install a cryostat in the test chamber.

Rydberg excitation of positronium will be the next step towards forming antihydrogen through charge-exchange reactions, as highly-excited Ps atoms are needed for this process. Rydberg excitation will require the use of an IR laser in the 1650-1700 nm range, which should be fairly simple to align and synchronise as all the necessary components are already installed. This excitation can be tested on both the p-type (100) and p-type (111) samples, in order to find the best target with regard to positronium temperature and excitation efficiency.

In addition to these improvements and experiments related to the antihydrogen formation, the positron system can also be used for other research into positronium formation and manipulation. For instance, developing a method for creating positronium via positron-positronium converters that work in transmission mode is a very interesting topic, as transmission mode targets have not been tested in detail yet. Testing transmission mode positronium formation in the AEGIS system would require some modifications of the test chamber, but should be feasible to do in the near future. Moreover, laser cooling of positronium as a subject has thus far received little attention, and is another possible research avenue in the positron system.

Bibliography

[1] G. Drobychev *et al.* (AEgIS collaboration), "Proposal for the AEGIS experiment at the CERN Antiproton Decelerator (Antimatter Experiment: Gravity, Interferometry, Spectroscopy)," Tech. Rep. SPSC-P-334. CERN-SPSC-2007-017, CERN, Geneva, 2007.

[2] A. P. M. Jr. and M. Leventhal, "Can we measure the gravitational free fall of cold Rydberg state positronium?," *Nucl. Instrum. Meth. B*, vol. 192, no. 1–2, pp. 102 – 106, 2002.

[3] M. Amoretti *et al.* (ATHENA collaboration), "Production and detection of cold antihydrogen atoms," *Nature*, vol. 419, no. 6906, pp. 456–459, 2002.

[4] G. B. Andresen *et al.* (ALPHA collaboration), "Trapped antihydrogen," *Nature*, vol. 468, no. 7324, pp. 673–676, 2010.

[5] I. B. Larsen, "On the characterisation and improvement of a positron-positronium converter," Semester project, Norwegian University of Science and Technology (NTNU), 2014.

[6] P. A. M. Dirac, "The quantum theory of the electron," in *Proceedings of the Royal Society of London A: Mathematical, Physical and Engineering Sciences*, vol. 117, pp. 610–624, The Royal Society, 1928.

[7] C. D. Anderson, "Energies of cosmic-ray particles," *Phys. Rev.*, vol. 41, no. 4, pp. 405–421, 1932.

[8] J. Kónya and N. M. Nagy, "4 - Radioactive Decay," in *Nuclear and Radiochemistry* (J. Kónya and N. M. Nagy, eds.), pp. 49 – 82, Oxford: Elsevier, 2012.

[9] J. Hubbell, "Electron–positron pair production by photons: A historical overview," *Radiation Physics and Chemistry*, vol. 75, no. 6, pp. 614 – 623, 2006.

[10] A. Bettini, *Introduction to Elementary Particle Physics*. Cambridge University Press, 2014.

[11] T. D. MacMahon and A. P. Baerg, "The electron capture to positron branching ratio in the decay of ^{22}Na," *Can. J. Phys.*, vol. 54, no. 14, pp. 1433–1437, 1976.

[12] R. H. Howell, R. A. Alvarez, and M. Stanek, "Production of slow positrons with a 100-MeV electron linac," *Appl. Phys. Lett.*, vol. 40, no. 8, pp. 751–752, 1982.

[13] D. B. Cassidy and A. P. Mills, "The production of molecular positronium," *Nature*, vol. 449, no. 7159, pp. 195–197, 2007.

[14] J. Estrada, T. Roach, J. N. Tan, P. Yesley, and G. Gabrielse, "Field ionization of strongly magnetized rydberg positronium: A new physical mechanism for positron accumulation," *Phys. Rev. Lett.*, vol. 84, no. 5, pp. 859–862, 2000.

[15] R. G. Greaves and C. M. Surko, "Solid neon moderator for positron-trapping experiments," *Can. J. Phys.*, vol. 74, no. 7-8, pp. 445–448, 1996.

[16] T. L. Watson, *Accumulation and Manipulation of Positron Plasmas for Antihydrogen Production.* PhD thesis, University of Wales, 2003.

[17] P. J. Schultz and K. G. Lynn, "Interaction of positron beams with surfaces, thin films, and interfaces," *Rev. Mod. Phys.*, vol. 60, no. 3, pp. 701–779, 1988.

[18] W. H. Cherry, *Secondary Electron Emission Produced from Surfaces by Positron Bombardment.* PhD thesis, Princeton University, 1958.

[19] A. Vehanen, K. Lynn, P. Schultz, and M. Eldrup, "Improved slow-positron yield using a single crystal tungsten moderator," *Appl. Phys. A*, vol. 32, no. 3, pp. 163–167, 1983.

[20] A. P. Mills, "Further improvements in the efficiency of low-energy positron moderators," *Appl. Pys. Lett.*, vol. 37, no. 7, pp. 667–668, 1980.

[21] C. Hugenschmidt, B. Straßer, and K. Schreckenbach, "Investigation of positron work function and moderation efficiency of Ni, Ta, Pt and W(100)," *Applied Surface Science*, vol. 194, no. 1–4, pp. 283 – 286, 2002. 9th International Workshop on Slow Positron Beam Techniques for Solids and Surfaces.

[22] M. Weber, A. Schwab, D. Beckek, and K. Lynn, "Solid neon moderated electrostatic or magnetic positron beam," *Hyperfine Interactions*, vol. 73, no. 1-2, pp. 147–157, 1992.

[23] A. P. Mills and E. M. Gullikson, "Solid neon moderator for producing slow positrons," *Appl. Pys. Lett.*, vol. 49, no. 17, pp. 1121–1123, 1986.

[24] E. M. Gullikson and A. P. Mills, "Positron dynamics in rare-gas solids," *Phys. Rev. Lett.*, vol. 57, no. 3, pp. 376–379, 1986.

[25] K. F. Canter, P. G. Coleman, T. C. Griffith, and G. R. Heyland, "Measurement of total cross sections for low energy positron-helium collisions.," *Journal of Physics B: Atomic and Molecular Physics*, vol. 5, no. 8, pp. L167–L169, 1972.

[26] P. J. Schultz, K. G. Lynn, W. E. Frieze, and A. Vehanen, "Observation of defects associated with the Cu/W(110) interface as studied with variable-energy positrons," *Phys. Rev. B*, vol. 27, pp. 6626–6634, Jun 1983.

[27] P. G. Coleman, ed., *Positron beams and their Applications.* World Scientific Co. Pte Ltd., 2000.

[28] R. Brusa, W. Deng, G. Karwasz, and A. Zecca, "Doppler-broadening measurements of positron annihilation with high-momentum electrons in pure elements," *Nucl. Instrum. Meth. B*, vol. 194, no. 4, pp. 519 – 531, 2002.

[29] D. B. Cassidy, "Experiments with many-positron systems," in *Proceedings of the International School of Physics "Enrico Fermi"; Physics with Many Positrons*, vol. 174, p. 1–75, IOS Press, 2010.

[30] D. H. E. Dubin and T. M. O'Neil, "Trapped nonneutral plasmas, liquids, and crystals (the thermal equilibrium states)," *Rev. Mod. Phys.*, vol. 71, no. 1, pp. 87–172, 1999.

[31] C. M. Surko and R. G. Greaves, "Emerging science and technology of antimatter plasmas and trap-based beams," *Physics of Plasmas*, vol. 11, no. 5, pp. 2333–2348, 2004.

[32] C. M. Surko, M. Leventhal, and A. Passner, "Positron plasma in the laboratory," *Phys. Rev. Lett.*, vol. 62, no. 8, pp. 901–904, 1989.

[33] T. J. Murphy and C. M. Surko, "Positron trapping in an electrostatic well by inelastic collisions with nitrogen molecules," *Phys. Rev. A*, vol. 46, no. 9, pp. 5696–5705, 1992.

[34] R. Greaves and C. Surko, "Positron trapping and the creation of high-quality trap-based positron beams," *Nucl. Instrum. Meth. B*, vol. 192, no. 1-2, pp. 90–96, 2002.

[35] B. M. Jelenković, A. S. Newbury, J. J. Bollinger, W. M. Itano, and T. B. Mitchell, "Sympathetically cooled and compressed positron plasma," *Phys. Rev. A*, vol. 67, no. 6, p. 063406, 2003.

[36] J. Notte and J. Fajans, "The effect of asymmetries on non-neutral plasma confinement time," *Physics of Plasmas*, vol. 1, no. 5, pp. 1123–1127, 1994.

[37] R. G. Greaves and C. M. Surko, "Radial compression and inward transport of positron plasmas using a rotating electric field," *Physics of Plasmas*, vol. 8, no. 5, pp. 1879–1885, 2001.

[38] D. B. Cassidy, R. G. Greaves, V. E. Meligne, and A. P. Mills, "Strong drive compression of a gas-cooled positron plasma," *Appl. Pys. Lett.*, vol. 96, no. 10, p. 101502, 2010.

[39] R. C. Davidson, *Physics of Nonneutral Plasmas*. Redwood City, CA: Addison-Wesley, 1990.

[40] M. Deutsch, "Evidence for the formation of positronium in gases," *Phys. Rev.*, vol. 82, no. 3, pp. 455–456, 1951.

[41] M. Deutsch, "Three-quantum decay of positronium," *Phys. Rev.*, vol. 83, no. 4, pp. 866–867, 1951.

[42] C. M. Surko, G. F. Gribakin, and S. J. Buckman, "Low-energy positron interactions with atoms and molecules," *J. Phys. B: At. Mol. Opt. Phys.*, vol. 38, no. 6, pp. R57–R126, 2005.

[43] A. H. Al-Ramadhan and D. W. Gidley, "New precision measurement of the decay rate of singlet positronium," *Phys. Rev. Lett.*, vol. 72, no. 11, pp. 1632–1635, 1994.

[44] R. S. Vallery, P. W. Zitzewitz, and D. W. Gidley, "Resolution of the orthopositronium-lifetime puzzle," *Phys. Rev. Lett.*, vol. 90, no. 20, p. 203402, 2003.

[45] A. Rich, "Recent experimental advances in positronium research," *Rev. Mod. Phys.*, vol. 53, no. 1, pp. 127–165, 1981.

[46] L. B. Madsen and P. Lambropoulos, "Scaling of hydrogenic atoms and ions interacting with laser fields: Positronium in a laser field," *Phys. Rev. A*, vol. 59, no. 6, pp. 4574–4579, 1999.

[47] M. J. Puska and R. M. Nieminen, "Theory of positrons in solids and on solid surfaces," *Rev. Mod. Phys.*, vol. 66, no. 3, pp. 841–897, 1994.

[48] G. R. Massoumi, N. Hozhabri, W. N. Lennard, and P. J. Schultz, "Doubly differential positron-backscattering yields," *Phys. Rev. B*, vol. 44, no. 7, pp. 3486–3489, 1991.

[49] M. P. Petkov, M. H. Weber, K. G. Lynn, and K. P. Rodbell, "Porosity characterization by beam-based three-photon positron annihilation spectroscopy," *Appl. Pys. Lett.*, vol. 79, no. 23, p. 3884, 2001.

[50] Y. Nagashima, M. Kakimoto, T. Hyodo, K. Fujiwara, A. Ichimura, T. Chang, J. Deng, T. Akahane, T. Chiba, K. Suzuki, B. T. A. McKee, and A. T. Stewart, "Thermalization of free positronium atoms by collisions with silica-powder grains, aerogel grains, and gas molecules," *Phys. Rev. A*, vol. 52, no. 1, pp. 258–265, 1995.

[51] D. B. Cassidy, P. Crivelli, T. H. Hisakado, L. Liszkay, V. E. Meligne, P. Perez, H. W. K. Tom, and A. P. Mills, "Positronium cooling in porous silica measured via doppler spectroscopy," *Phys. Rev. A*, vol. 81, no. 1, p. 012715, 2010.

[52] S. Mariazzi, A. Salemi, and R. S. Brusa, "Positronium cooling into nanopores and nanochannels by phonon scattering," *Phys. Rev. B*, vol. 78, no. 8, 2008.

[53] C. G. Fischer, M. H. Weber, C. L. Wang, S. P. McNeil, and K. G. Lynn, "Positronium in low temperature mesoporous films," *Phys. Rev. B*, vol. 71, no. 18, p. 180102, 2005.

[54] S. Mariazzi, P. Bettotti, S. Larcheri, L. Toniutti, and R. S. Brusa, "High positronium yield and emission into the vacuum from oxidized tunable nanochannels in silicon," *Phys. Rev. B*, vol. 81, no. 23, p. 235418, 2010.

[55] R. W. Siegel, "Positron annihilation spectroscopy," *Annu. Rev. Mater. Sci.*, vol. 10, no. 1, pp. 393–425, 1980.

[56] S. J. Tao, "Positronium annihilation in molecular substances," *The Journal of Chemical Physics*, vol. 56, no. 11, pp. 5499–5510, 1972.

[57] M. Eldrup, D. Lightbody, and J. Sherwood, "The temperature dependence of positron lifetimes in solid pivalic acid," *Chemical Physics*, vol. 63, no. 1–2, pp. 51 – 58, 1981.

[58] D. B. Cassidy, S. H. M. Deng, H. K. M. Tanaka, and A. P. Mills, "Single shot positron annihilation lifetime spectroscopy," *Appl. Pys. Lett.*, vol. 88, no. 19, p. 194105, 2006.

[59] D. B. Cassidy, M. W. J. Bromley, L. C. Cota, T. H. Hisakado, H. W. K. Tom, and A. P. Mills, "Cavity induced shift and narrowing of the positronium Lyman-α transition," *Phys. Rev. Lett.*, vol. 106, no. 2, 2011.

[60] D. B. Cassidy, T. H. Hisakado, H. W. K. Tom, and A. P. Mills, "Efficient production of Rydberg positronium," *Phys. Rev. Lett.*, vol. 108, no. 4, 2012.

[61] F. Castelli and M. G. Giammarchi, "Laser-driven positronium excitation in the AEGIS antimatter experiment at CERN," in *Proceedings of the International School of Physics "Enrico Fermi"; Physics with Many Positrons*, vol. 174, p. 311–336, Amsterdam: IOS Press, 2010.

[62] R. Caravita, *Laser apparatus for Exciting Positronium in AEGIS Positronium Spectroscopy Experiment*. PhD thesis, University of Milan, 2012.

[63] M. Charlton, "Antihydrogen production in collisions of antiprotons with excited states of positronium," *Physics Letters A*, vol. 143, no. 3, pp. 143 – 146, 1990.

[64] A. Kellerbauer *et al.* (AEgIS collaboration), "Proposed antimatter gravity measurement with an antihydrogen beam," *Nucl. Instrum. Meth. B*, vol. 266, no. 3, pp. 351 – 356, 2008. Low Energy Positron and Positronium Physics Proceedings of the {XIV} International Workshop on Low Energy Positron and Positronium Physics.

[65] M. Doser *et al.* (AEgIS collaboration), "AEGIS: An experiment to measure the gravitational interaction between matter and antimatter," *J. Phys.: Conf. Ser.*, vol. 199, p. 012009, 2010.

[66] B. Rienäcker, "Investigation of positron/positronium converter targets at AEgIS (CERN)," Master thesis, Munich University of Applied Sciences, 2015.

[67] M. J. T. Collier, L. V. Jørgensen, O. I. Meshkov, D. P. van der Werf, and M. Charlton, "Development and testing of a positron accumulator for antihydrogen production," AIP Publishing, 1999.

[68] R. Khatri, M. Charlton, P. Sferlazzo, K. G. Lynn, A. P. Mills, and L. O. Roellig, "Improvement of rare-gas solid moderators by using conical geometry," *Appl. Pys. Lett.*, vol. 57, no. 22, pp. 2374–2376, 1990.

[69] L. Penasa, L. D. Noto, M. Bettonte, S. Mariazzi, G. Nebbia, and R. S. Brusa, "Positron bunching system for producing positronium clouds into vacuum," *J. Phys.: Conf. Ser.*, vol. 505, p. 012031, 2014.

[70] K. Canter, "Slow-positron optics," in *Proceedings of the International School of Physics "Enrico Fermi"; Positron Spectroscopy of Solids*, vol. 125, p. 361–369, Amsterdam: IOS Press, 1995.

[71] D. B. Cassidy, S. H. M. Deng, R. G. Greaves, and A. P. Mills, "Accumulator for the production of intense positron pulses," *Rev. Sci. Instrum.*, vol. 77, no. 7, p. 073106, 2006.

[72] F. Castelli, "The positronium atom as a benchmark for Rydberg excitation experiments in atomic physics," *The European Physical Journal Special Topics*, vol. 203, no. 1, pp. 137–150, 2012.

[73] T. E. Wall, A. M. Alonso, B. S. Cooper, A. Deller, S. D. Hogan, and D. B. Cassidy, "Selective production of Rydberg-Stark states of positronium," *Phys. Rev. Lett.*, vol. 114, no. 17, p. 173001, 2015.

[74] S. Cialdi, I. Boscolo, F. Castelli, F. Villa, G. Ferrari, and M. G. Giammarchi, "Efficient two-step positronium laser excitation to Rydberg levels," *Nucl. Instrum. Meth. B*, vol. 269, no. 13, pp. 1527 – 1533, 2011.

[75] S. Mariazzi, P. Bettotti, and R. S. Brusa, "Positronium cooling and emission in vacuum from nanochannels at cryogenic temperature," *Phys. Rev. Lett.*, vol. 104, no. 24, p. 243401, 2010.

[76] R. S. Brusa, L. D. Noto, S. Mariazzi, and G. Nebbia, "Positronium cooling at cryogenic temperature for advanced experiments," *J. Phys.: Conf. Ser.*, vol. 505, p. 012038, 2014.

[77] M. J. Sailor, *Fundamentals of Porous Silicon Preparation*, pp. 1–42. Wiley-VCH Verlag GmbH & Co. KGaA, 2011.

[78] W. R. Leo, *Techniques for Nuclear and Particle Physics Experiments: A How-To Approach*. Springer Science + Business Media, 1994.

[79] J. V. Jelley, "Cerenkov radiation and its applications," *Br. J. Appl. Phys.*, vol. 6, no. 7, pp. 227–232, 1955.

[80] J. L. Wiza, "Microchannel plate detectors," *Nucl. Instrum. Methods*, vol. 162, no. 1–3, pp. 587 – 601, 1979.

[81] S. Aghion *et al.* (AEgIS collaboration), "Positron bunching and electrostatic transport system for the production and emission of dense positronium clouds into vacuum," *Submitted to Nucl. Instrum. Meth. B*, 2015.

[82] H. Saito, Y. Nagashima, T. Kurihara, and T. Hyodo, "A new positron lifetime spectrometer using a fast digital oscilloscope and baf2 scintillators," *Nucl. Instrum. Meth. A*, vol. 487, no. 3, pp. 612 – 617, 2002.

[83] L. Hui, S. Yundong, Z. Kai, P. Jingbiao, and W. Zhu, "A simplified digital positron lifetime spectrometer based on a fast digital oscilloscope," *Nucl. Instrum. Meth. A*, vol. 625, no. 1, pp. 29 – 34, 2011.

[84] B. M. Concannon, V. M. Contarino, D. M. Allocca, and L. J. Mullen, "Characterization of signal-induced artifacts in photomultiplier tubes for underwater lidar applications," in *Airborne and In-Water Underwater Imaging* (G. D. Gilbert, ed.), vol. 3761, pp. 167–173, SPIE-Intl Soc Optical Eng, 1999.

[85] D. B. Cassidy and A. P. Mills, "A fast detector for single-shot positron annihilation lifetime spectroscopy," *Nucl. Instrum. Meth. A*, vol. 580, no. 3, pp. 1338 – 1343, 2007.

[86] T. Kelly, J. Merrigan, and R. Lambrecht, "Comparison of plastic scintillators with nanosecond lifetimes," *Nucl. Instrum. Methods*, vol. 109, no. 2, pp. 233 – 235, 1973.

[87] P. Lecoq, I. Dafinei, E. Auffray, M. Schneegans, M. Korzhik, O. Missevitch, V. Pavlenko, A. Fedorov, A. Annenkov, V. Kostylev, and V. Ligun, "Lead tungstate (PbWO4) scintillators for LHC EM calorimetry," *Nucl. Instrum. Meth. A*, vol. 365, no. 2–3, pp. 291 – 298, 1995.

[88] F. Villa, *Laser System for Positronium Excitation to Rydberg Levels for AEGIS Experiment*. PhD thesis, University of Milan, 2010.

[89] S. Aghion *et al.* (AEgIS collaboration), "Efficient laser excitation of the n=3 levels of positronium," *In preparation*, 2015.

[90] F. Villa, F. Castelli, and R. Caravita *Personal communcations*, 2015.

[91] H. Poth, B. Seligmann, W. Schwab, M. Wörtge, A. Wolf, R. Conti, W. Frieze, D. Gidley, A. Rich, M. Skalsey, J. Van House, P. Zitzewitz, J. Berger, P. Blatt, R. Neumann, and G. Putlitz, "Antihydrogen production in a merged beam arrangement," *Hyperfine Interactions*, vol. 44, no. 1-4, pp. 257–270, 1989.

[92] P. Blatt, "Laser enhanced positron capture," *Hyperfine Interactions*, vol. 44, no. 1-4, pp. 295–304, 1989.

[93] G. Gabrielse, S. Rolston, L. Haarsma, and W. Kells, "Antihydrogen production using trapped plasmas," *Physics Letters A*, vol. 129, no. 1, pp. 38 – 42, 1988.

[94] B. I. Deutch, F. M. Jacobsen, L. H. Andersen, P. Hvelplund, H. Knudsen, M. H. Holzscheiter, M. Charlton, and G. Laricchia, "Antihydrogen production by positronium-antiproton collisions in an ion trap," *Physica Scripta*, vol. T22, pp. 248–255, 1988.

[95] T. Breeden and H. Metcalf, "Stark acceleration of Rydberg atoms in inhomogeneous electric fields," *Phys. Rev. Lett.*, vol. 47, no. 24, pp. 1726–1729, 1981.

Appendices

Appendix A

Antihydrogen Production Schemes

Antihydrogen is the antimatter equivalent of hydrogen, and consists of one negatively charged antiproton as the nucleus and one positively charged positron bound to the antiproton. Even though antiparticles are created naturally from pair-production and radioactive decay, there are no presently known sources for antimatter atoms in the universe. This disparity between matter and antimatter is the subject of intensive research and there are several approaches to explaining this. The hypothesised explanations span from CPT violation (violation of the conservation of charge, parity and time) to an unknown asymmetry in the baryogenesis - the moment in the very early universe when subatomic particles and antiparticles were created and annihilated.

AEGIS therefore has to build these antimatter atoms from antiparticles and the choice naturally falls on antihydrogen, as it is the best understood antimatter atom and the only one that can actually be produced at present. The following sections will explain in more detail the two ways of creating antihydrogen that were presented in Chapter 1.

A.1 Antiprotons and Positrons

The simplest method for producing antihydrogen involves overlapping antiproton and positron clouds in order to place positrons very close to the cold antiprotons. When the anti-proton captures a positron, the binding energy is emitted as a photon with an energy of $h\nu$, as shown in Equation A.1a [91]. This method is called spontaneous radiative recombination and although it is a very simple method, it is also quite inefficient. The number of positrons and antiprotons available in these experiments is typically low, and it is challenging to keep the plasmas dense and overlapping over long time periods. The efficiency of this process can be improved somewhat by using for example CO_2- and dye-lasers in order to stimulate positrons lying in the continuum into a bound state with the

antiprotons [92].

A second reaction will always occur in addition to radiative recombinations, which is the three-body reaction shown in Equation A.1b. In this mechanism, antihydrogen is created by an antiproton forming a bound state with a positron, and a second positron receives the energy released from the recombination process [93].

$$e^+ + \bar{p} \rightarrow \bar{H} + h\nu \tag{A.1a}$$

$$e^+ + e^+ + \bar{p} \rightarrow \bar{H} + e^+ \tag{A.1b}$$

The process of three-body formation was employed by the ATHENA experiment at CERN, and was the first successful scheme ever used to create antihydrogen [3].

A.2 Antiprotons and Excited Positronium

A separate antihydrogen formation scheme involving positronium-antihydrogen collisions was proposed by Deutch *et al.*, where the reaction is shown in Equation A.2a [94]. This scheme utilises a charge-exchange reaction between a positronium atom and an antiproton. An improvement of this scheme was presented by Charlton in 1990, as shown in Equation A.2b [63]. This reaction uses Ps excited to a Rydberg state in order to form antihydrogen, where the Ps can be excited with lasers as described in Section 2.7.

$$Ps + \bar{p} \rightarrow \bar{H} + e^- \tag{A.2a}$$

$$Ps^* + \bar{p} \rightarrow \bar{H}^* + e^- \tag{A.2b}$$

The planned production of antihydrogen in the AEGIS experiment will be done by the latter scheme, combining antiprotons and excited positronium in order to form excited antihydrogen. One advantage of using Ps excited to a Rydberg state is the large cross section of the antihydrogen formation ($\sigma \sim 10^{-8}$ cm^2), which is proportional to the principle quantum number as n^4 [1]. For instance, the reaction between antiprotons and excited Ps at $n = 20$ will be $1.6{\cdot}10^5$ times more efficient than the reaction with ground state positronium.

In addition, the scope of the energy states in the produced $\bar{H}^*$ will correlate to the energy state distribution of the positronium. Due to this, the resulting distribution of $\bar{H}^*$ will be very predictable and well-defined. The charge-exchange reaction is dependent on the velocity of the antiproton and that of the positron in the Ps. The reaction has the largest cross section when these two velocities are matched.

The principal quantum number in this reaction is also important for the formation

of an antihydrogen beam, which will be an integral part of the measurements in AEGIS. Antihydrogen atoms are neutral, and it is therefore challenging to transform a cloud of these atoms into a beam. Still, excited $\bar{H}$ atoms have a large dipole moment due to charge separation, and will feel an accelerating force if influenced by a time-dependent and inhomogeneous electric field. This effect is called Stark acceleration, and becomes more efficient with a higher n [95].

Appendix B

Extra Converter Results

In addition to the converter comparison presented in Figure 4.9, the n-type (100) sample etched with 20 mA was also investigated for positronium formation, and the result is shown in Figure B.1. These SSPALS spectra were acquired in the same way as described in Section 4.3.1. This measurement was carried out some time after the initial converter comparison, and is therefore not directly comparable to these earlier spectra. The measurement was done at a time when tests of the main magnetic transport in the AD ring were being performed, and the acquired spectra are therefore more noisy.

As expected, the background spectrum has a large annihilation peak, followed by a fast decrease. The lifetime spectrum of the n-type sample etched at 20 mA displays no tail following the prompt peak. Hence, no positronium formation can be seen in this sample.

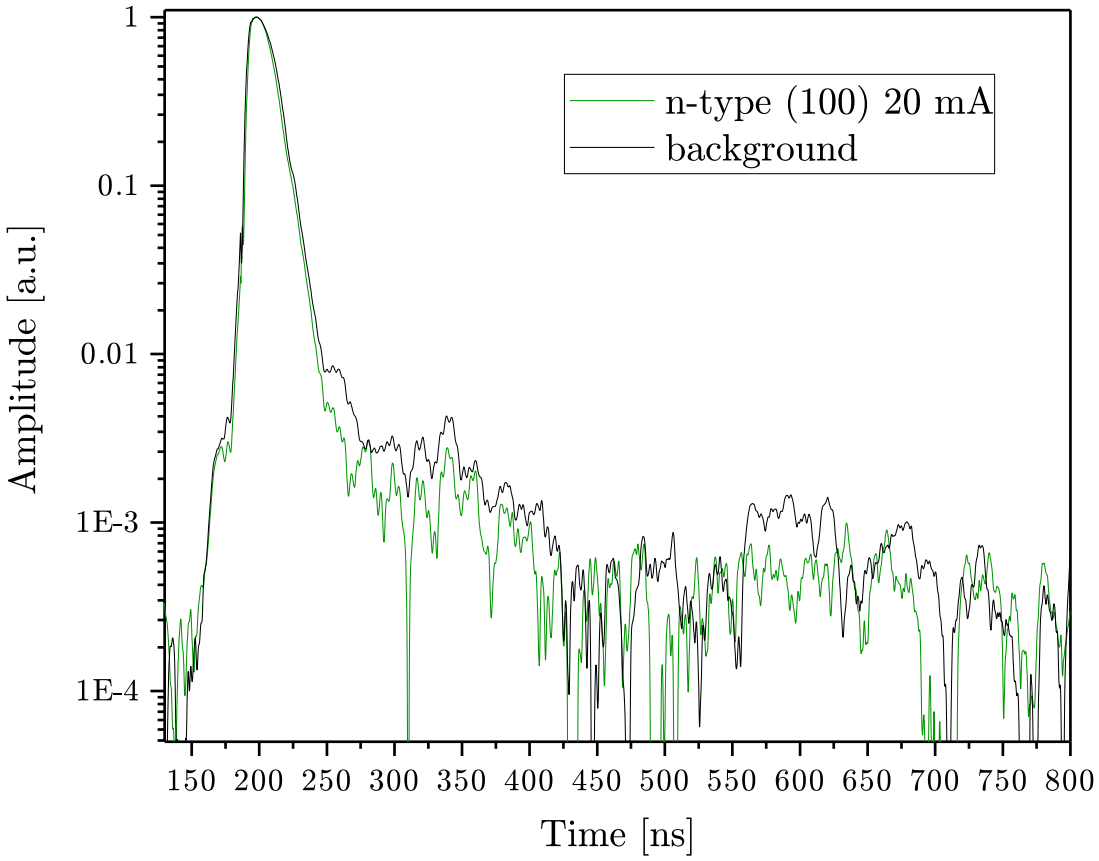

Figure B.1: Comparison of normalised SSPALS spectra for an Al plate (black curve) and an n-type (100) sample etched at 20 mA (green curve). Each spectrum here is an average of 10 shots from the accumulator. The n-type sample demonstrates no positronium production.

Appendix C

Excitation and Laser Power

Measurements were done in order to evaluate if the excitation to the $n = 3$ state was in saturation with regard to the energies of the two laser pulses. Figure C.1 shows the fraction of excited positronium as a function of the UV laser energy and the IR laser energy. Each data point represents the $S(\%)$ parameter calculated from a lifetime spectrum, where the spectra were created by averaging 10 beam shots from the accumulator. When the UV laser energy was varied, the IR laser was kept constant at 55 mJ as indicated by the arrow in C.1b, and vice versa for the variation of the IR laser energy. In the case of the IR laser energy, $S(\%)$ increases very steeply for low energies, before it reaches a plateau and saturates. The saturation is reached at an energy of 15 mJ, and the laser energy used for the experiments is 55 mJ. The IR laser energy is therefore well within saturation.

For the UV laser energy, $S(\%)$ initially increases quite fast, before it displays what appears to be a plateau or a much slower linear increase. It is not straightforward to determine if this region represents saturation or a continued increase of $S(\%)$, as both trends fit within the error bars of the data points. Earlier research by Cassidy *et al.* [60] indicates that if such a linear region occurs, it might be due to a power broadening of the laser bandwidth, which effectively enhances the spectral overlap with the Ps Doppler distribution. However, it is expected that the power broadening is much smaller for the $1 \rightarrow 3$ transition [62], and this is why the laser was initially built with a large bandwidth.

These results can also be used to evaluate if the IR laser is having any direct influence on the excitation to $n = 3$. The excited fraction goes down to 0 when the UV energy goes towards 0, as expected. When the IR energy goes towards zero, $S(\%)$ lies around 4%, which agrees with the result in Figure 4.13. In other words, the excitation to $n = 3$ is enabled by the UV radiation, while the IR radiation only makes the excitation signal clearer by ionising excited positronium atoms, thereby increasing $S(\%)$.

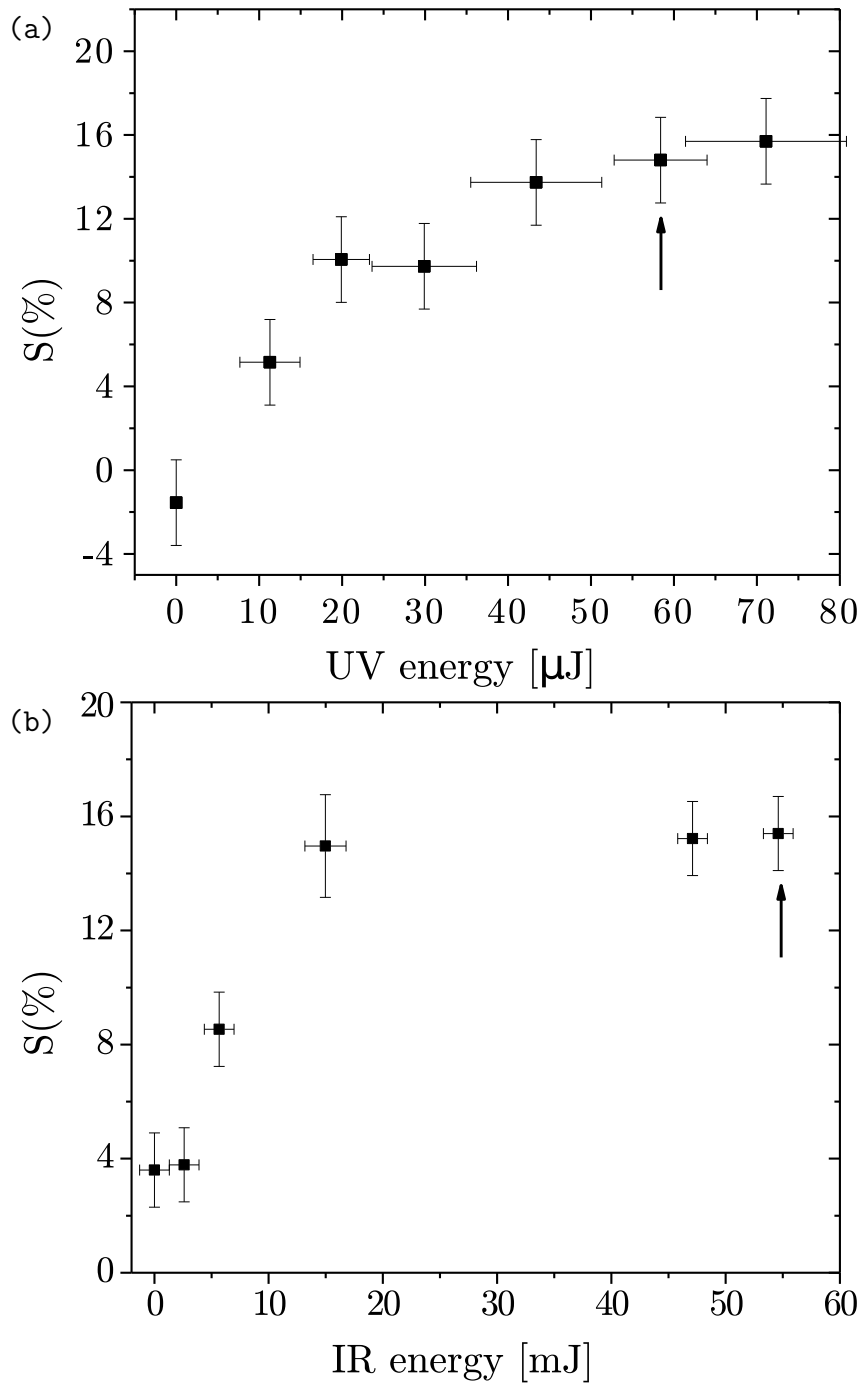

Figure C.1: The laser excitation $S(\%)$ parameter as a function of a) the UV laser energy and b) the IR laser energy. The arrows indicate the laser energies used for the excitation measurements described in Section 4.4, with 60 μJ for the UV laser and 55 mJ for the IR laser. The vertical error bars depict the standard deviation of $S(\%)$ and the horizontal error bars represent the standard deviation of the laser energies.